A Laser Speckle Based Position Sensing Technique

by

Vijay Shilpiekandula

B.Tech., Mechanical Engineering (2001)
Indian Institute of Technology, Madras

Submitted to the Department of Mechanical Engineering
in partial fulfillment of the requirements for the degree of

Master of Science in Mechanical Engineering

at the

MASSACHUSETTS INSTITUTE OF TECHNOLOGY

February 2004

Author .....
Department of Mechanical Engineering
January 28, 2004

Certified by .....
David L. Trumper
Professor of Mechanical Engineering
Thesis Supervisor

Accepted by .....
Ain A. Sonin
Chairman, Department Committee on Graduate Students

A Laser Speckle Based Position Sensing Technique

by

Vijay Shilpiekandula

Submitted to the Department of Mechanical Engineering
on January 28, 2004, in partial fulfillment of the
requirements for the degree of
Master of Science in Mechanical Engineering

Abstract

This thesis presents the design and development of a novel laser-speckle-based position sensing technique. In our prototype implementation, a He-Ne laser beam is directed at the surface of an air-bearing spindle. An imaging system is set up to capture speckle patterns scattered from the spindle surface. These patterns are highly correlated over small angular displacements of the spindle. We use correlation-based image-processing algorithms to measure offsets between the speckle patterns. These offsets are calibrated against the counts of a commerical incremental optical encoder. A custom-built bicell photointerrupter unit is used as a reference sensor for the incremental optical encoder.

To test for the control performance of this speckle-based sensor, we have constructed a transmission drive to run the air-bearing spindle. Our speckle-based metrology system is able to run at update rates of 10 Hz with a measured closed loop -3 dB bandwidth of about 2 Hz. Using a real-time processor interfaced with a desktop PC, we have implemented a novel algorithm that interpolates position estimates with respect to two pre-stored global images.

We predict that this technique can potentially achieve resolutions of 0.1 μm for translational and 5 μrad for rotational motion. The limitation of our current implementation is the low update rates resulting from the time-intensive nature of correlation-based methods. Possible methods to overcome this limitation are addressed and ideas for follow-on work are presented.

Thesis Supervisor: David L. Trumper
Title: Professor of Mechanical Engineering

Acknowledgements

First and foremost, I would like to thank Professor David Trumper for allowing me to work on this exciting project on building a position sensor. His vision for my project, passion for hands-on teaching and physical intuition into the design, dynamics and control of practical systems have always amazed me. I am proud to have achieved under his much-needed guidance the goals that we set for our sensor.

Much of my controls background here at MIT is from the course 6.302 on Feedback Systems that I credited in Fall 2001. Professors James Roberge, Steven Leeb and Kent Lundberg have been great teachers who intrigued my interest in this subject. The chapter on the control of our sensor in this thesis follows directly from material taught in this class. Professor Samir Nayfeh's 2.718 class on Design of Motion Systems provided an in-depth coverage of design concepts that enhanced my understanding of various aspects of this project.

I would like to acknowledge the following people for their help at different stages. Kripa Varanasi was a great source of inspiration from the beginning. I have learnt a lot from him over the last two years. I am grateful to him for his endless patience in discussing my work. Xiaodong Lu and Rick Montessanti have helped me out whenever I got stuck with some aspect of my project. I am thankful to them for their energy and time in clarifying my doubts.

Katherine Lilienkamp setup her DSA tool for low frequencies for my project and helped me frequently with advice on MATLAB/Simulink related aspects of our sensor implementation. Marten Byl, Murtaza Zafer and Lei Zuo discussed with me the digital controls aspect of this project and were very resourceful in identifying the problems I had with modeling the sensor dynamics. Dave Otten discussed many ideas on this project from time to time and I have greatly benefitted from these discussions.

Andrew Stein, Joseph Cattell, Yi Xie, Aaron Mazzeo and Augusto Barton made my stay at lab a fun experience. The initial setup for our speckle experiments was done as a project for 2.710 class on Optics. Andrew Stein was my partner on this team project. It was with his help that I could catch up with speed on my hardware experiments.

Ajay Deshpande, Pranava Goundan, Binayak Roy and Arvind Saraf taught me Windows programming aspects that we have examined during the course of this work. Thanks to these computer gurus for their time and energy. I would also like to thank Alon Harpaz of Dover Instrument Company for his valuable comments and suggestions regarding my work. He pointed out the Heidenhain grid encoder to me. Justin Chickles and the Technical Support of National Instruments helped me with the hardware setup, software installations and LabVIEW based programming aspects of our NI-PXI system.

Finally, I am grateful to my family and friends for being there for me always. Their unflinching support at every point of my life keeps me focused and motivated in my work. I can never forget the love and caring of Amma, Peddamma, Peddanannagaru, Vijji Mama, Vikas and Sangeeta. Vikas has been a godsend in hours when I needed him the most for his advice and guidance. Dhanush, Harsh and Lava always put

things in perspective and cheered me up. I am just so lucky to be in the company of these wonderful people.

Part of this work has been published in two NSF conferences [6, 30] and the ASPE conference 2003 [23]. This project was supported by NSF grant DMI-0084981. The author received additional support from a one-term MIT Pappalardo Fellowship.

Contents

List of Figures

List of Tables

Chapter 1

Introduction

This thesis presents a novel laser speckle based position sensing technique applicable to precision motion metrology. We have designed and developed a machine vision sensor based on the proposed technique for measuring the angular position of a rotating precision axis. This design could potentially be extended to develop a sensor for compound rotary-linear motion metrology.

1.1 Speckle Setup: An Overview

Figure 1-1 shows our prototype metrology system for measuring the rotary position of a 4 inch diameter air-bearing spindle, the surface of which is illuminated by a 0.63 mm diameter, 2 mW He-Ne laser beam of 633 nm wavelength. The matte metal surface of the spindle, whose roughness is of the order of the optical wavelength, generates in the space surrounding the illuminated spot on the spindle a high-contrast, three-dimensional random interference pattern.

A two-dimensional slice of this pattern, as shown in Figure 1-2 consists of bright and dark spots or "speckles" - bright corresponding to the constructive, and dark to the destructive, interference of wavefronts scattered from the microscopic features of the spindle surface. This pattern is obtained at a fixed point within a 1 inch distance

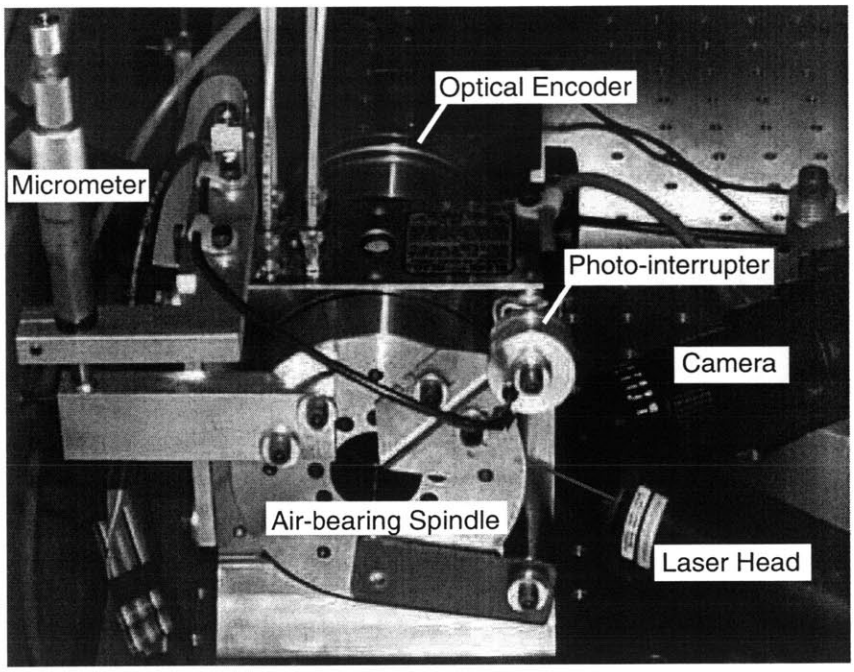

Figure 1-1: Our laser speckle based machine vision sensor for measuring the angular position of an air-bearing spindle.

from the surface by an imaging system consisting of a microscope lens assembly, a high-resolution analog monochrome CCD camera and a video capture card interfaced with a desktop PC. Details of this imaging system are provided in Section 4.2.

1.1.1 Image Correlation

For small rotations of the spindle, corresponding to a surface motion of about 10-100 μm, the speckle patterns captured on the CCD plane are highly correlated. With the rotation of the spindle, the patterns exhibit a corresponding translation of speckles and a gradual change in the spatial intensity distribution. Figure 1-3 shows two such speckle images A and B obtained before and after a small angle rotation corresponding to a 25 μm surface motion.

A mathematically rigorous approach to similarity detection between the speckle images of Figure 1-3 is two-dimensional correlation. The MATLAB plot of the auto-

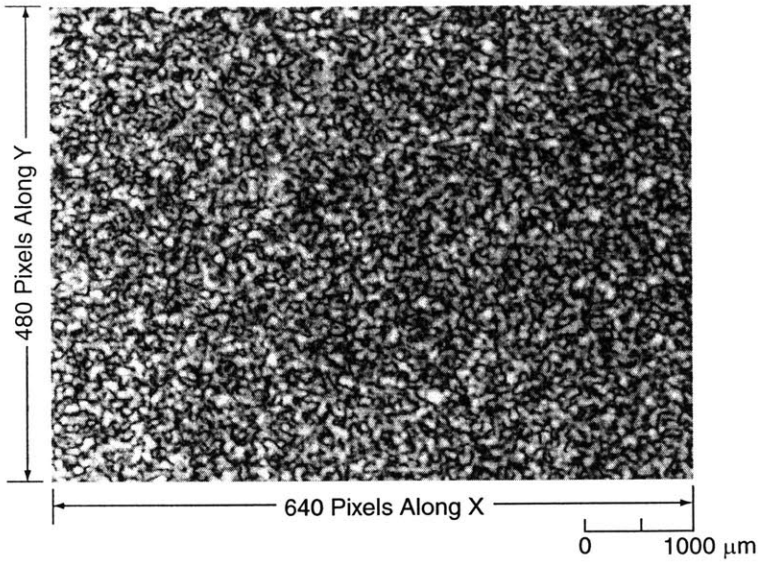

Figure 1-2: Speckle pattern captured by our imaging system. The length scale is about 10 μm per pixel along X and Y directions.

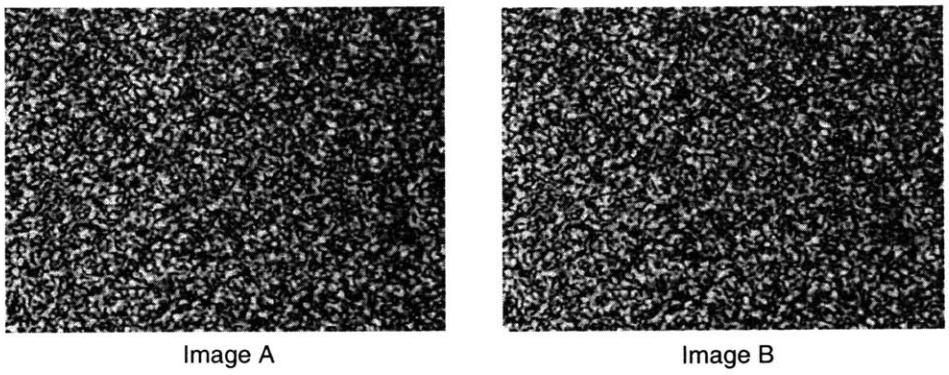

Figure 1-3: Two speckle images, Image A and Image B separated by 25 μm along the spindle circumference.

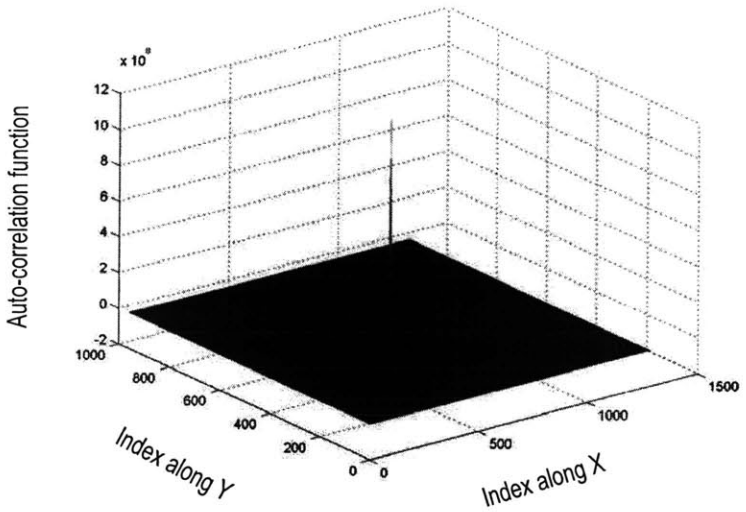

Figure 1-4: Autocorrelation function of the Image A of Figure 1-3 shows a sharp peak at (640,480) the center of the 1280 x 960 correlation plane.

correlation of the speckle image A is shown in Figure 1-4. The mean value of the intensity measured at the imaging plane has been subtracted from the data before performing the auto-correlation. This is done so as to eliminate any structure generated by the background illumination in the correlation. The auto-correlation surface is centered at (640,480) in the 1280 x 960 pixel correlation plane. An end view of the auto-correlation surface shown in Figure 1-5 depicts the sharp central peak. The signal to noise ratio is large, with no visible residual structure in the data.

The cross-correlation of Image B with respect to Image A is plotted in Figure 1-6. An end view of the same is shown in Figure 1-7. The peak of the cross-correlation surface is offset from the center (640,480) to a location (633,482) in the correlation plane. Because of the sharp peaks and the high signal to noise ratio, we can measure the offset between the correlation peaks with high resolution, to values as fine as a $1/100^{th}$ of a pixel with sufficient PC processing speed and memory, and by cross-correlating across the whole image.

We have performed a number of preliminary proof-of-concept experiments mea-

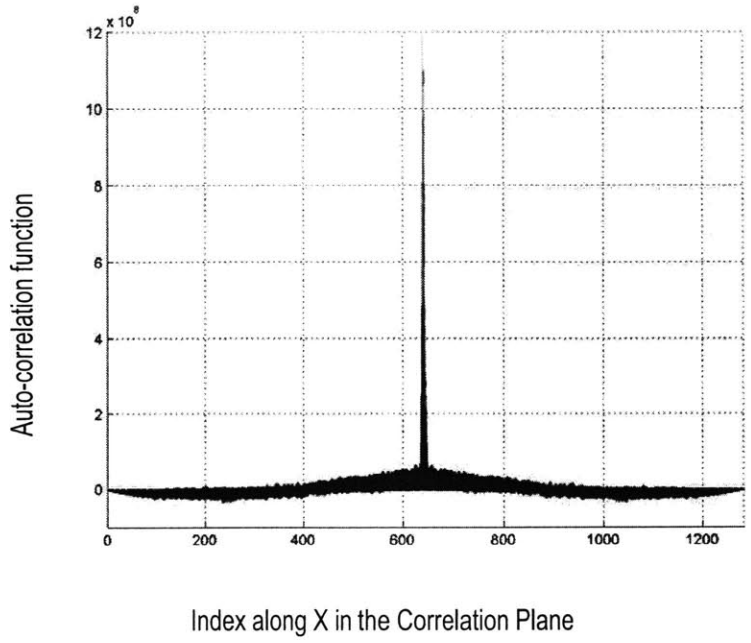

Figure 1-5: An end view of the auto-correlation surface shown in Figure 1-4.

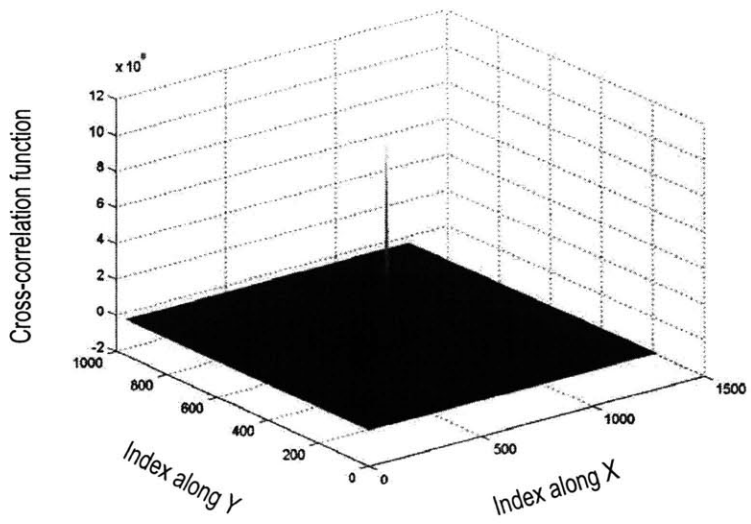

Figure 1-6: Cross-correlation of the Image B performed with respect to Image A has a sharp peak centered at (633,482).

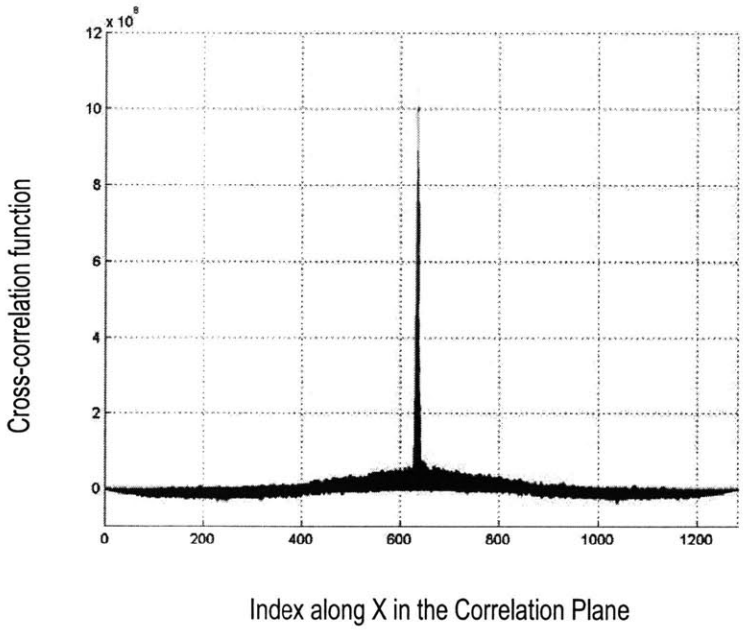

Figure 1-7: An end view of the cross-correlation surface shows the peak slightly displaced in X (by 7 pixels) from the central position X=640 of Figure 1-5.

suring offsets of the correlation peaks for discrete rotations imparted to the spindle by a micrometer setup (see Figure 1-1). Figure 1-8 shows, on a section of the pixel plane, the locus of the center of a sub-image extracted from a pre-stored reference image and matched across successive speckle images recorded on the CCD. The pattern-matching algorithm used here is based on normalized two-dimensional cross-correlation. Data points in this graph have been taken for every 5 μm of surface motion imparted with the micrometer setup. The solid line is a least square fit drawn using these points. For known rotations of the spindle as measured by the micrometer, we now can calibrate our sensor so as to determine position estimates of the spindle corresponding to correlation peak offsets. In our implementation with the micrometer setup, a peak offset of 7 pixels corresponds to a 25 μm surface motion, i.e. the resolution of our peak offset detection is 3.6 μm surface motion per pixel.

We need to check for spatial repeatability of the speckle pattern. That is, if we return to the same absolute position of the surface, will the speckle pattern be the

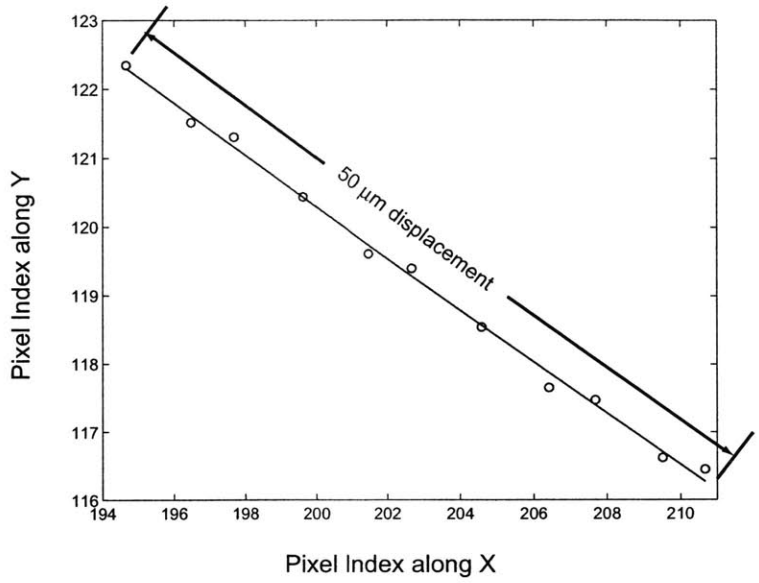

Figure 1-8: Locus of the center of a pattern matched across successive speckle images obtained for a total displacement of 50 μm along the spindle surface. The solid line is a least square fit drawn using the data points each taken for every 5 μm of surface motion imparted using the micrometer setup.

same? The data from the graph in Figure 1-9 addresses this question. Here again, we have used a pattern-matching algorithm based on normalized two-dimensional cross-correlation to detect the offset between images. To obtain each data point on the graph, we start with a chosen surface position, deviate from this position over multiple turns of the micrometer head and finally return to the same position. Though we have not measured the repeatability for every physical angular position of the spindle in the desired range of motion, this data looks promising. The scatter of the speckle pattern is within a tenth of a pixel. Since 1 pixel of motion corresponds to 3.6 μm surface motion, this indicates that we have a spatial repeatability of better than 0.36 μm.

However, the error motions from backlash of the micrometer, the cantilever deflections and temperature variations in the setup could have a significant impact on the measured scatter. At this point, we have not attempted a rigorous error analy-

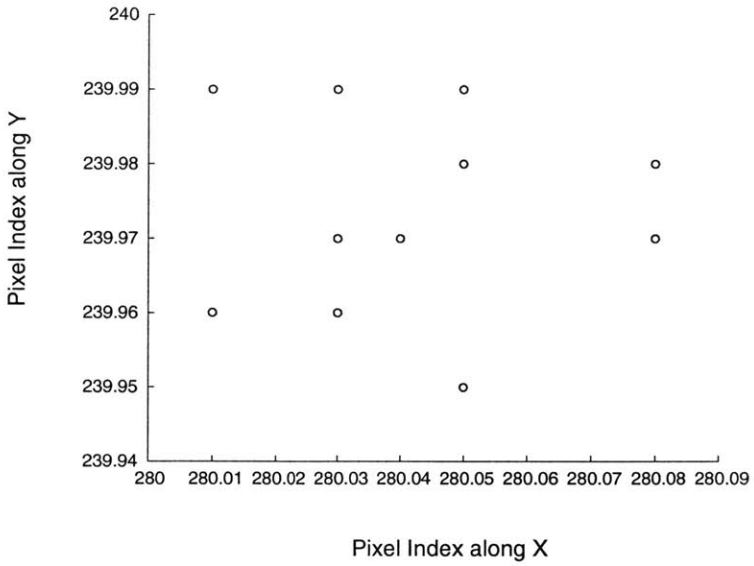

Figure 1-9: Spatial repeatability of speckle pattern as measured with the micrometer actuator. The image offsets are measured using a pattern-matching algorithm based on normalized two-dimensional cross-correlation.

sis to quantify each of the possible error terms. However, this data does provide a conservative bound on the repeatability of such speckle measurements.

1.1.2 Speckle-based Position Sensing Technique

For large rotations of the spindle corresponding to about 300 μm of surface motion, the speckle patterns de-correlate in the CCD imaging plane. Over such a large range of displacement, the spatial intensity distribution of the speckles change significantly, erasing the inherent "signature" of the pattern [14].

To address this problem, we propose storing a global library of reference images spread uniformly at a 20-100 μm pitch over the range of motion. Given the current image, the cross-correlations should be performed with respect to nearest neighboring reference images retrieved from this library. The use of a pre-stored global library for referencing each of our image correlations can allow operation over distances much larger than the decorrelation distance.

Time constraints have prevented us from implementing such a global library of speckle images. In our present implementation, as a proof of concept, we have stored just two global images spaced along the spindle surface at the above-mentioned pitch of 20-100 μm. We perform our correlation-based pattern matching routines to measure offsets with respect to these two global images and interpolate between the offsets to generate a position estimate. Our interpolation algorithm is discussed in Chapter 2.

1.1.3 Auxiliary Sensor

We have calibrated the speckle image offsets against a Renishaw[1] incremental optical rotary encoder, mounted on the spindle. We store the reference images at angular positions measured by this sensor. For the lack of a sensor with higher resolution, we have compared the results from our speckle sensor with the same Renishaw optical encoder.

The grid scale of this encoder has a grating pitch of 20 μm, and its motion can be read with a non-contact optical read head with an angular resolution of 15727 cycles/rev of the spindle. After interfacing with the digital encoder channel of dSPACE, this encoder has to a resolution of 5 μm surface motion per dSPACE line count.

The index of the encoder counts is derived from a photo-interrupter bicell unit held in mechanical fixture mounted on the spindle blockhead. This unit consists of an LED illuminating a split photo-diode through a moving slit made from two razor blades fixed to the spindle. An analog circuit interfacing with this unit generates a differential signal that hits a zero-crossing for every turn (2π rev) of the spindle. As measured using the micrometer setup, this unit has repeatability of better than 1 μm. Details of this unit are provided in Chapter 3.

[1] See Appendix B for vendor details.

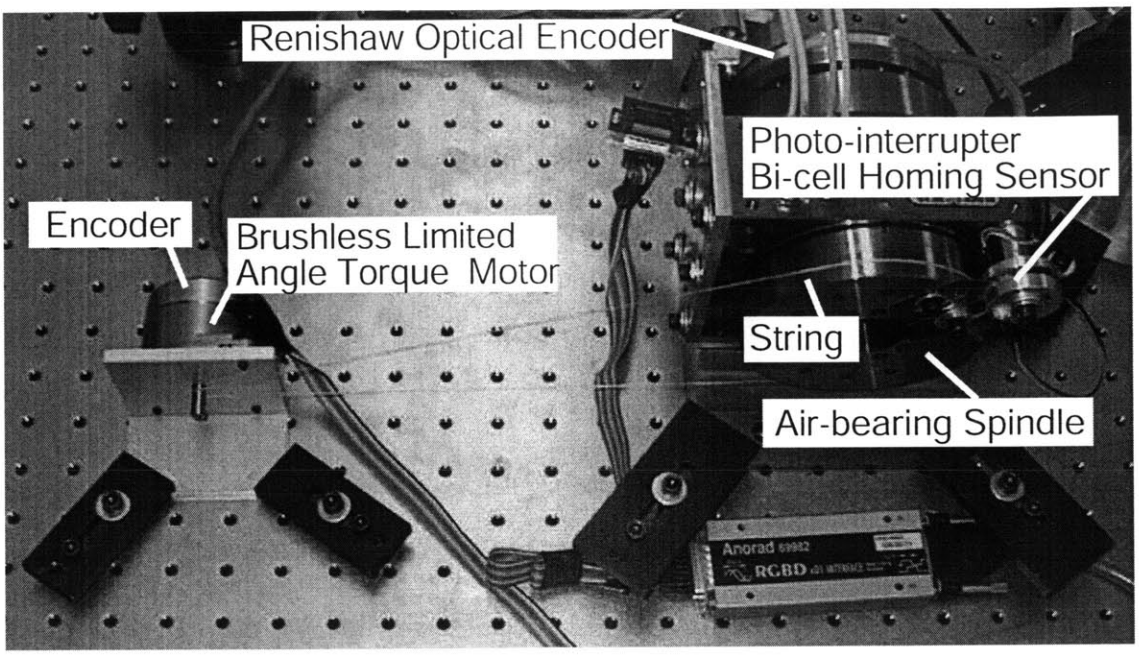

Figure 1-10: A photograph of our speckle-based metrology system. A tensioned string tied between the shaft of a brushless limited angle torque motor and the air-bearing spindle forms our low cost transmission drive.

1.1.4 Control Implementation and Results

We have successfully implemented closed loop control of position of the spindle using feedback from the speckle measurements. Here, the video capture card is interfaced with the PCI bus of a National Instruments[2] PXI Chassis run by an embedded real-time controller. Pattern-matching algorithms based on normalized two-dimensional cross-correlation are run in the real-time operating system of this controller to find the offsets between speckle images. The pattern-matching algorithms are called in a LabVIEW VI that has measured update rates of 10 Hz.

Figure 1-10 shows a photograph of our motion control system. A brushless limited angle torque motor drives the spindle through a low-cost transmission drive built using a string tied between the motor shaft and the spindle. The control system software is implemented in a dSPACE DS1103 platform, a PC based rapid prototyping controller,

[2]See Appendix B for vendor details

in conjunction with custom-built MATLAB/Simulink Models.

As shown in the schematic of control implementation in Figure 1-11, we control the voltage applied to the PA-21 power amplifier to command the voltage of the motor. Mounted on the back of the motor is an analog optical encoder with sine-cosine outputs that measures the angle of the 0.25 inch diameter motor shaft at a resolution of 1100 cycles/rev. By connecting the encoder output to the analog encoder interface available with the dSPACE DS1103, we obtain resolutions of 0.07 μm for displacement of the surface of the motor shaft.

The position of the air-bearing spindle is measured by the laser speckle based machine vision sensor. The speckle-based position is converted to an equivalent analog representation. This analog output is fed to an A/D channel of dSPACE. Further, we also interface the Renishaw incremental optical encoder system with the digital encoder interface of dSPACE. The reference signal for angular position of the encoder comes from the Photo-interrupter bi-cell unit interfacing with an A/D channel of dSPACE.

Figure 1-12 shows the output of the laser speckle based sensor when a command voltage ranging from -0.8 to 0.8 V is applied in dSPACE to the closed loop metrology system. The data points for the speckle sensor have been manually noted at intervals of 0.1 V, while averaging over around 10 iterations so as to minimize analog noise in the data. A least square fit of data points obtained using the speckle sensor matches up well with the relatively coarse Renishaw optical encoder of resolution 5 μm. The scale factor used here is 30 μm/0.8V. That is, we have mapped the digital voltage range $\pm$0.8 V to the surface displacement of 60 μm between the library images.

Our speckle-based sensor has measurement update rates of 10 Hz. The loop transmission of our control system has a cross-over frequency of 1 Hz and a phase margin of 40°. The closed loop system -3 dB bandwidth is about 2 Hz. The control performance is discussed in Chapter 5.

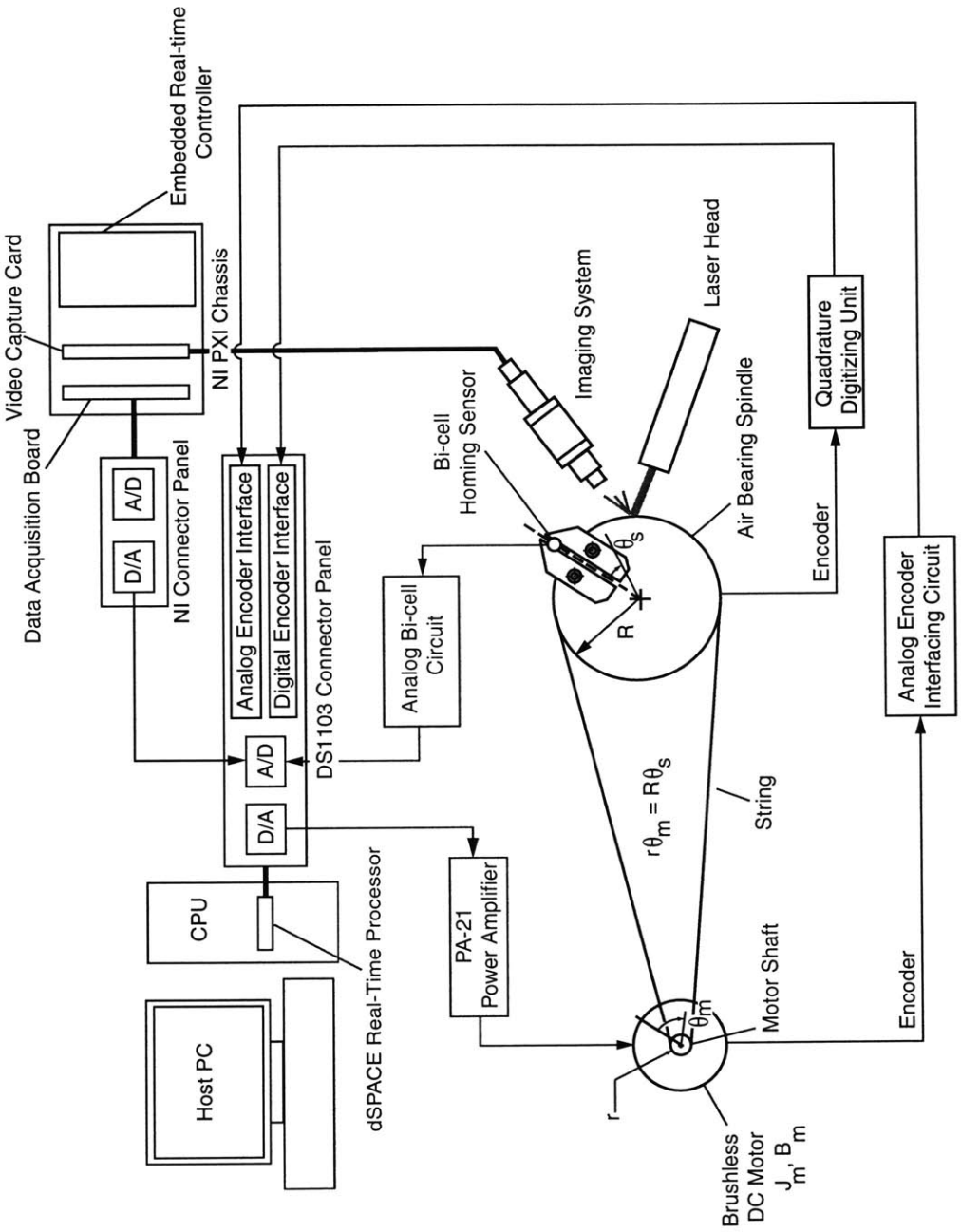

Figure 1-11: Schematic of our laser-speckle based metrology system.

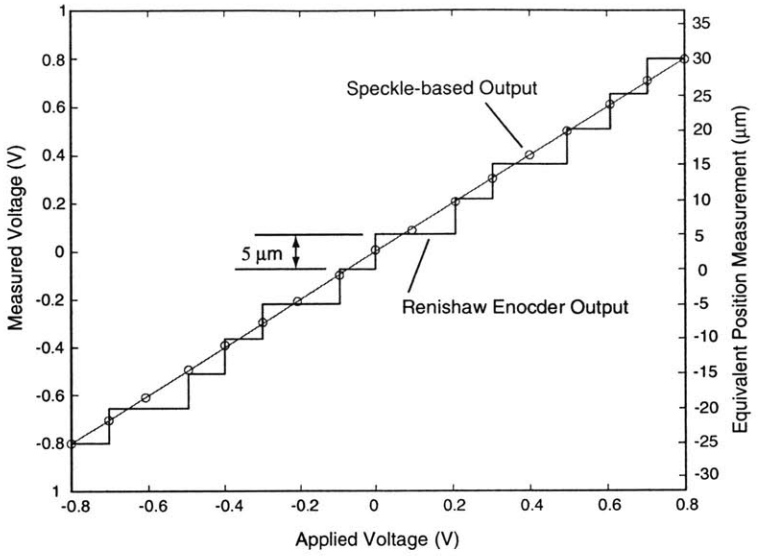

Figure 1-12: Output of the laser speckle based sensor, marked as circles, as compared with that of the Renishaw optical encoder, shown as the stair-case. Data points for the speckle-based sensor have been taken manually and a least-square fit of the data matches up well with data from Renishaw optical encoder.

With our speckle-based position sensing technique, we predict that resolutions of 0.1 μm for translational and 5 μrad for rotational motion measurement can be achieved. A significant limitation, however, of our current implementation is the time-intensive nature of image correlations across the whole pixel field. This bottleneck process accounts for the low present update rate of 10 Hz. We could improve this rate by restricting the image correlations to only those offsets where we predict the shift is most likely to be. An estimator can be constructed so that it can predict future motions from past and present information. Larger processing capabilities in terms of processing speed and memory can further reduce the computation times.

1.2 Thesis Organization

The remainder of this chapter presents the context and the motivation for the project. In Chapter 2, we examine the formation of speckle images and discuss our speckle

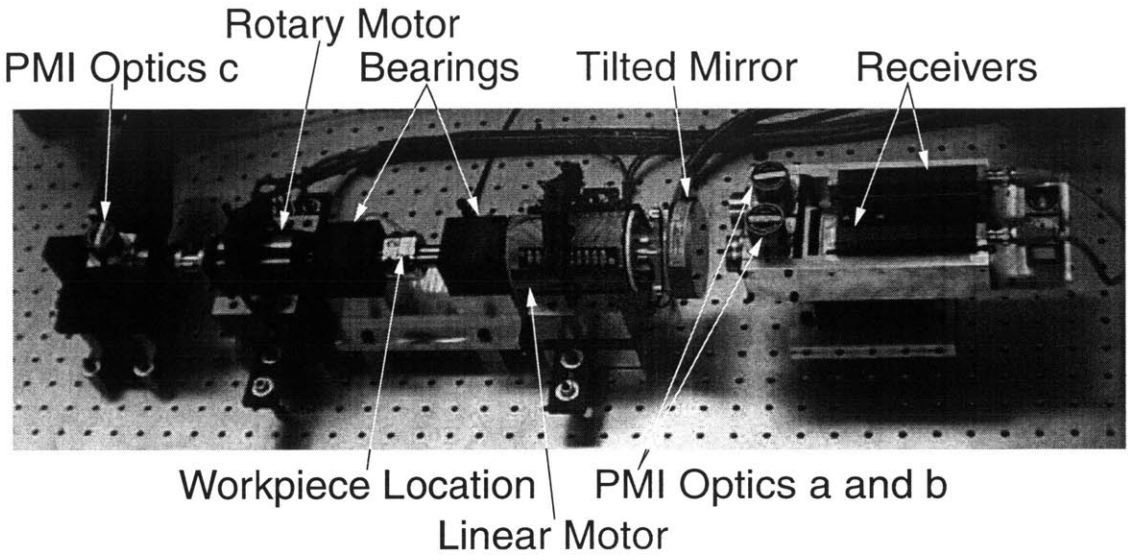

Figure 1-13: Prototype hybrid rotary-linear testbed for a novel 5-axis machining system. This picture is taken from [7].

based position sensing technique. Chapter 3 outlines the design and performance of our auxiliary sensor system consisting of an incremental optical encoder and a photo-interrupter bicell unit.

Chapter 4 presents the design of the imaging system, the air bearing spindle, and the actuators for our motion system. Chapter 5 describes the modeling and control implementation of our speckle-based metrology system. Finally, in Chapter 6, we summarize our work and suggest follow-on ideas for future work.

1.3 Background

1.3.1 Rotary-linear Hybrid Axis

This research has been motivated by the need for developing sensors that can measure the compound rotary-linear motion of a hybrid rotary-linear axis developed at the MIT Precision Motion Control Laboratory by Michael Liebman and Marsette Vona under the guidance of Professor David Trumper [1, 7, 16].

Figure 1-13 shows the prototype rotary-linear axis run on air bearings and actuated by rotary and custom-built linear permanent magnet brushless motors [7]. This hybrid axis is intended to be incorporated in 5 degree-of-freedom machine tools for machining centimeter scale parts. Separate sensors were developed to measure translation and rotation of the axis.

To implement a rotary sensor that can tolerate axial translation, a tilted mirror rotary sensor was developed. This sensor provides an absolute measurement of the angular position of the axis from the orientation of a 3 inch diameter mirror mounted on one end of the axis. The mirror has a tilt of 4.7 mrad with respect to a plane normal to the axis and has a resolution of 1,366,000 counts/rev or 4.6μrad per count. Details of the implementation of this sensor are provided in [16].

The limitation with this implementation is that the large mass of 0.29 kg of the mirror at the end of a 0.84 inch cantilever length of the axis results in a resonance at 1000 rad/s. This resonance limits the closed loop bandwidth achieved by the rotary axis controller [7].

1.3.2 Alternative Sensors

We are interested in developing non-contact sensors that do not add to the mechanical inertia or mass of the prototype hybrid axis. Liebman et al [7] studied an optical encoder technique proposed by Chitayat [18]. Figure 1-14 shows the layout of a sensor for measuring cylindrical motion of a rotary-linear actuator developed at Anorad Corporation. An optical grid is printed on the cylindrical surface of the moving part. From the motion of this grid, translation and rotation of the surface are detected. Printing a precise grid on a cylindrical surface is a significant manufacturing challenge, but it is certainly a viable approach.

In our search for non-contact sensors for two degree-of-freedom motion, we came across Heidenhain [19] KGM grid encoder and Renishaw RGX encoder. These en-

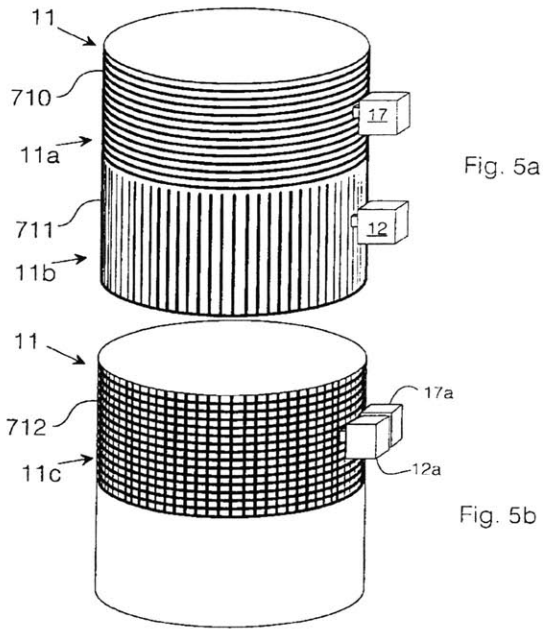

Figure 1-14: Two figures taken from US Patent 5982053, by Chitayat, of a rotary-linear sensor component of a rotary-linear actuator built at Anorad Corporation. Motion is sensed visually from the displacement of an optical pattern printed on the cylindrical surface.

coders are based on a flat grid printed on glass, and resolve planar motion as analog sine-cosine signals. We do not know of versions of these grid encoders for cylindrical motion.

Here, however, we recognize an important aspect of these sensors. The principle of optically detecting motion of a surface from the motion of a pattern on it can be applied to the sensor we intend to build. Optical mice are constructed to work on this principle. HDNS 2000 is a product of Agilent Technologies [21], used in optical mice as a compact 2 degree-of-freedom motion sensor with an in-built image acquisition system and a digital signal processor. Vona [16] evaluated this sensor for its performance through experiments on a cylinder colored unevenly using a black marker and observed significant drift (nearly 1% of a given repeated motion). The presence of drift rules out using HDNS 2000 for our purposes.

A combination of ideas from the sensors described above leads us to the speckle-based sensor. Laser speckle phenomenon is convenient in that it is a quick and easy way to from a generate a surface pattern. Since this method uses coherent light to illuminate the metal surface of the spindle, it produces images unique to the specific micro-structure of the surface [16]. If we have a machine vision system in which an image sensor captures these patterns and feeds it to image processing algorithms that detect motion of the surface from motion across the images, we have essentially a unit that provides position information that can be used for real-time control.

In the next chapter, we provide an overview of the phenomenon of laser speckle and discuss our speckle-based position sensing technique. We have implemented the laser speckle based sensor for measuring rotation alone, however, we discuss extending its functionality to compound rotary-linear motion in Chapter 6.

Chapter 2

Laser Speckle Technique

Speckle is a random noise pattern generated by spatial interference of coherent waves. In this research, our emphasis has been on the experimental aspect of this phenomenon, as observed under laser illumination of the cylindrical surface of a rotating air-bearing spindle.

Here, we provide an overview of speckle formation and present our novel speckle-based position sensing technique. Then we discuss the candidate schemes for implementing this technique. Our actual implementation is discussed in Section 2.3.

A future exercise could be to develop a numerical model for the speckle data and use it to estimate future positions based on current and past positions. In this context, we propose a state space variable description of a control system incorporating such a model in estimating angular position.

2.1 Speckle Formation

Speckle patterns are commonly observed on surfaces illuminated by laser light. For instance, surfaces exposed to low power lasers like those used in laser pointers or bar code scanners have a granular appearance because of a speckle pattern formed on them.

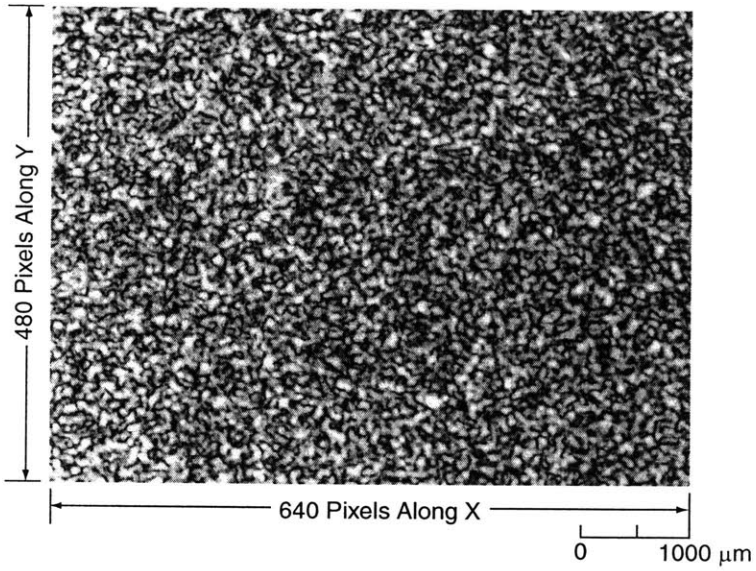

Figure 2-1: Speckle pattern captured on the CCD plane consisting of a random pattern of bright and dark spots.

A typical speckle pattern like the one shown in Figure 2-1 consists of a random distribution of bright and dark spots. On the CCD plane, the wavefronts emerging from each of the scattering centers in the laser-illuminated spot on the spindle surface superimpose to produce this random interference pattern [14]. When these wavefronts interfere, the intensity of the pattern can vary between fully dark (destructive interference) and fully bright (constructive interference) speckle spots.

References [8]-[13] provide the theoretical background necessary to understand the formation of a speckle pattern. A detailed analysis of scattering of electromagnetic waves from rough surfaces is presented in [8]. Goodman's book on Statistical Optics [9] has a section (7.5.1 in Chapter 7) devoted to statistical methods used to depict the speckle phenomenon.

Dainty [10] provides a comprehensive review of the speckle theory and early research in this field. A Fourier Optics basis and introduction to speckle interferometry methods are presented in Francon [11]. Cloud [14] discusses speckle metrology and compares it with other modern optical methods. Recent applications of speckle

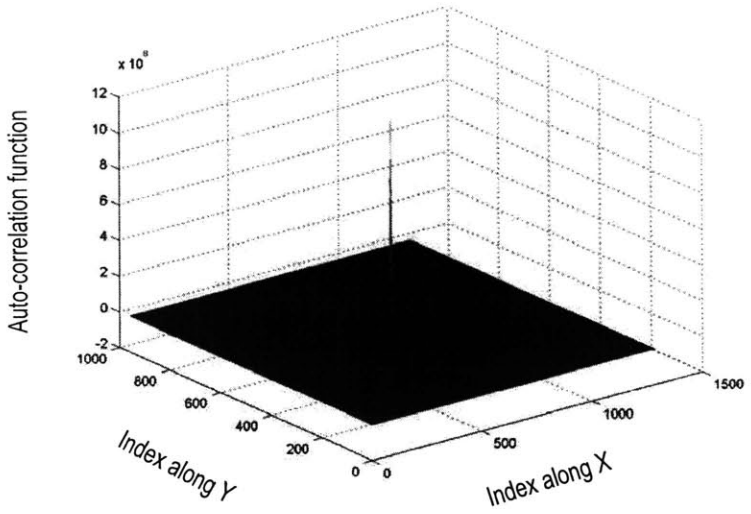

Figure 2-2: Autocorrelation function of the speckle pattern shows a sharp peak at (640,480) the center of the 1280 x 960 correlation plane.

metrology and interferometry are discussed in Sirohi [12] and Shirley [13].

Goodman [9] used first and second order statistical properties of speckles to model the auto-correlation function of a speckle pattern. In this work, we have not attempted to analyze the internal structure of the peaks of correlation surfaces obtained between successive speckle images. Understanding the internal structure of the correlation peaks could help in generating a numerical model that can be used to predict future peak positions from current and past positions. Goodman's model seems to be a good lead in this direction.

2.2 Speckle Based Position Sensing

2.2.1 Speckle Correlation

A plot of the auto-correlation of a speckle pattern captured for a fixed angular position of our PI spindle is shown in Figure 2-2. The mean value of the intensity measured at the imaging plane has been subtracted from the image data before performing

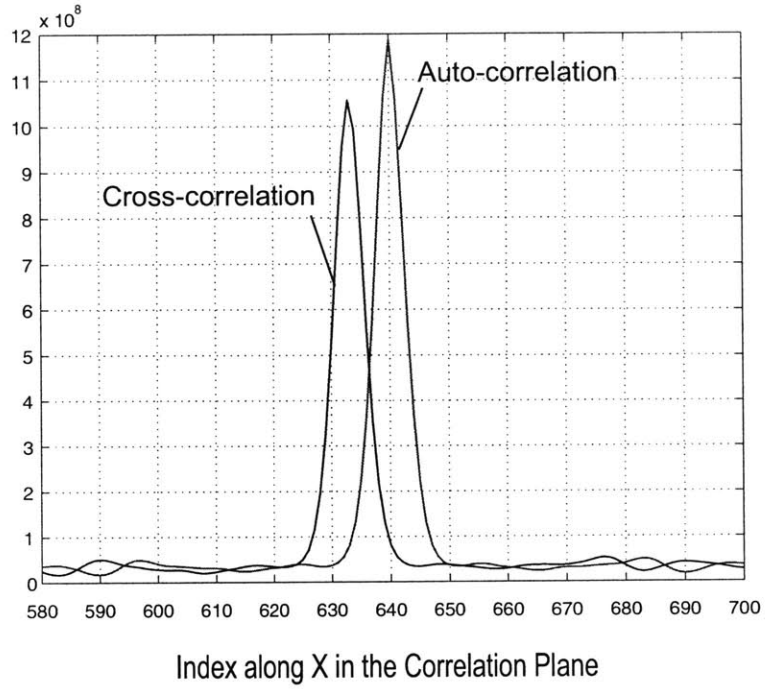

Figure 2-3: Any surface motion is reflected as an offset between the cross-correlation peak and the auto-correlation peak.

the correlation. This is done so as to eliminate structure generated by the presence of any background illumination or specular reflection components in the imaging system. The auto-correlation surface is centered at (640,480) in the 1280 $\times$ 960 pixel correlation plane, showing a sharp central peak and a signal-to-noise ratio of about $1/0.05 \approx 26$ dB.

Cross-correlation

In Figure 2-2 the auto-correlation peak is at the center (640,480) of the correlation plane. If the spindle is given a small angular displacement corresponding to a surface motion of around 10-100 μm, the correlation peak is offset from the center, thus reflecting the surface motion.

Figure 2-3 shows an end-view of the cross-correlation pattern obtained for images recorded before and after a small rotation of the spindle corresponding to a surface

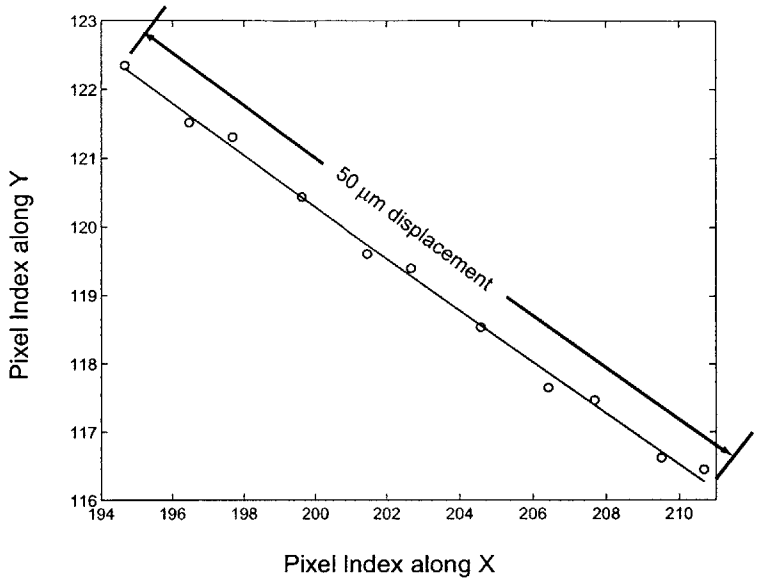

Figure 2-4: Locus of the center of a pattern matched across successive speckle images obtained for a total displacement of 50 μm along the spindle surface.

motion of 25 μm. The auto-correlation peak, centered at 640, is shown as a reference. We can measure the offset between these sharp peaks with high resolution, to values as fine as $1/100^{th}$ of a pixel with sufficient PC processing speed and memory, and by cross-correlating across the whole image.

Figure 2-4 shows, on a section of the pixel plane, the locus of the center of a sub-image extracted from a pre-stored reference image and matched across successive speckle images. The pattern-matching algorithm used here is based on normalized two-dimensional cross-correlation. The solid line is a least square fit drawn using the data points taken for every 5 μm of surface motion. The discrete displacements are provided using a micrometer actuator setup discussed in Chapter 4.

A peak offset of 7 pixels corresponds to a 25 μm surface motion, i.e. the resolution of our peak offset detection is 3.6 μm surface motion per pixel. However, we should note that we are relying here on the accuracy of the micrometer which is certainly not perfect at this level of resolution.

2.2.2 Our Technique

For our purposes, speckle is a surface signature that provides highly correlated data over small offsets (around 100 μm)[16]. This allows for high-resolution detection of position offsets between images.

The practical limitation of speckle methods is the possibility of speckle de-correlation which places a limit on the range of motion that can be recorded. To address this problem, we suggest storing a global library of reference images spread uniformly at a 20-100 μm pitch over the range of motion. Given a current image, the cross-correlations should then be performed with respect to nearest neighboring reference images retrieved from this library. The use of a pre-stored global library for referencing each of our image correlations can allow operation over distances much larger than the de-correlation distance.

Yamaguchi [17] investigated the dependence of speckle displacement with displacement of the diffuse surface generating them. By using a linear image sensor of 15 μm pitch and 1024 pixels in the detector array, Yamaguchi achieved a resolution of 35 μrad for measuring the angle of a 115-mm diameter metal cylinder. However, the encoder is based on measuring relative displacement across images. Measurements based on relative registrations are prone to drift, which cannot be tolerated for high precision measurements [16]. Though we have not verified this yet, we predict that the use of global images for referencing correlations should minimize drift in the measured position.

Figure 2-5 shows a state space model describing a proposed system in which a global library of images are recorded over the range of motion. The cross-correlator block performs correlations of the current image I with respect to the nearest two reference images I_A, I_B (corresponding to angles θ_A, θ_B of the spindle). The reference images are supplied by the retriever block from a library of global images. From the displacements ϕ_A, ϕ_B obtained between the current image and each of the reference

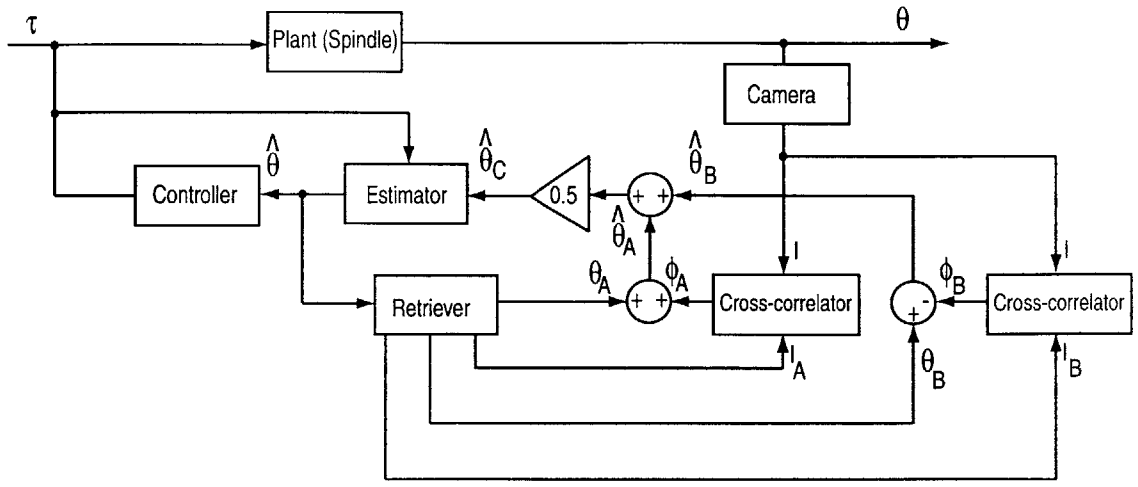

Figure 2-5: State space model for the real time application of the speckle sensor utilizes averaged estimates of angle obtained from cross-correlation of current image with nearest neighbors in a global library. An estimator further refines this value taking into account the torque inputs decided by controller in the feedback path.

images, estimates of angular motion $\hat{\theta}_A$, $\hat{\theta}_B$ are obtained. An average of these estimates $\hat{\theta}_C$ is fed to an estimator which refines this value to $\hat{\theta}$. The torque τ driving the spindle is supplied as one of the inputs to the estimator. A controller placed in the feedback path can be designed to obtain the desired specifications for the closed loop system.

Due to time constraints, we could not implement such a global library of speckle images. In our implementation, as a proof of concept, we have stored just two global images separated by about 20-100 μm along the spindle surface. For a given current image, we obtain a refined estimate of spindle angle by interpolating between the results of cross-correlations performed with respect to these two images.

Figure 2-6 shows the schematic for our interpolation. The circles with 'X' represent the cross-correlation operator. Current image I is correlated against nearest global neighbors I_A and I_B corresponding to angles θ_A and θ_B. The displacement across images ϕ_A and ϕ_B denote the separation with respect to the global images along the line of motion. Figure 2-7 shows on the pixel plane the process described above, for

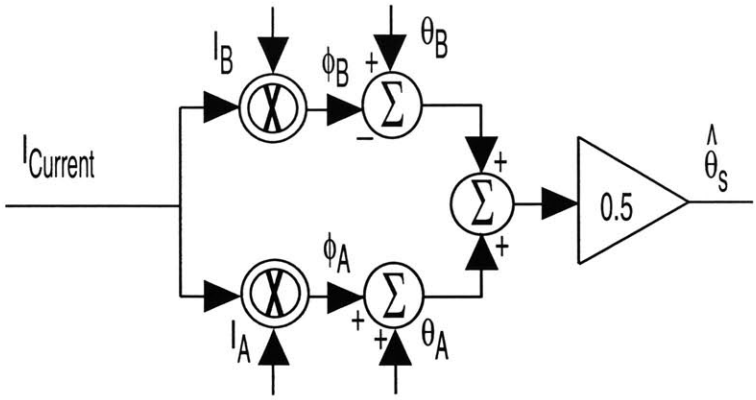

Figure 2-6: Interpolation schematic for obtaining a refined estimate of current position from image offsets measured with respect to two neighboring global images. Circle with 'X' represents the cross-correlation operator.

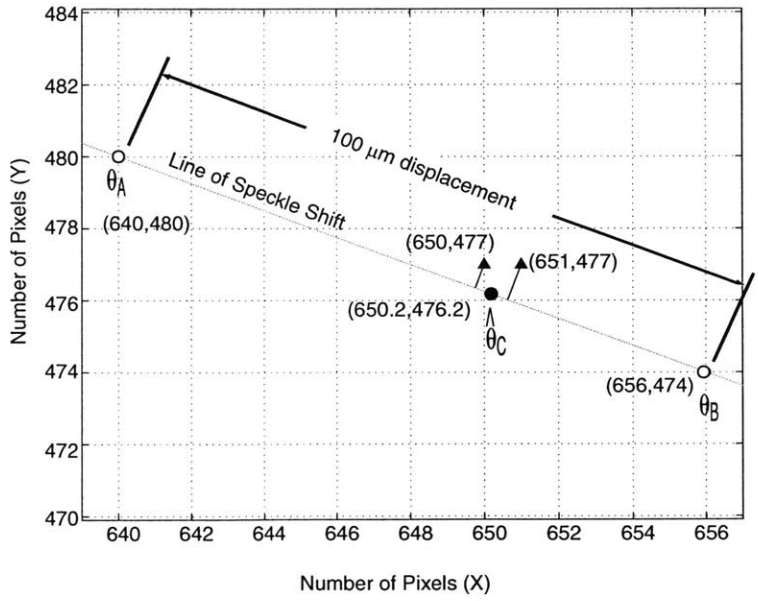

Figure 2-7: Interpolation between library images refines estimate of angle. Coordinates of peak corresponding to the averaged estimate is (650.2,476.2). This indicates linear motion of 63.2 μm measured from A.

the case when the library images are spaced at intervals of 100 μm. The projections of the corresponding peak locations onto the line of motion are averaged to obtain an estimate of the current angle $\hat{\theta}_C$ [6].

2.3 Speckle Correlation Implementation

2.3.1 Candidate Schemes

We have kept the imaging system in our setup simple, with just a microscopic objective lens and an analog camera interfaced with the PC by a video capture card. Using our speckle-based technique, we would like to estimate surface position from the offsets measured across the speckle images. The challenge here is to have the image correlations run real-time so that speckle-based sensing can be tested for its control performance. Our real-time setup discussed in Section 2.3.2 consists of a National Instruments(NI) PXI system[1] with a video capture card and LabVIEW based image processing algorithms run by an embedded real-time controller.

In our preliminary setup, we have used a PC-based video capture card, purchased from Coreco Imaging Company[2]. This video capture card came with a Windows-based software that allowed us to manually save the image files to the hard disk in any of the standard formats - bmp, jpeg or png. We used MATLAB-based mfiles to perform the two-dimensional cross-correlation of the image files. The computation time in MATLAB associated with performing cross-correlation of two 640×480 images is about an hour on our 1 GHz PC. This is too slow to be applicable to real-time position sensing.

Yamaguchi [15, 17] reduced the computational time considerably by performing line correlations of speckle images. If we were to implement line correlation, we

[1]See Appendix B for vendor details.
[2]See Appendix B for vendor details.

would have to choose a line scan camera, which is much costlier than an area scan CCD array. Moreover, we would like to use as much of the available speckle data as possible, since that would ensure that we are less affected by inaccuracies in the image sampling at the CCD array. Vona [16] compared cross-correlation as against FFT based methods and absolute difference methods. Even with these other methods, the times for computation are not sufficiently low.

An important issue here is interfacing the video capture card directly to the PC-based MATLAB code. We understand that the MATLAB based cross-correlation algorithm may not be optimal for real-time computations. Even if we have an efficient image-processing software (or C based code) that can compute for us the correlations at much faster rates, how would the processed data be transferred to the motion control implementation that we have built in dSPACE?

The discussion here follows directly from ideas presented by Marty Vona who helped us initially in identifying candidate schemes for the real-time implementation. First of all, any software code based on a Windows Operating System is not likely to work for our real-time implementation. Windows is not a real-time operating system since the processor time in Windows is shared between programs running on the system. We should hence have a separate real-time processor to run our image processing code.

Coreco Imaging, the vendor of the Bandit video capture card, provides, at an additional cost, a software developer's toolkit that contains custom routines allowing access to features of the video capture card. Using Win32 programming in C, the video data from the capture card can be directly transferred to the PC system memory by DMA (Direct Memory Access). We can then transfer this data from the PC system memory to the dSPACE controller board and then perform the image processing in dSPACE.

dSPACE has a custom library of sub-routines called CLIB that can be used in

a C code to access features of the dSPACE board. Since dSPACE DS1103 that we have in our lab does not come with solutions for video-processing, we would have to develop our own realtime image processing code in C (or use the code we already have in MATLAB) and get dSPACE to call these routines using CLIB (or MLIB, the CLIB equivalent for MATLAB).

However, this implementation is again challenging since all the C or MATLAB code that we use would have to run real-time so that no delays occur in the execution of the code. The developmental effort associated with implementing the Coreco video capture card and dSPACE appeared to be much larger compared with configuring and developing all the embedded code for a higher-end image processing system provided with its own DSP.

The NI PXI-based system is reasonably priced (after an academic discount) and provides a system-level integration of the image acquisition hardware and image processing software. This is a more efficient approach, since the low-level programming aspects are already taken care of. All that we have to do is configure the system and call the appropriate routines in a LabVIEW-based code.

2.3.2 Our Implementation

NI PXI-based system

Our implementation shown in Figure 2-8 for computing speckle correlations integrates image acquisition hardware with image-processing software in a NI PXI-based system. The hardware apparatus consists of a video capture card and a data-acquisition board installed in a bench-top NI PXI chassis provided with an embedded real-time controller.

The video capture card is provided with an analog-to-digital (A/D) converter that digitizes the speckle images at 8 bits per pixel, corresponding to a gray scale of 256 levels. The digitized image data is transferred at frame rates of 30 Hz via the PCI

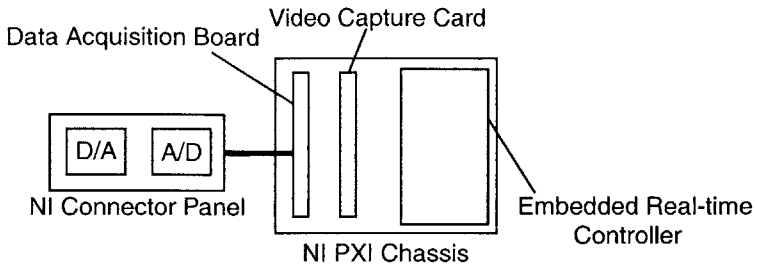

Figure 2-8: Our setup for speckle image acquisition and image processing consists of a NI PXI chassis with a video capture card interfaced in the real-time operating system of an embedded real-time controller.

bus to the system memory by an onboard DMA (Direct Memory Access) controller.

The data acquisition board has an input/output (I/O) connector panel with access to 8 A/D and 2 D/A channels. The position estimated from the image-processing algorithms is converted to an equivalent analog output, generated by a 16-bit D/A converter.

Pattern-matching sub-routines based on normalized two-dimensional cross-correlation are used in the real-time operating system of the controller to find the offsets between speckle images streamed at the video rate (30 Hz) by the video capture card. The pattern-matching algorithms are called in a LabVIEW VI, the user panel of which is shown in Figure 2-9.

Prior to running the LabVIEW code, two reference images are recorded and stored using the NI image acquisition software that communicates with the video capture card. The NI-PXI chassis is booted in real-time and the image files are transferred from the host PC through an ftp process to the real-time operating system. The image-processing algorithms called in the VI correlate the current image against the two reference images and interpolate between the results to obtain a position estimate. This estimate is converted into an equivalent analog output and interfaced with the A/D channel of the dSPACE DS1103 connector panel. The software implementation of our system is detailed in Appendix A.

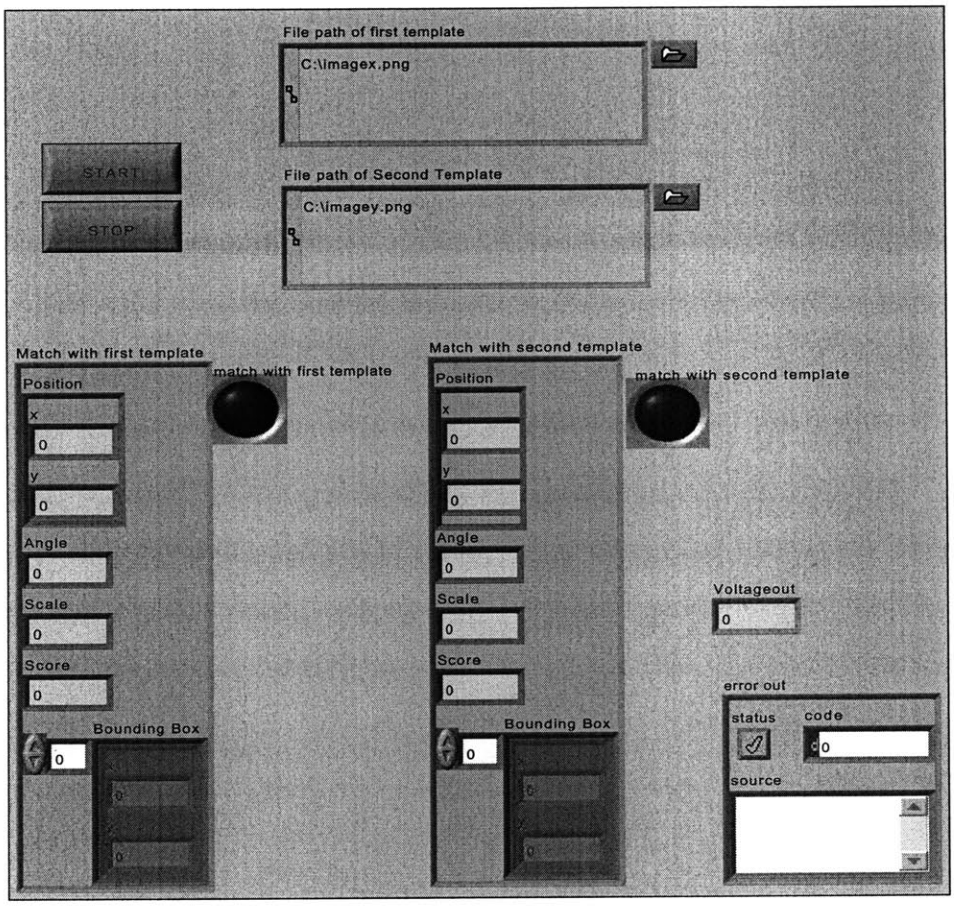

Figure 2-9: LabVIEW user panel of our implementation of the speckle-based sensor. Current image is correlated against two pre-stored reference images. Indicators are lighted when a pattern match is found. The position estimate is converted to an equivalent voltage output also displayed in the panel.

Chapter 3

Auxiliary Sensor System

We have calibrated our laser speckle-based position measurements with respect to a rotary incremental optical encoder mounted on the air-bearing spindle. We need a reference sensor to index the counts of this encoder. To this end, we have built our own photo-interrupter bicell unit, which is operated in a differential voltage mode. The differential output signal of this unit crosses a zero value for every 2π rotation of the spindle. The encoder counts are triggered once this zero-crossing is detected.

This chapter describes the design and development of this auxiliary sensor system made from the encoder and the photo-interrupter bicell unit. First, we discuss the encoder system. We then examine the concept of quadrature and see how it is used in our encoder system to increase resolution by a factor of 4 and also to detect direction of motion. In Section 3.2, we describe the operation and performance of the photo-interrupter unit.

3.1 Renishaw Incremental Optical Encoder

Figure 3-1 shows a Renishaw[1] incremental optical encoder mounted on our air-bearing spindle. This encoder is available as a stainless steel ring with an integral 360° grid

[1]See Appendix B for vendor details.

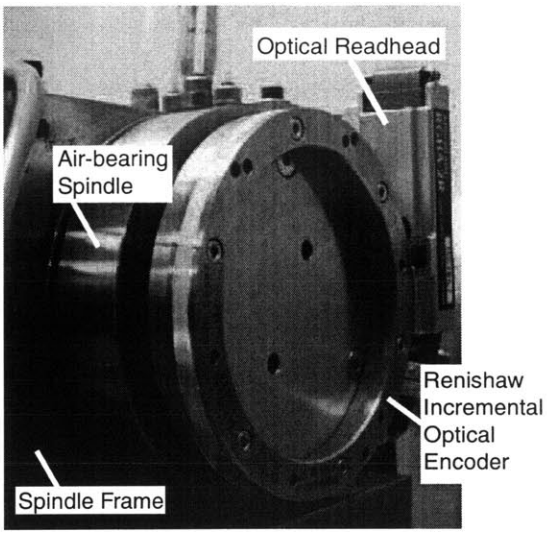

Figure 3-1: Incremental optical encoder along with the readhead and quadrature digitizing unit provides quadrature output signals that are read into the digital encoder channel of dSPACE.

scale along its circumference. The grating pitch of the scale is $20\,\mu$m. The analog sine and cosine outputs from a non-contact read head fixed to the spindle are connected to an Anorad[2] quadrature digitizing unit.

3.1.1 Quadrature Output

The digitized outputs of an incremental optical encoder are 90° out of phase, or in "quadrature", with each other. Each full cycle consists of four state transitions, or edges. Our Renishaw RGR encoder, for example, has a resolution of 15727 cycles/rev, which corresponds to 62908 edges per revolution.

Figure 3-2 shows the schematic for the digitized outputs A and B of the encoder system as a function of surface displacement x. The period of the square waveforms is 20 μm and they are 90° out of phase with each other. The amplitude of each waveform can assume values of 0 or 1. There are four possible combinations, or "states" as given in Table 3.1.

[2]See Appendix B for vendor details.

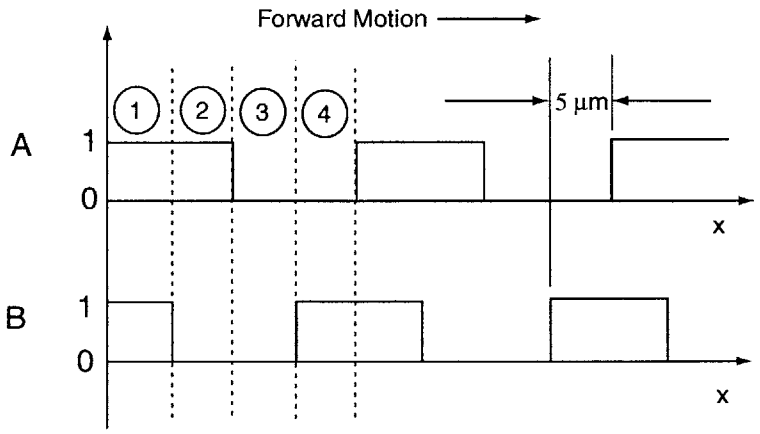

Figure 3-2: Schematic showing digitized quadrature output of the Renishaw incremental encoder system.

State	Output A	Output B
1	1	1
2	1	0
3	0	0
4	0	1

Table 3.1: Quadrature states of digitized outputs of the Renishaw encoder system.

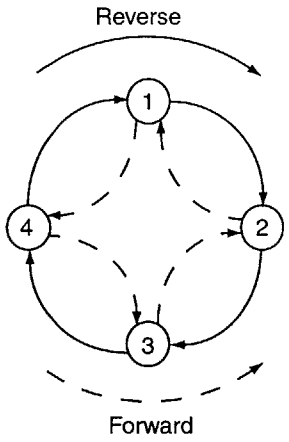

Figure 3-3: Valid state transitions are as indicated. Direction can be detected from the sequence of transitions.

If the spindle moves, the encoder state changes. For a transition from any given state, only two final states are allowed of the possible three. These valid transitions are given in Figure 3-3. The direction of motion is indicated by the sequence of transitions. For the outputs A and B shown in the figure, motion in the forward direction corresponds the sequence 1→4→3→2→1, while motion in the reverse direction corresponds to 1→2→3→4→1.

3.1.2 Resolution

The Renishaw incremental encoder has a 20 μm grating that corresponds to a resolution of 15,727 cycles/rev of the ring, whose nominal diameter is 100 mm. When interfaced with a quadrature digitizing unit, the 20 μm sine-cosine output is converted to square waveforms of 20 μm period and 5 μm quadrature shift.

The digital encoder channels of dSPACE DS1103 board have 24-bit counters and a 4-fold line-subdivision. When interfaced with this channel, the Renishaw encoder has a 1/4th line count for every 5 μm of surface motion. We have scaled this up in our Simulink model so that the resolution is a surface motion of 5 μm per encoder line count.

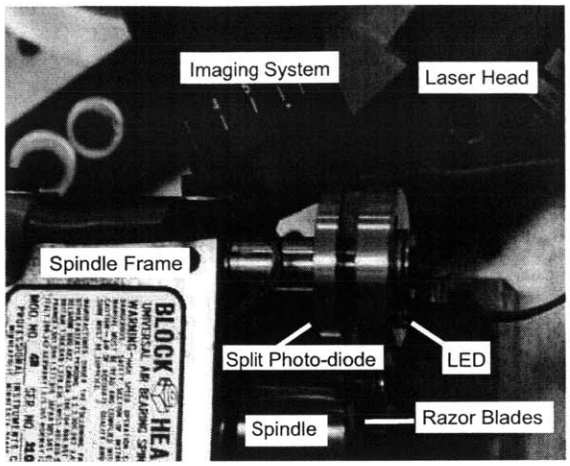

Figure 3-4: Photo-interrupter bicell unit consists of a LED illuminating a split photo-diode through a moving slit. The slit is made from two sharp razor blades separated by 0.02 inch and fixed to the spindle.

3.1.3 Need for a Homing Sensor

Incremental encoders need a reference or "homing" signal that triggers the encoder counts. The unit that we purchased from Renishaw was not provided with a homing sensor.

In the next section, we look at the design and implementation of the photo-interrupter unit that provides the reference signal for our Renishaw encoder. Because of its simplicity in principle and construction, we have found this unit to be an effective low-cost alternative to commercial homing sensors. This unit has a repeatability of better than 1 μm, as measured using the micrometer setup.

3.2 Photo-interrupter Bi-cell Unit

Figure 3-4 shows our photo-interrupter bicell unit in which an LED illuminates a split photo-diode through a moving slit. The slit is made from two sharp razor blades separated by 0.02 inch and fixed to the spindle. An analog circuit interfacing with this unit generates a differential voltage signal that hits a zero-crossing once the slit passes

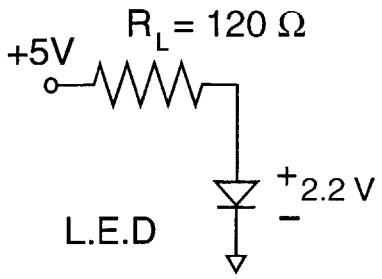

Figure 3-5: Analog circuit used to light the super bright LED.

between the LED and the split photodiode. The analog differential signal is fed to an analog-to-digital (A/D) channel of dSPACE. The zero-crossing of the corresponding digital signal is used to trigger the counts of the Renishaw encoder.

3.2.1 Light Source

In the visible spectrum, the spectral responsivity of the bi-cell sensor is highest for red at a value of 0.4 A/W. We have hence used as our light source a super bright LED[3] emitting red light (wavelength λ=630 nm). The circuit used to light the LED with a 5 V applied using a DC power supply and 120 Ω, 0.5 W resistor R_L is shown in figure 3-5. The absolute maximum peak forward current of the LED is specified at 50 mA. For a typical voltage drop of 2.2 V across the diode, the current i is set by the resistor R_L. The value of i can be calculated from Kirchoff's Voltage law as (5 V - 2.2 V)/ 120 $\Omega \approx$ 23.33 mA, which is below the maximum peak value of 50 mA.

3.2.2 Split photodiode

In position sensing applications, photodiodes are used as light detectors. These detectors usually contain multiple active areas, or cells, separated by narrow gaps. In our implementation, we have used such a "split" photodiode, known commercially as a bicell, to detect the motion of slit moving across it. Our bicell has two active areas,

[3]See Appendix B for vendor details.

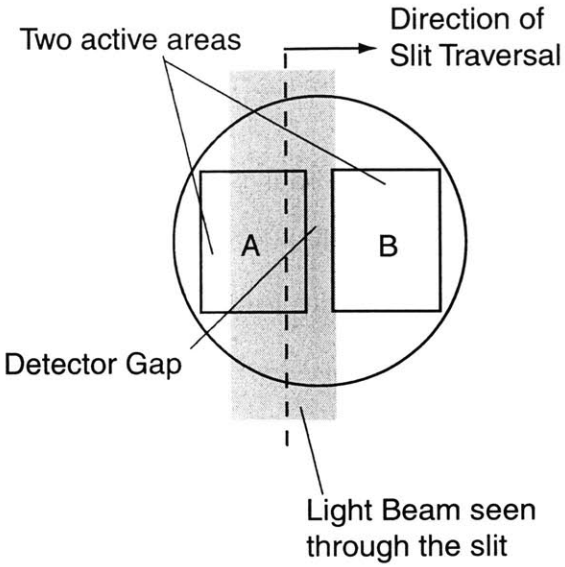

Figure 3-6: Schematic of operation of the bicell photodetector. The slit is shown lightly shaded. It is formed between two razor blades, which block the light beam falling on the active areas A and B. The LED source is out of the page and in front of the detector.

each of size 0.023 inch $\times$ 0.047 inch, and separated by a narrow gap of 0.0008 inch. We purchased this detector from Advanced Photonix, Inc[4]. The slit moving across the bicell is formed between the sharp edges of two razor blades fixed to the spindle.

Operation

A schematic of the operation of the bicell unit is shown in Figure 3-6. As the spindle rotates, the razor blades containing the slit move between the LED source and the bicell detector. The slit is shown in the figure as a lightly shaded rectangular strip incident on a part of the active area A. The remaining part of this active area A and the entire active area B cannot see the light from the LED since they are blocked by the opaque razor blades. The currents here are dark currents, while the current in the lighted portion of the active area A is the photocurrent. As the slit moves across the bicell, the difference between the currents is obtained from an analog circuit, shown

[4]See Appendix B for vendor details.

in Figure 3-7. When the slit is centered exactly at the center of the photo-detector gap, the differential signal generated by this circuit hits a zero-crossing.

The currents from each cell of the split photodiode are first passed through two separate transimpedance amplifiers. These amplifiers are constructed using an LM741 op-amp in an inverting configuration with Resistor R = 62 kΩ and Capacitor C = 1 nF connected in parallel in the feedback path. Photocurrent I(s) generated in each cell is transduced by the impedance network to a voltage V(s) given by

$$\frac{V(s)}{I(s)} = \frac{-R}{RCs+1} \tag{3.1}$$

Thus, the impedance network acts as a low pass filter with a -3 dB bandwidth of $1/(2\pi \times 62 \times 10^3 \times 10^{-9}) \approx$ 2.5 kHz.

The voltages thus obtained from each cell are then supplied to a differencing circuit built using a three-op-amp instrumentation amplifier [22]. The input stage of the amplifier is configured from two op-amps X and Y that provide high differential gain ($G_{sig} = 1+2R_2/R_1$) and unity common-mode gain ($G_{CM} = 1$) without the need for any close resistor matching. The differential output of this stage has a substantial reduction in the common-mode signal. The differential amplifier Z has unity gain ($G_{sig} = 1$) and filters further for any common mode component present in the signal ($G_{CM} \approx 0$).

We have used as the instrumentation amplifier in our circuit a AD621 amplifier with a preset gain of 10. The hardware circuit-board implementation is shown in Figure 3-8. The output differential signal V(s), for input currents $I_1(s)$ and $I_2(s)$ of the cells of the split photodiode, is given by

$$V(s) = \frac{-10R}{RCs+1}[I_1(s) - I_2(s)] \tag{3.2}$$

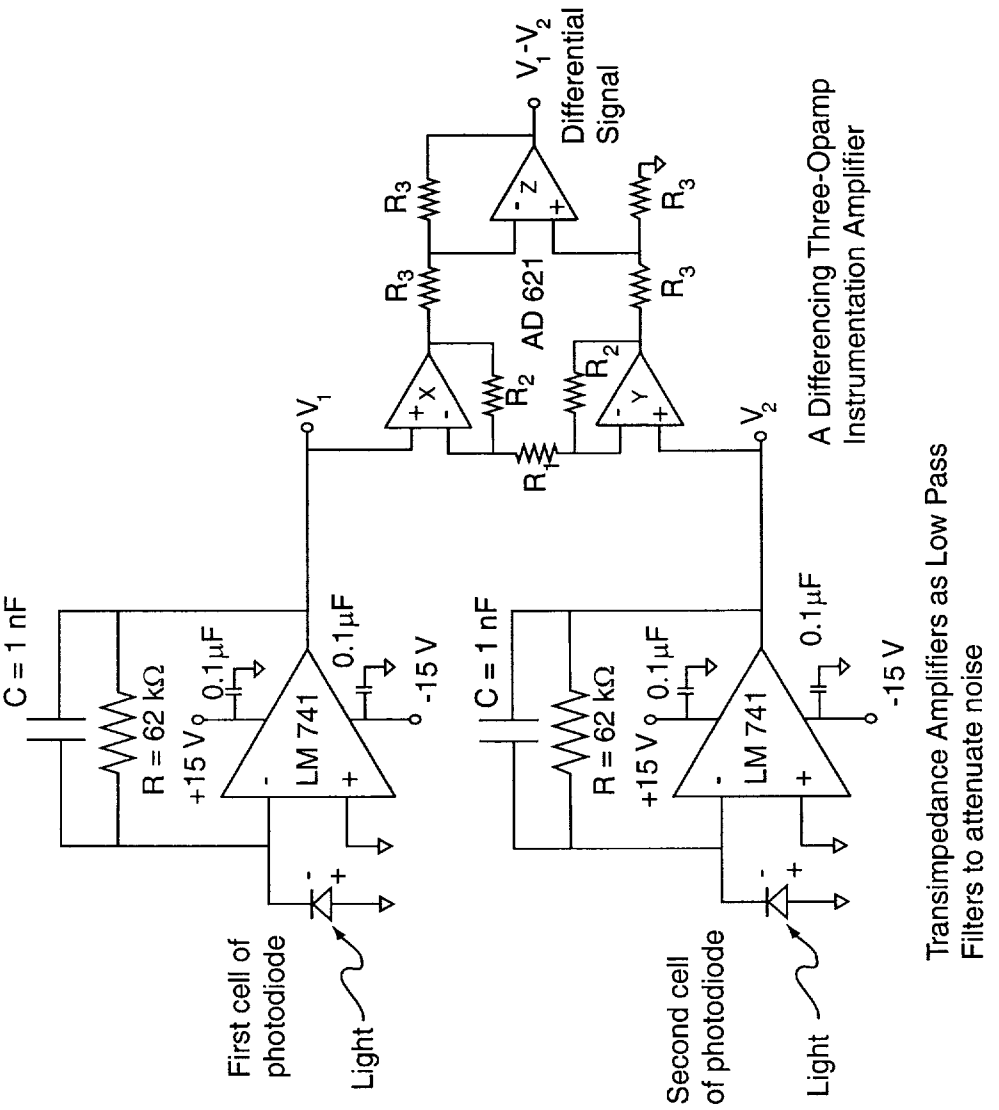

Figure 3-7: Outputs of the separate cells of the split photodiode are filtered for noise with a transimpedance amplifier and their difference is found using a AD621 three-opamp instrumentation amplifier.

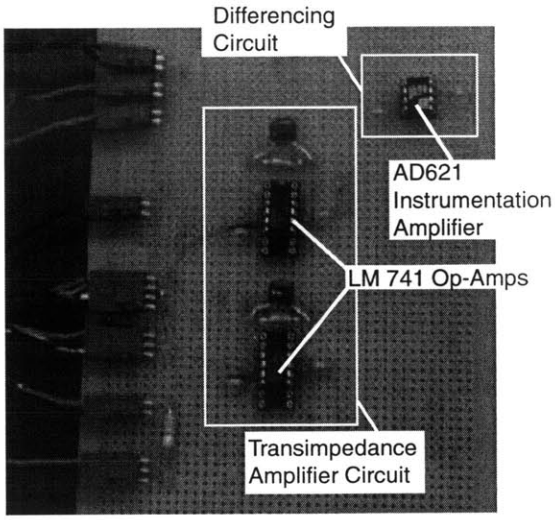

Figure 3-8: Circuit board implementation of the low pass filtering transimpedance amplifier and differencing instrumentation amplifier.

3.2.3 Performance

In usual photodetector setups, optical filters are used to desensitize the system to variations in the intensity of the ambient light. Since we have used our photo-interrupter unit in a differential voltage mode, we do not need any such filter [27]. It might still help to have such optical filters. Additionally, the differential voltage mode ensures that the unit is unaffected to first order by variations in the intensity of the LED.

We measure the voltage output of the AD621 amplifier at different positions of the slit, set by turning the spindle using the micrometer setup. Since our micrometer has backlash, we have recorded voltages only for the clockwise rotation of the micrometer thimble.

Figure 3-9 shows 5 sets of data collected with our setup. For each data set, the voltage output of the AD621 is measured at every $10\,\mu$m of micrometer displacement. The total micrometer displacement corresponding to this data is 110 μm, which, in turn, corresponds to a 55 μm displacement along the spindle surface. A least-square fit line is drawn for the data of each trial. By linear interpolation, the zero-

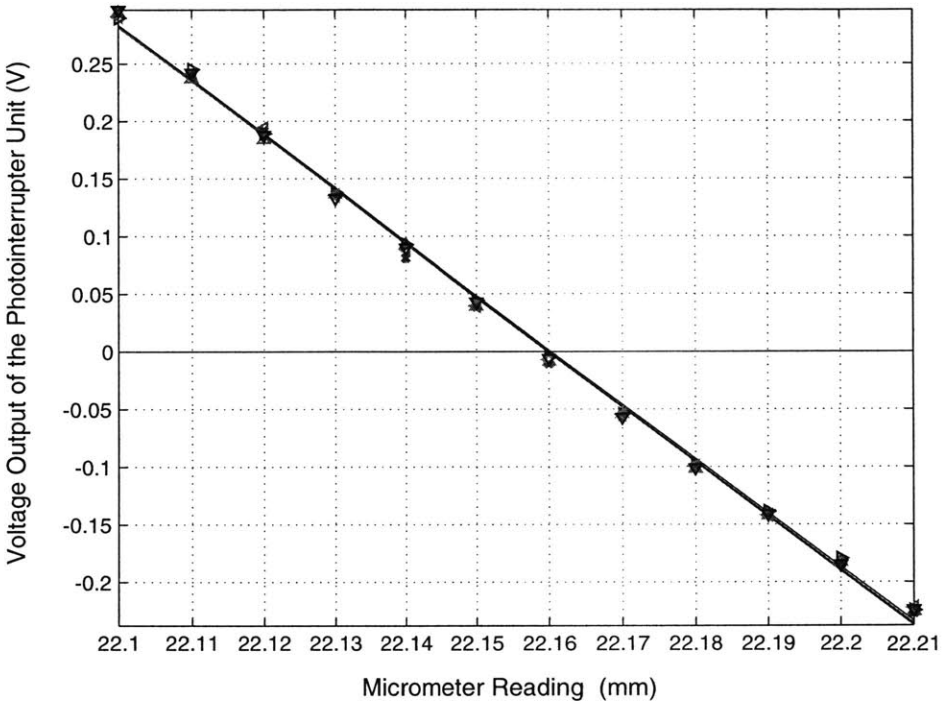

Figure 3-9: Variation of differential voltage output of the photo-interrupter unit with micrometer position. Five separate data sets are shown, for each of which a least square fit line is drawn. The position corresponding to the zero-crossing can be found from interpolation.

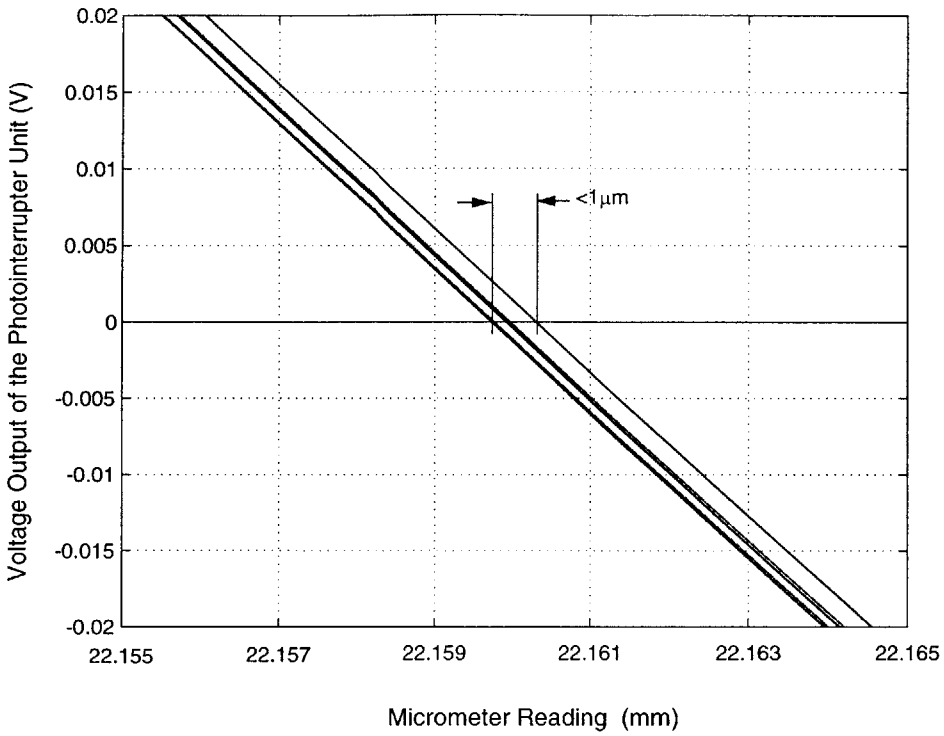

Figure 3-10: Zoomed in view of the zero-crossing in the graph of Figure 3-9. The scatter in the measured position of the zero-crossing is less than 1 μm.

crossing corresponding to this data can be found. The least square fit lines are indicated by different colors in the graph. The close match between them indicates high repeatability of our measurements recorded using the micrometer setup.

Figure 3-10 presents a zoomed view of the least square fit lines of the 5 data sets about the zero-crossing. The uncertainty in the measurement of the position corresponding to the zero-crossing can be gauged from the intercept of the zero axis contained between the lines. From the figure, this is measured to be less than 1 μm, and thus the sensor repeatability is certainly better than 1 μm. Here again, we are, as in our speckle based trials with the micrometer setup, relying on the accuracy of the micrometer. The micrometer is certainly not perfect at this level of resolution.

Chapter 4

Design of Speckle Based Metrology System

This chapter describes the design of our prototype metrology system. The speckle-based sensing system, as described in Chapter 2, consists of a laser source, a microscope lens assembly and a high-resolution monochrome CCD camera interfaced with a PC-based video capture card.

To verify the laser speckle based position sensing technique, we have initially built a micrometer actuator setup that imposes discrete angular displacements on an air-bearing spindle. For continuous torque motion, we have implemented a transmission drive run by a brushless limited angle torque motor. Here we examine the design of these actuators.

4.1 Air-bearing Spindle

The rotary precision axis in our motion system is a 4 inch diameter externally pressurized aerostatic bearing spindle[1] purchased from Professional Instruments Company

[1]The sensing capability of our speckle based machine vision sensor should be independent of the choice of the bearing, as long as the selected bearing allows for low error motions of the rotary axis. We have opted for the air-bearing spindle primarily for its low error motions.

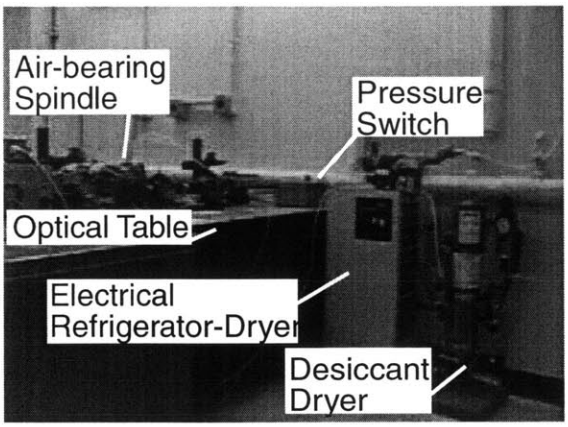

Figure 4-1: Filter-dryer unit that produces clean, dry air at 70-90 psi (4-5 atm) for use with the PI air-bearing spindle shown on the left.

(PI)[2]. This spindle is rated to have error motions of less than 25 nm and a maximum speed of 10,000 RPM. The radial and axial stiffnesses are listed as 120 N/μm and 360 N/μm respectively at pressures of 150 psi (about 10 atm). We have operated the spindle at a pressure of about 70-90 psi (about 4-5 atm), and at these pressures the load capacity and working stiffnesses are specified to be half of their rated values. Even with this reduction, the error motions are more than low enough for our purpose, making the spindle an essentially perfect axis of rotation in our metrology system.

Figure 4-1 shows a photograph of the filter-dryer unit that supplies clean and dry air to the spindle. This unit was also purchased from Professional Instruments Company. Our lab air supply available at a pressure of about 80-100 psi is passed in this unit through a deliquescent dryer and a refrigerator-type electrical dryer. Details of this setup are provided in [24]. The cleansed air is fed to the inlet ports of the spindle frame, through a pressure switch that prevents accidental start-up at lower pressures [26]. An uninterrupted compressed air supply at 70-90 psi (about 4-5 atm) is maintained using this setup.

[2]See Appendix B for vendor details.

4.2 Laser Speckle Imaging System

4.2.1 Light Source

The light source that we use for speckle generation in our metrology system is a 2 mW He-Ne laser beam of 633 nm wavelength purchased from Edmund Optics.[3] The beam divergence of our He-Ne laser is specified at a low value of 1.3 mrad. This implies that we have a nearly collimated beam directed at the spindle surface. The nominal beam diameter is 0.63 mm which corresponds to a sufficiently large (about 1 mm^2) illuminated spot.

4.2.2 Imaging System

Our imaging system consists of a low-cost analog monochrome CCD camera mounted on the back of a microscope lens assembly. Both these units were purchased from Edmund Optics.

The sensing area of the CCD camera is 6.4 mm x 4.8 mm, while its spatial resolution is given by the size 8.4 μm x 9.8 μm of each pixel in a 640 x 480 pixel array. The signal-to-noise ratio is specified as 50 dB.

Monochrome cameras have higher resolution and better signal-to-noise ratio than similarly priced color cameras. Since a color image requires more processing time and does not yield significantly more information, our choice of a monochrome camera seems appropriate. The fact that we have higher resolution at a lower price seals the deal for us.

The microscope lens assembly consists of a direct-to-video objective lens in a parfocal zoom setting, whose magnification can be varied from 2.5x to 10x. The corresponding variation in focal length is specified as the range 87.5 to 350 mm. The

[3]See Appendix B for vendor details.

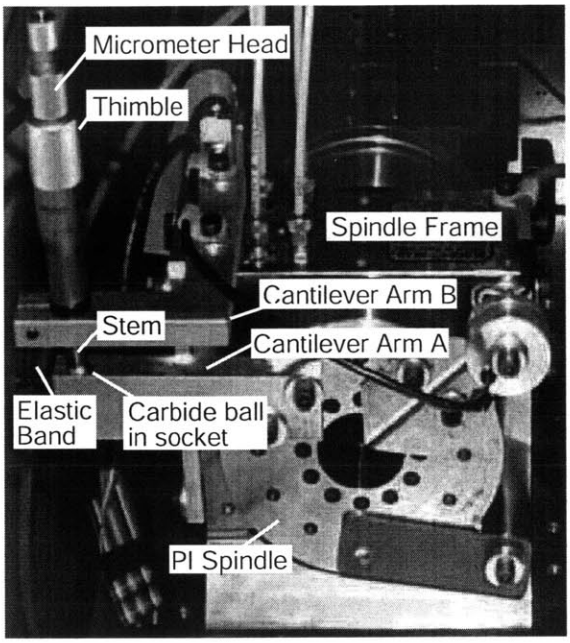

Figure 4-2: Micrometer head, with a 0.5 mm/rev screw pitch, and a 25 mm travel range, is used as a displacement source providing discrete angular motions to the PI spindle.

analog video signal from the CCD camera is transferred to a National Instruments[4] 1409 video capture card connected to a NI PXI Chassis provided with is own real-time controller. The video capture card digitizes the image at 8 bits per pixel, corresponding to a gray scale of 256 levels. The digitized image is transferred at frame rates of 30 Hz via the PCI bus to the PXI Chassis memory by an onboard DMA (Direct Memory Access) controller.

4.3 Actuator

4.3.1 Micrometer Setup

In our preliminary proof-of-concept experiments, we have verified the speckle-based sensing principle while providing discrete motions to the spindle using a manual mi-

[4]See Appendix B for vendor details.

crometer head. Two cantilever arms A and B are fixed respectively to the PI spindle and its frame as shown in Figure 4-2. A micrometer head with a 0.5 mm/rev screw pitch, and a 25 mm travel range is clamped to arm B. The thimble of the micrometer is manually rotated to push the stem down on arm A, while stretching a pre-stressed elastic band tied between setscrews fastened to the cantilever arms.

At the contact, the flat face of the stem pushes down on a carbide ball held in a socket machined in cantilever arm A. The point contact between the stem and the carbide ball ensures that the motion always applies a single-constraint along the axial direction of the micrometer, independent of small misalignments in the positioning of the socket [2].

Kinematic Relation

We now derive the kinematic relation between a small downward displacement δh of the micrometer stem and the corresponding angular displacement $\delta\theta_s$ of the PI spindle. Let us consider the geometry of the motion with respect to a right-handed coordinate system XYZ fixed to the center O of the spindle as shown in Figure 4-3.

Let C and C' respectively be the position of the center of the carbide ball before and after the stem displacement δh. The corresponding points of contact between the stem and the ball are P and P'. For the distance OC= L, $\angle$COY=β, and H=$L\cos\beta$, we have

$$\delta h = L\sin\beta - L\sin(\beta - \delta\theta_s) \tag{4.1}$$

which reduces to

$$\delta h \approx H\tan\beta(\delta\theta_s{}^2/2) + H(\delta\theta_s) \tag{4.2}$$

after preserving up to second order terms in the small angle approximations of sine and cosine functions of $\delta\theta_s$.

For values of δh of the order of 10 μm, the quadratic term in (4.2) is negligible. In

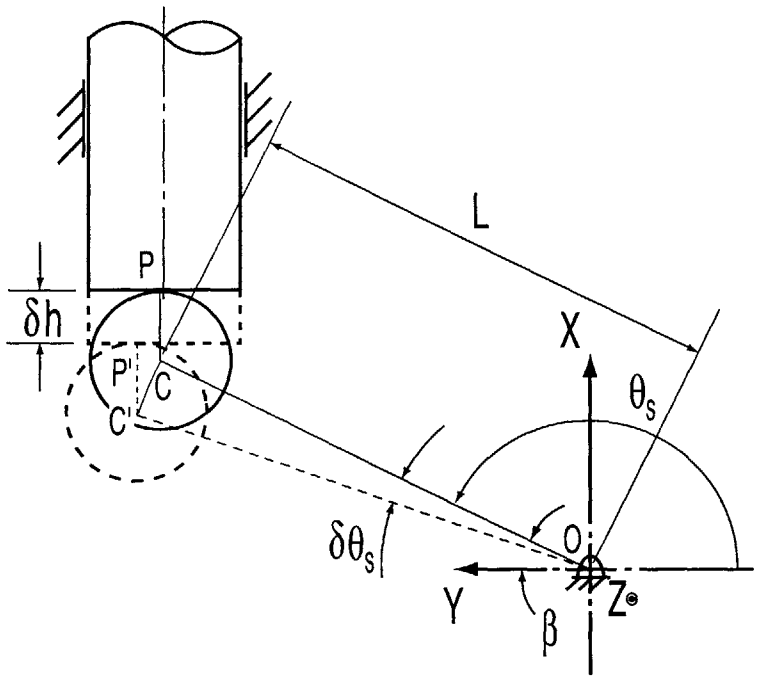

Figure 4-3: Schematic drawn to derive a kinematic constraint for rotation of the spindle using the micrometer setup.

our setup, the moment arm H=4 inch, and the radius of the PI Spindle is 2.125 inch, so the surface displacement of the spindle for a 1 μm downward displacement of the micrometer is given by 1 μm$\times$(2.125 inch/4 inch) $\approx$ 0.5 μm.

4.3.2 Actuator Drive for Continuous Torque Motion

Since we could prove that high resolution measurements are possible with speckle based sensing for discrete motions of the PI spindle by manual feed from a micrometer head, we have next examined closed loop feedback control applications where the sensor can be tested for its control performance. From possible designs, we have chosen a brushless limited angle torque motor to turn the PI spindle through a string tied between the motor shaft and the spindle. A higher-performance version of this system might use a steel band to replace the string, or eliminate the transmission with a direct-drive setup.

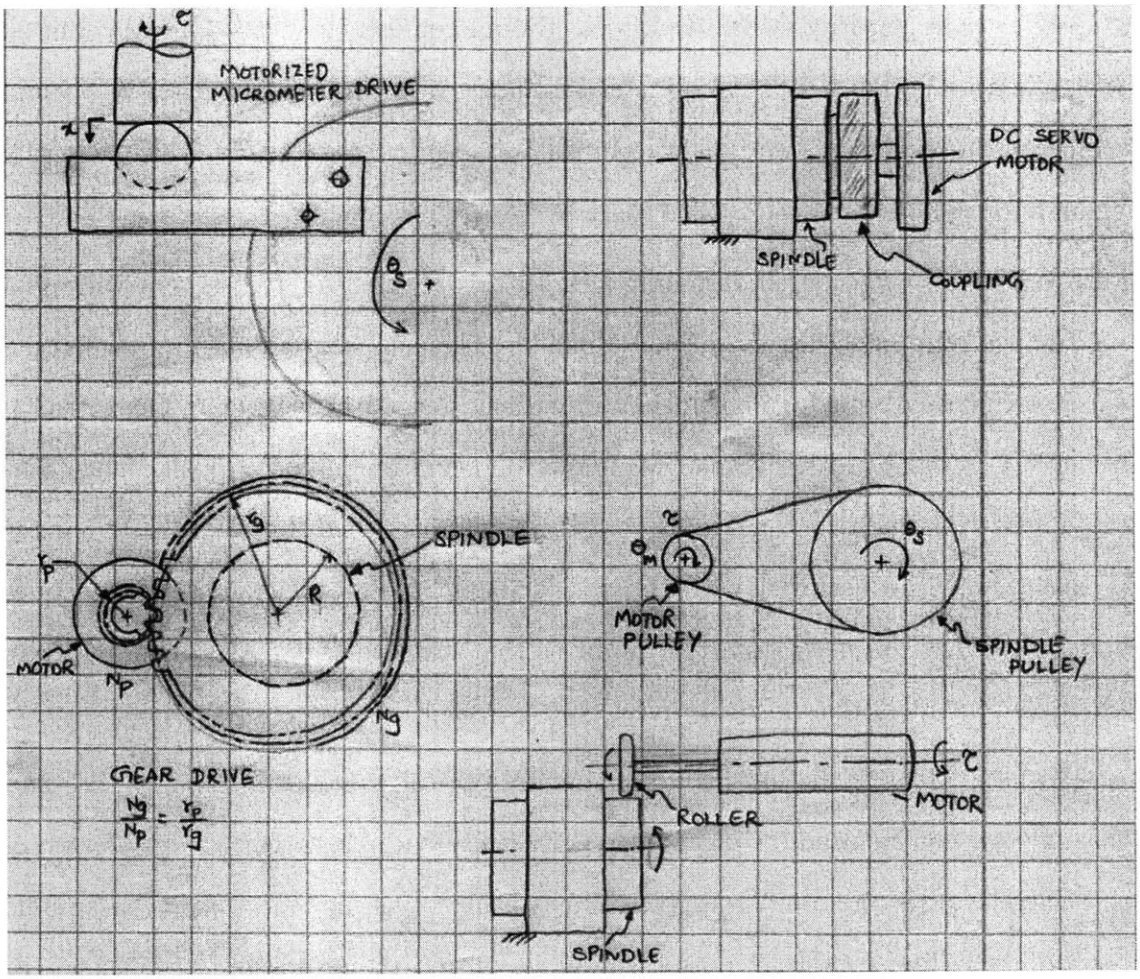

Figure 4-4: Design candidates for implementing an actuator drive to provide continuous torques to the spindle.

Candidate drive designs

Figure 4-4 shows the candidate designs we have examined before choosing to develop our transmission drive.

A motorized micrometer is an obvious choice after our preliminary experiments using a manual micrometer head. From among similar priced designs, the resolutions and travel ranges that can be obtained for motion with a motorized micrometer are relatively low. Further, backlash in the micrometer screw mechanism can be a significant source of error in our measurements.

As an example, PiezoMike, a piezoelectric micrometer drive produced by Physik Instrumente [3] claims sub nano-meter resolution over fine travel ranges of 30 μm. However, the dynamic operation is specified as being limited to 10 Hz, which is hardly enough for our purposes.

We have also considered designing a direct drive consisting of a servomotor and a mechanical coupling attached to the PI spindle. The main constraint in implementing this design is achieving high resolutions of motion, so that the motor can be controlled for sufficient bandwidths. Since we know from our preliminary experiments that our speckle based measurements have low sample rates, high bandwidths for motor control cannot be achieved with the speckle-based sensor. An additional encoder and tachometer are needed on the motor so that position and velocity feedback are available to control the motor torque.

We have installed a Renishaw incremental optical encoder on our spindle, and this encoder can be used for providing position feedback. However, the resolution of this encoder after quadrature digitization is 5 μm of surface motion of the spindle per dSPACE line count. This resolution is far too coarse for our purposes. To implement velocity feedback, an additional tachmoter is required, or some external (electromagnetic or hydraulic) damping should be provided.

Reasonably priced servomotors available with AeroTech [4], Maxon [5] and other common commercial suppliers have integral encoders with, at the maximum, 4000 cycles/rev, which corresponds to a surface resolution of $2\pi \times 2.125$ inch/4000 ≈ 84.8 μm which, again, is too coarse for our purposes.

The developmental effort with the direct drive appeared to be substantially larger than that with the simpler, low-cost solution of a transmission drive using a brushless limited angle torque motor and a string tied between the motor shaft and the PI spindle. This motor is provided with an integral optical sine-cosine encoder of resolution 1100 cycles/rev. When the analog sine-cosine outputs of the encoder are

interfaced with the analog encoder channel of a dSPACE DS1103 board, a surface resolution of 0.07 μm is obtained for the 0.25 inch motor shaft. At this high resolution, differences between successive counts of the encoder can be used to derive a velocity measurement, thus eliminating the need for a separate tachometer. The details of our dSPACE control implementation are discussed in Chapter 5.

Other possible transmission drives include a gear drive and a roller drive. Backlash is again a significant error source in gear drives, and many anti-backlash mechanisms have been developed to tackle this problem. A roller drive serves as a robust design, since there is minimal compliance in the transmission load path. Though these designs are equally acceptable choices, we have not implemented them in our system.

Drive Implementation

Our implementation of the actuator drive is shown in Figure 4-5. The rotary actuator in our transmission drive is a brushless limited angle torque motor and the transmission element is a string (dental floss) tied between the motor-shaft and the PI spindle.

Figure 4-6 illustrates the construction of the brushless torque motor with a specified active range of 120° and its integral incremental optical sine-cosine encoder. This motor is a Lorentz-type electromagnetic actuator with an iron core stator around which a coil is wound in two sections with opposite polarities [25]. The rotor is a permanent magnet that spins while maintaining a constant gap between the magnetic poles and the iron core. A cross-section of the actuator is shown in Figure 4-7.

The motor is driven by a PA-21 power amplifier set at a gain of 2. This amplifier is supplied with a voltage of $\pm$15 V from two 0-30 V supplies of a Tektronix Power Supply operated in a series mode. An analog circuit built on a protoboard is used to interface the output of the sine-cosine encoder with the analog encoder channel of dSPACE. This circuit is discussed in Section 4.3.2. The schematic showing the motor

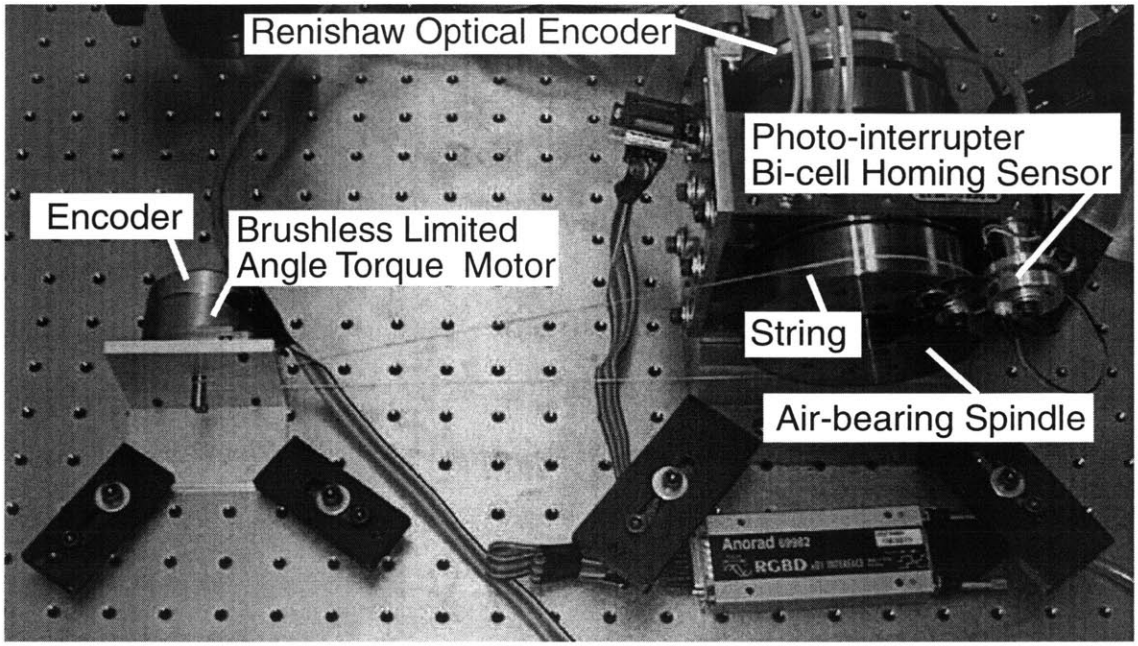

Figure 4-5: A photograph of the transmission drive used in our implementation of our speckle based metrology system. The transmission element in this drive is a pre-stressed string tied between the shaft of the brushless limited angle torque motor and the PI spindle.

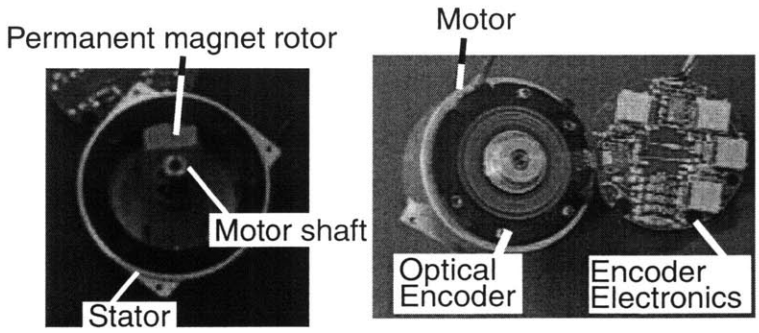

Figure 4-6: A photograph of our brushless limited angle torque motor taken apart to illustrate its construction. An optical sine-cosine encoder mounted on the back of the motor resolves the motion of the 0.25 inch motor shaft at 1100 cycles/rev.

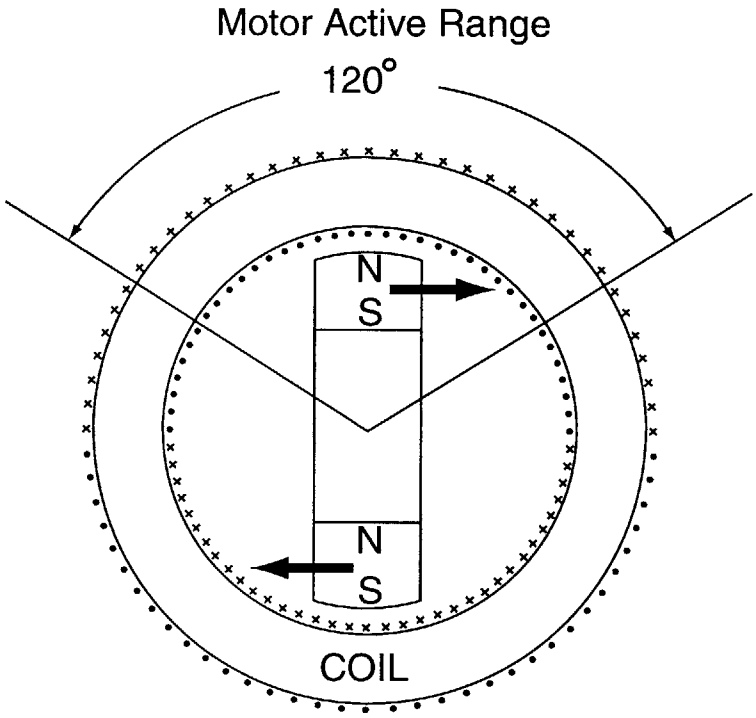

Figure 4-7: Schematic illustrating the principle of our brushless torque motor. Current coming out of the page is marked as dots and current going into the page is marked as 'x'. In the given configuration, a clockwise torque is generated on the rotor. This picture is taken from [25].

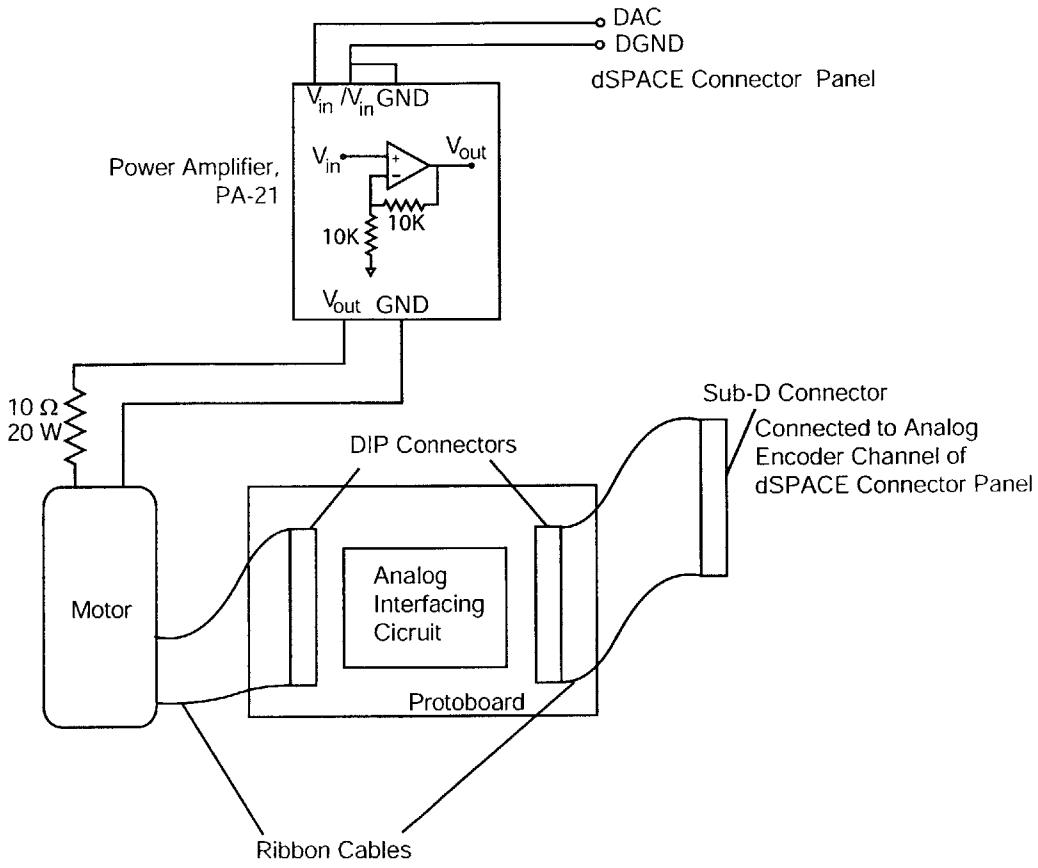

Figure 4-8: Schematic showing the motor connections of our setup. A PA-21 power amplifier set at a gain of 2 drives the motor. An analog circuit built on a protoboard connects the analog encoder outputs to dSPACE. This figure is based on a schematic given in [25].

connections of our setup is given in Figure 4-8. The specifications of the motor are given in Table 4.1. Since we do not have any stringent torque requirements for the spindle operation, the low torque rating does not affect us. In testing the speckle-based sensor over small ranges of motion of the order of 100 μm, the motor active range of 120° is more than sufficient.

This motor has been purchased from Servo Systems Company[5] and used in the MIT 2.737 Mechatronics Laboratory class, taught by Professor Trumper, in a lab exercise on brushless motor control [25]. Here, two of these actuators, attached with a

[5]See Appendix B for vendor details.

Active Range	$\pm 60^\circ$
Torque constant K_t	0.038 Nm/A
Peak Torque	0.091 Nm
Rotor Inertia J_m	1.34×10^{-5} kg m^2
Viscous Damping B_m	4.5×10^{-4} Nm/(rad/s)
Resistance R	3.7 Ω

Table 4.1: Brushless limited angle torque motor: Characteristics.

flexible coupling, are commutated electronically to control torques over a full rotation of the motor shaft. Commutation is not necessary in our case since we are interested in a limited range of motion.

In our case, for controlling the torques of the motor over its active range, we model the motor as a typical DC servomotor with first-order characteristics. For a voltage $V(s)$ applied at to the motor, the angular velocity of the motor shaft $\Omega_m(s)$ is given as

$$\Omega_m(s) = V(s) \frac{\frac{K_t}{R}}{J_m s + B_m + \frac{K_t^2}{R}} \tag{4.3}$$

In Chapter 5, we measure the frequency response of the motor and check if it conforms to our model in Eq. 4.3. This model is actually inadequate and we would need to modify it to account for dynamics in the roller-element bearing supporting the motor shaft to the casing.

Encoder Interface

The dSPACE DS1103 board has an encoder channel for interfacing analog encoder inputs in either the voltage (with a maximum allowable voltage of signal 1V peak-to-peak) or the current mode (with a maximum allowable current of signal 11 μA peak-to-peak). Kendale [20] observed a steady drift of encoder counts while using this channel in the voltage mode. In troubleshooting the output, Kendale observed that the magnitude of the sine-cosine waveforms dropped after connecting them to the dSPACE board.

To avoid such loading problems, we passed the sine-cosine outputs of the encoder through unity-gain buffer amplifiers as as shown in Figure 4-9. Because of its high input impedance, the unity-gain buffer draws hardly any current from the encoder. The low output impedance of the buffer ensures that the interfacing circuits of the dSPACE analog encoder channel are not loaded.

Further, the dSPACE encoder channel needs differential sine-cosine inputs. Since the outputs from our encoder are not differential, we have generated the complementary sine-cosine outputs using a LM741 op-amp in an unity-gain inverting configuration. With this implementation in the voltage mode, we have not observed any drift in encoder position such as Kendale [20] observed.

Drive Modeling

Figure 4-10 shows the dynamic model of the transmission drive, with rotary inertias J_m and J_s, and damping B_m and B_s, respectively for the motor and spindle. For a torque τ_m applied to the motor, the motor shaft rotates by an angle θ_m. This motion is transmitted via the string to the spindle as a rotation θ_s, in the presence of disturbance torques τ_{dm} on the motor and τ_{ds} on the spindle. The tension on the upper slack side of the string and the lower taut side are denoted as F_1 and F_2 respectively. If the pre-load tension in the string is F_p, the tensions under dynamics conditions are given by

$$F_1 = F_p - K\delta \tag{4.4}$$

$$F_2 = F_p + K\delta \tag{4.5}$$

where for an Young's Modulus specified at E, and the area of cross-section A, the portion of the string of length L on either side is modeled as a linear spring of stiffness $K = EA/L$. The axial deformation of the string (elongation on the taut side and

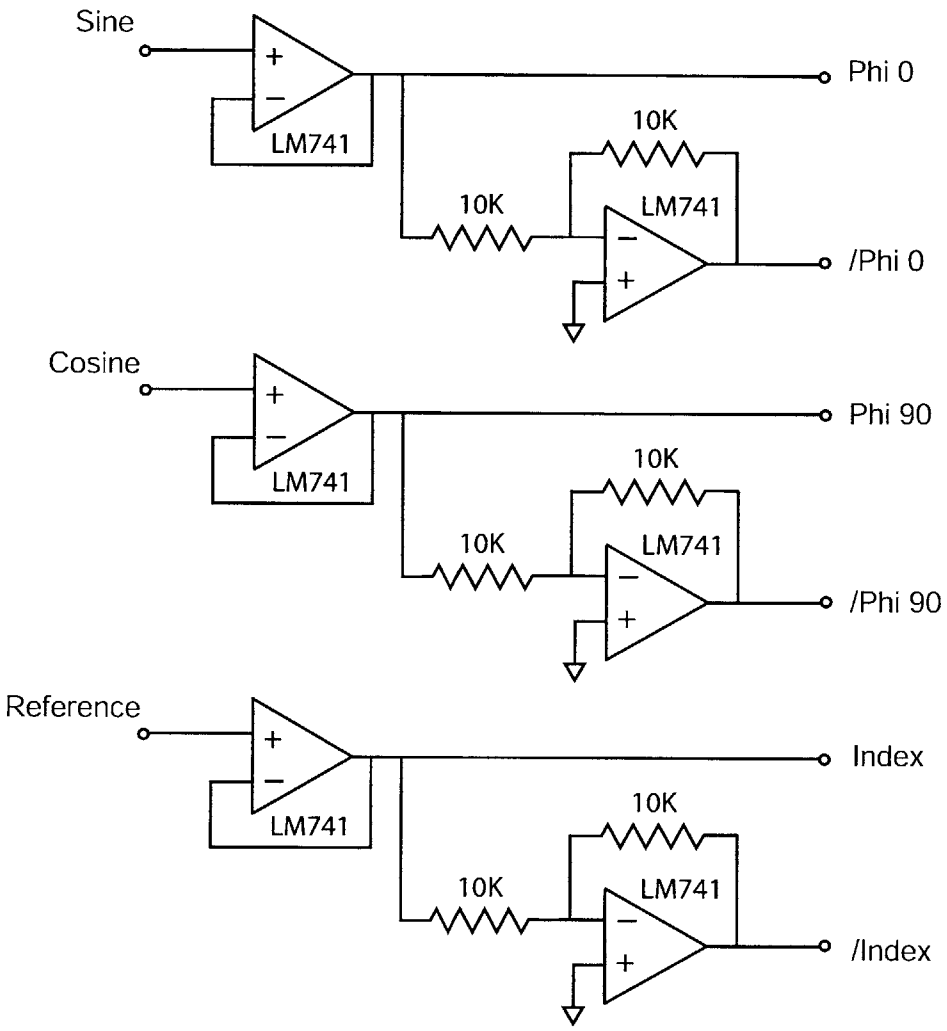

Figure 4-9: Analog interfacing circuit that we built on a protoboard for connecting the encoder sine-cosine outputs to the dSPACE analog encoder channel in a voltage mode. By using an active circuit with unity feedback buffer amplifiers, the output impedance of the signals is reduced so that the encoder channel of dSPACE is not loaded.

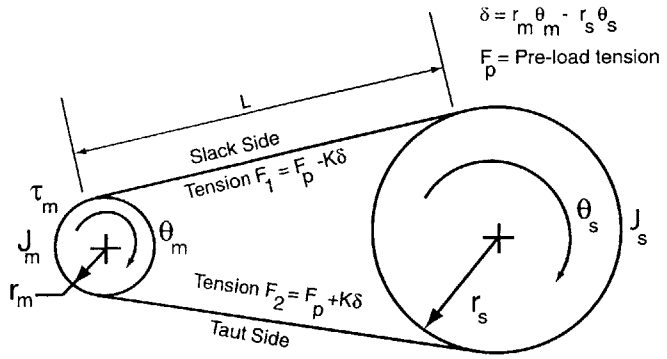

Figure 4-10: A dynamic model representing our transmission drive.

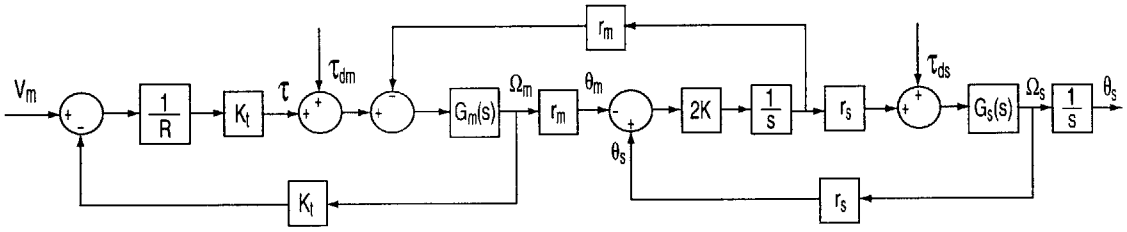

Figure 4-11: Control block diagram of the transmission drive.

compression on the slack side) has a magnitude $\delta = r_m\theta_m - r_s\theta_s$.

By applying angular momentum principle about the centers of the motor and the spindle, we obtain the following equations of motion for the system.

$$J_m\ddot{\theta}_m = \tau_m + (F_1 - F_2)r_m + \tau_{dm} - B_m\dot{\theta}_m \tag{4.6}$$

$$J_s\ddot{\theta}_s = (F_2 - F_1)r_s + \tau_{ds} - B_s\dot{\theta}_s \tag{4.7}$$

This system is the torsional equivalent of the canonical two mass-spring-damper system. A control block diagram representing the model is presented in Figure 4-11 which simplifies to the form shown in Figure 4-12 in the absence of external disturbance torques τ_{dm} and τ_{ds}.

We compare the frequency responses as obtained from this model with the measured response in Chapter 5, before we proceed to implement feedback control using

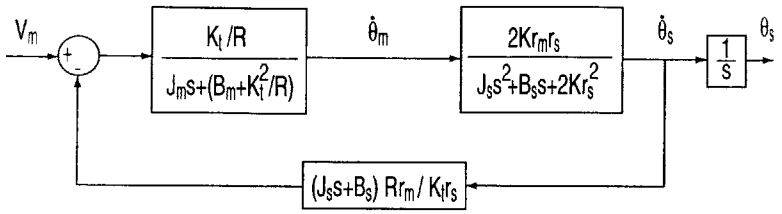

Figure 4-12: Simplified form of the control block diagram shown in Figure 4-11.

the optical encoder provided with the motor and the laser speckle based machine vision sensor.

Chapter 5

Control Implementation

In this chapter, we describe the control performance of our speckle-based sensor. We have implemented closed-loop control of position of the spindle using speckle-based feedback. The loop transmission of the system has a cross-over frequency of 1 Hz and a phase margin of 40°. The closed-loop system -3 dB bandwidth is about 2 Hz, while the sample rate of the speckle-based sensor is 10 Hz.

Here, we discuss schemes of minor loop compensation that we have developed for our system. We perform small-signal excitation over the desired range of frequencies using a dSPACE/Simulink based DSA tool developed by Lilienkamp et al [31]. We compare and upgrade the dynamic models that we proposed in Chapter 4 to explain the system dynamics thus measured in the frequency domain. Since the sample rates of our current speckle-based sensor implementation are low, the achievable closed-loop system bandwidth is low. Finally, we study the system response in the time domain as well.

5.1 dSPACE Implementation

In Chapter 2, we have discussed the implementation of speckle-based estimation of position using LabVIEW-based algorithms run on the NI real-time controller. The

motion control application for our laser speckle-based metrology system is built using a dSPACE[1] DS1103 controller board.

The dSPACE DS1103 hardware is a PC-based rapid prototyping development system with a 400 MHz PowerPC processor. The board has an input/output (I/O) connector panel with 20 analog-to-digital ADC channels and 8 digital-to-analog DAC channels.

Control block diagrams are built in MATLAB/Simulink, which are then converted to real-time C code using MATLAB Real-time Workshop. dSPACE Real-time Interface software links this code for execution on the controller board. We access in real-time the parameters and data on the board from ControlDesk. With this configuration[2], the motion system can be run for different control algorithms at a chosen fixed execution step size of 0.1 ms (corresponding to a sample rate of 10 kHz).

Encoder Channels

The DS1103 controller board also provides channels for incremental encoder outputs, 6 for encoders with digital outputs and 1 for those with analog outputs. The digital channels have a 24-bit counter and 4-fold line-subdivision, while the analog channel has a 32-bit counter, and a 256-fold line sub-division.

In our implementation, we have interfaced with the analog channel sine-cosine outputs of the optical encoder provided with the motor. This encoder measures the angle of the 0.25-inch diameter motor shaft at a resolution of 1100 cycles/rev. With the 256-fold sub-division of dSPACE, we obtain theoretical resolutions of 0.07 μm for displacement of the surface of the motor shaft. As discussed in Chapter 3, the Renishaw encoder interfaced with the digital encoder channel has a resolution of 5μm of surface motion per dSPACE line count.

[1]See Appendix B for vendor details.

[2]The Simulink models and LabVIEW VI developed as part of our implementation are included in Appendix A.

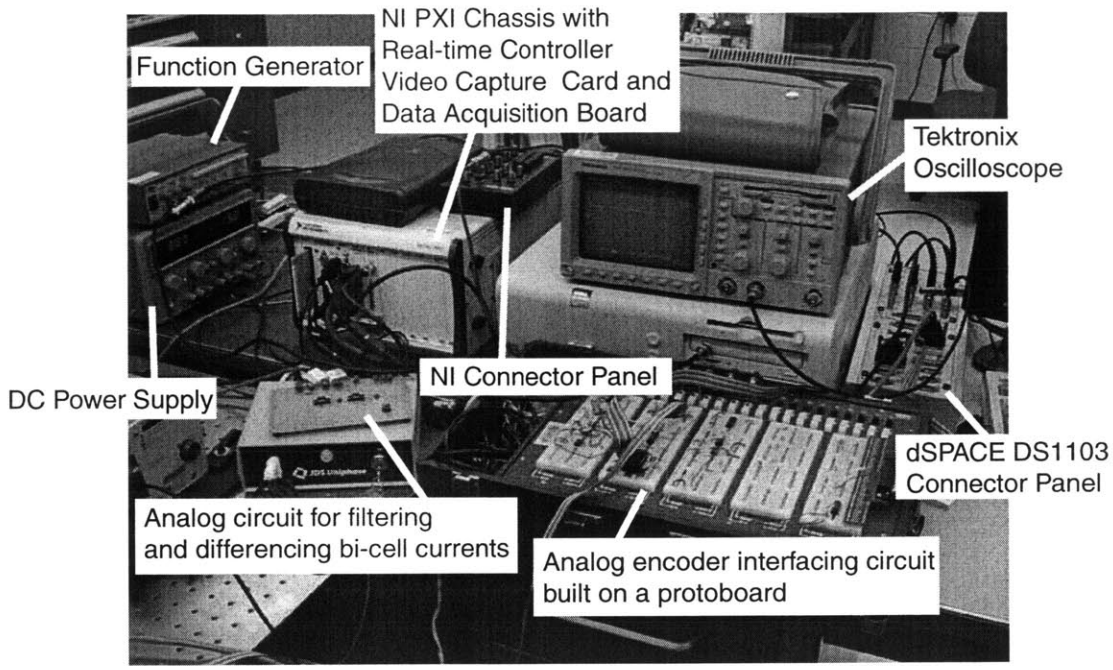

Figure 5-1: A photograph of our real-time hardware instrumentation showing the dSPACE and NI PXI-based sytems.

5.2 Real-time Setup

Figure 5-1 shows a photograph of the dSPACE and NI PXI-based systems that we have used in our real-time implementation of the speckle-based metrology system. Figure 5-2 shows a schematic depicting our metrology system. A brushless limited angle torque motor drives the air-bearing spindle through a string tied between the motor-shaft and the spindle. The motor is driven in a voltage mode through a power amplifier, whose voltage, in turn, is commanded from dSPACE. The position sensor on the motor end of this transmission drive is the optical encoder mounted on the back of the motor. We derive angular velocity using the difference between successive counts of the encoder as a virtual tachometer.

The position of the air-bearing spindle is measured by the laser speckle-based machine vision sensor. As described in Chapter 2, this sensor consists of an imaging system, a video capture card, and a NI-PXI system based image processing unit. The

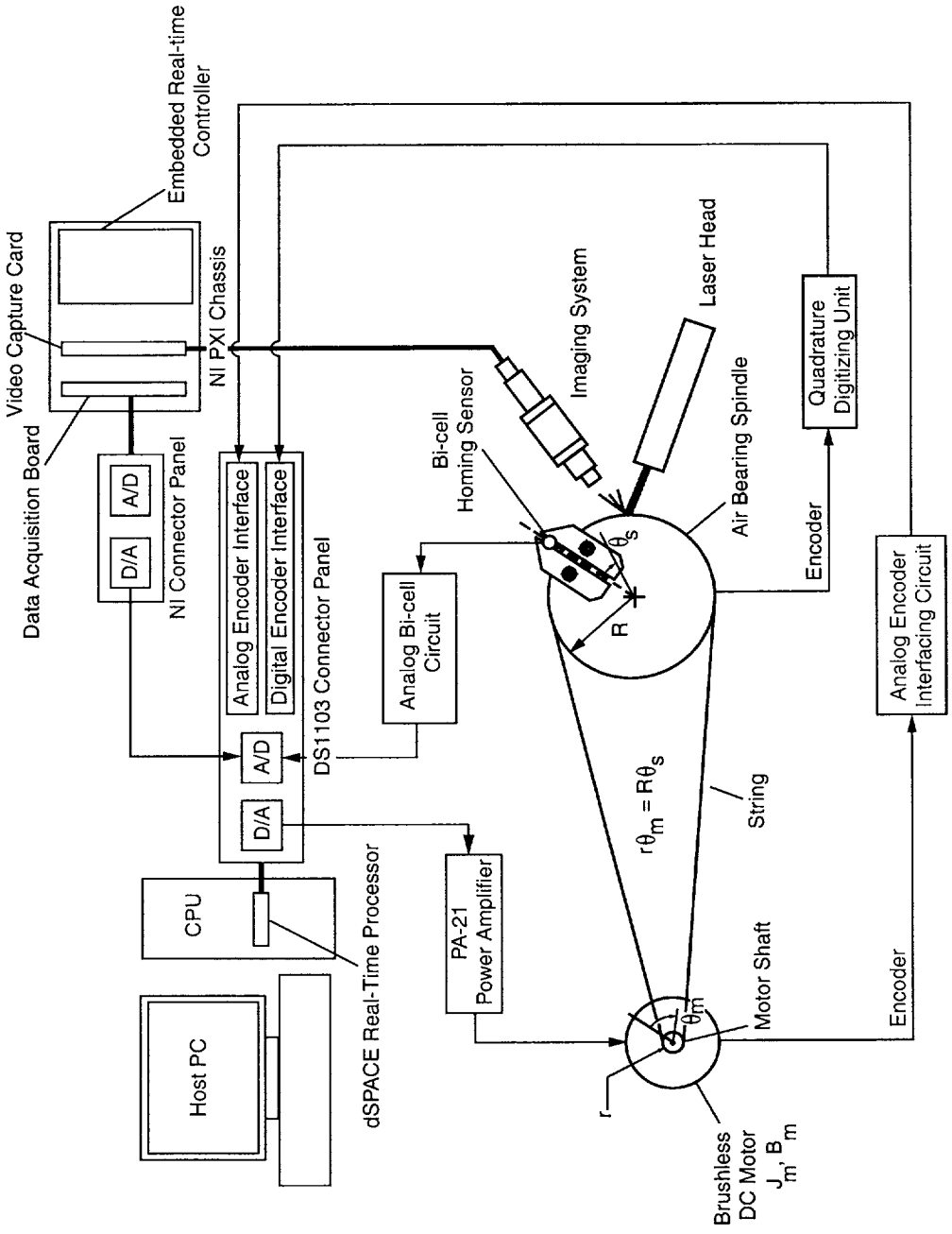

Figure 5-2: Schematic of the laser-speckle based real-time machine vision sensor for an air-bearing spindle.

speckle-based position estimated using this sensor is scaled up in the LabVIEW-based algorithms to an equivalent voltage value. This value is converted to an analog signal in the DAC of the NI Data acquisition board and fed to an A/D channel of dSPACE.

We calibrate our speckle sensor against the Renishaw incremental encoder system, whose digitized outputs are interfaced with the digital encoder channel of dSPACE. The reference signal for this encoder is derived from the photo-interrupter bi-cell unit interfaced with another A/D channel of dSPACE.

5.3 Control System

Figure 5-3 shows the control block diagram of our speckle based metrology system. The speckle-based estimate $\hat{\theta}_s$ of spindle position is converted to an analog voltage value V_{sa}. This voltage is read in dSPACE as a digital value V_{sd}. Converting the speckle-based position estimate to an analog representation V_{sa} comes handy in debugging the system by monitoring the analog signals on an oscilloscope.

The error signal E_I is obtained as a difference between the reference voltage V_{ref} and V_{sd}. This error is driven to zero in steady state by an integral controller with a gain K_I.

A pair of nested minor loops, the inner for velocity and the outer for position are used to control the motor. The feedback in the velocity loop is angular velocity Ω_m of the motor derived from the difference between successive counts of the optical encoder provided with the motor. The velocity controller is a proportional gain K_v.

Similarly, in the position loop, the feedback is the motor angle θ_m measured by the optical encoder and the position controller is a proportional gain K_p.

The digital voltage V_m is applied to the PA- 21 power amplifier which drives the motor and the spindle through the transmission drive. The power amplifier is set at a gain of 2.

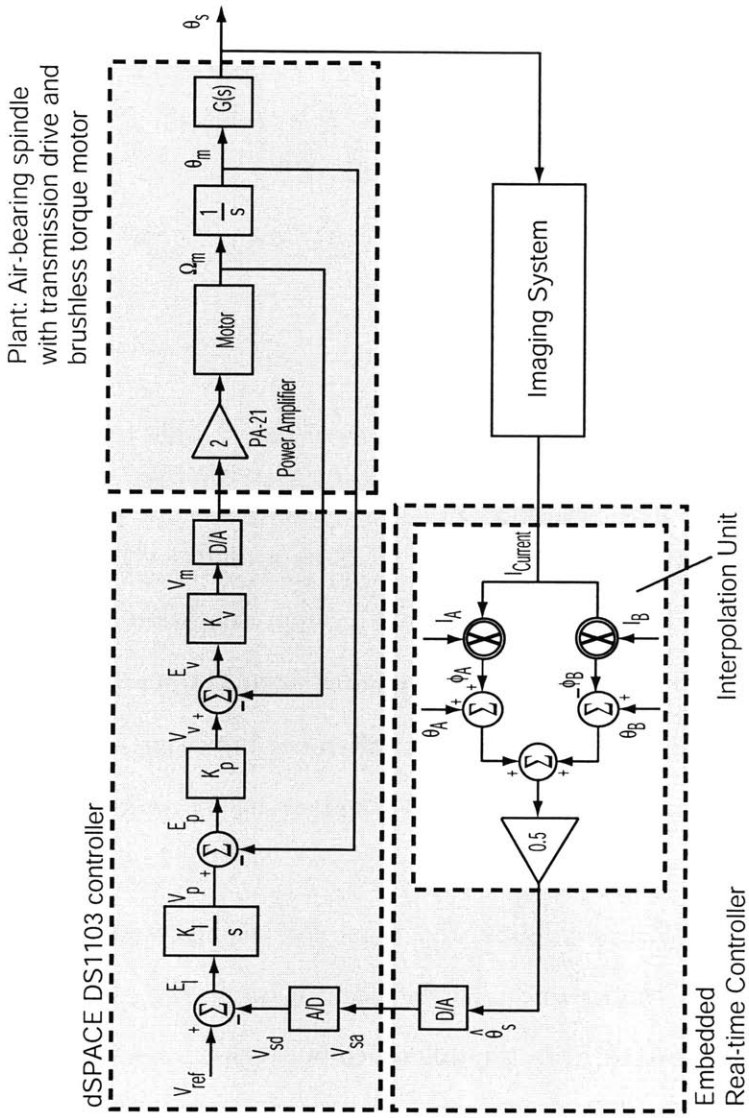

Figure 5-3: Control block diagram of our laser speckle-based metrology system.

In the feedback path of the major loop on the NI real-time system, the current image $I_{current}$ is compared against two pre-stored library images I_A and I_B to generate a position estimate $\hat{\theta}_s$. This estimate is output as the analog voltage V_{sa}.

5.4 Operation

Figure 5-4 presents the schematic describing the operation of our control system. The sequence of steps that we follow in implementing closed-loop control of position of the spindle is presented below. The actual software implementation of these steps is detailed in Appendix A.

1) Keep switches S_1 and S_2 in *State B*. Apply a reference voltage V_p for the position minor loop to run the spindle with low torque inputs from the motor.

As the spindle rotates, the razor blades containing the slit move between the LED and the bicell of the photo-interrupter unit. Zero the count of the Renishaw encoder when the differential signal of this unit hits a zero-crossing. This position is indicated as the angle θ_r in Figure 5-4.

2) From the zero of the Renishaw RGR encoder, rotate the spindle by +X encoder counts, where X corresponds to half the pitch of the speckle image library. Capture the speckle image I_A corresponding to this position θ_A. In our implementation, we have chosen $X = 6$, which corresponds to a $30\,\mu$m surface motion.

3) Repeat Step (2) now rotating the spindle by -X encoder counts to position θ_B from the zero position.

4) Run the speckle interpolation algorithm that calculates interpolated estimates of position based on the two stored speckle images.

5) Flip switches S_1 and S_2 to *State A* to implement the closed-loop system. The switches S_1 and S_2 are constructed in Simulink as Switch blocks that propagate a zero when the switch is in State B, and the control signal when the switch is in State

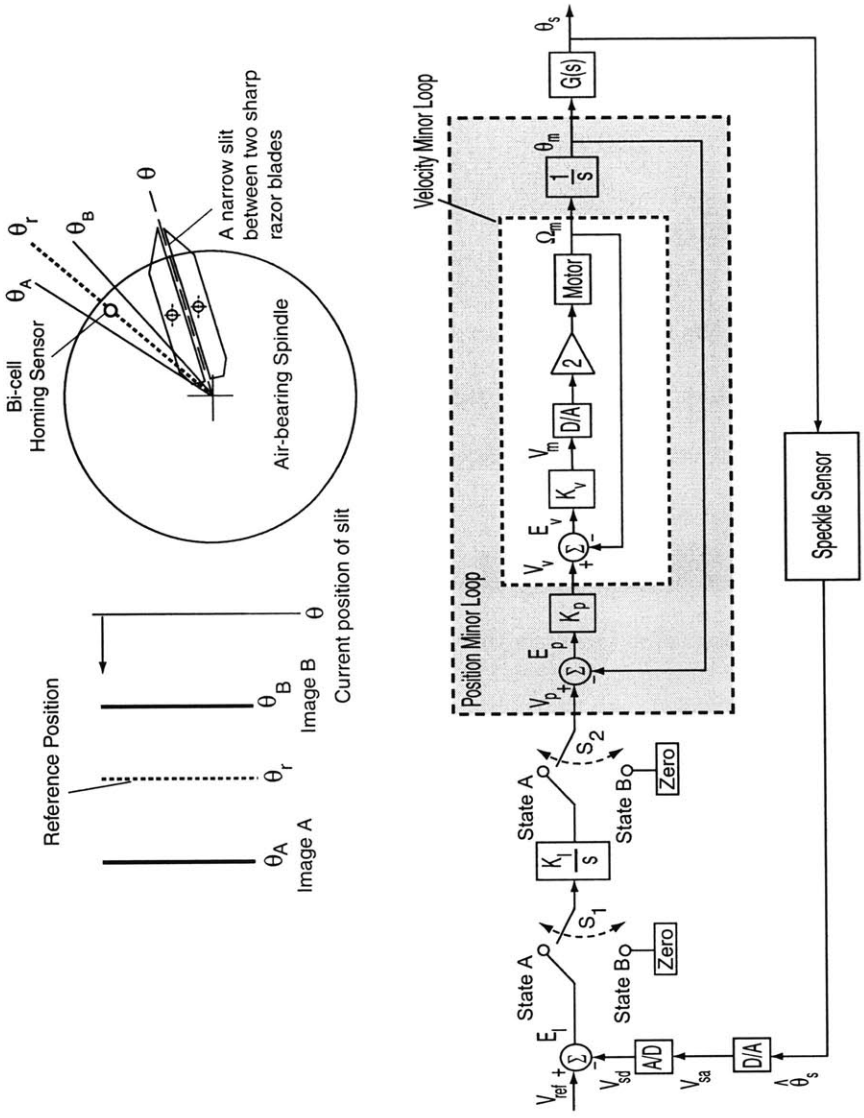

Figure 5-4: Schematic depicting the operation of our laser speckle metrology system. First, the motor is controlled for its position by implementing the velocity and position minor loops. Switches S_1 and S_2 are kept in *State B*. For a given voltage command V_p, the controlled torque of the motor drives the spindle through the string. When the bi-cell current output hits a zero-crossing, the encoder count of the spindle is triggered. Speckle images are captured at a surface displacement of $\pm 30\,\mu$m about this position. The angles shown in figure are not drawn to scale. Image processing algorithms are initialized and run to generate an interpolated position estimate. Finally, switches S_1 and S_2 are flipped to *State A* to complete the speckle-based major loop.

A. That is, when the switches S_1 and S_2 are open, the input to the integrator block is zero and V_p is independent of our speckle-based measurements. When the switches S_1 and S_2 are closed, the closed-loop system error E_I is reduced to zero in the steady state by the integrator block.

5.5 Minor Loop Compensation

In our implementation, we have two minor loops, one for velocity and the other for position of the motor. The major loop is the one with the speckle-based position feedback obtained from our machine vision sensor.

In the case of nested minor loops, each inner loop is designed to have a cross-over frequency of the order of 10 times higher than that of the immediate outer loop containing it. We have chosen to implement a cross-over frequency of 150 Hz for the velocity minor loop and 20 Hz for the position minor loop. The cross-over of the speckle major loop is chosen to be about 1 Hz.

5.5.1 Motor Modeling

The data points marked as 'x' in Figure 5-5 represent the measured frequency response of the open loop transfer function between the encoder position $\theta_m(s)$ and the applied voltage $V_m(s)$, of the motor alone. That is, the string is not wrapped around the motor shaft. The dynamics clearly differs from that predicted with the usual servomotor model that we described in Section 4.3.2 of Chapter 4. The model, marked as the solid curve, is an integrator at low frequencies and hits a first order pole at a frequency of about 6.5 Hz, after which the magnitude drops off at a rate of -40 dB/dec. In contrast, the measured response indicates that the motor behaves as a spring at low frequencies.

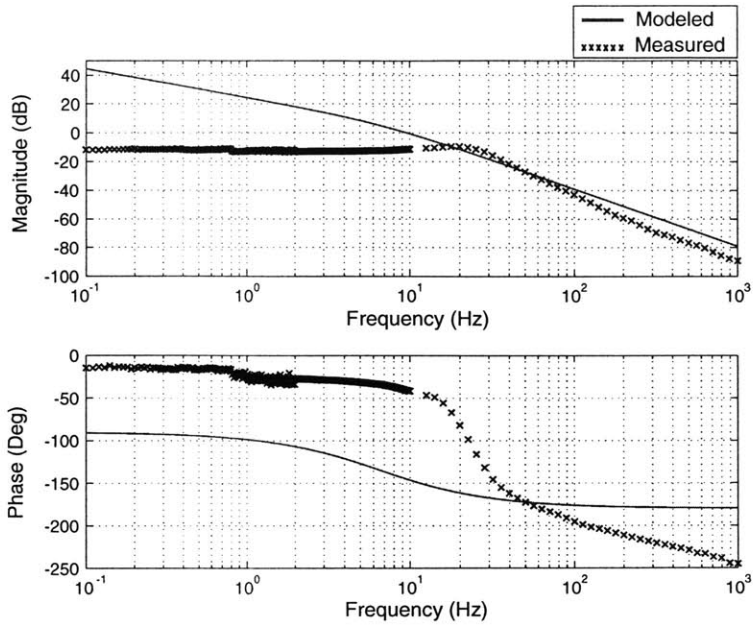

Figure 5-5: Frequency response of the transfer function between position $\theta_m(s)$ and applied voltage $V_m(s)$ of the motor without the string wrapped around its shaft.

Non-linear behavior at low frequencies

Ludwick [28] observed spring-like behavior at low frequencies with a servomotor used in his diamond-turning machine setup. He noted that the response at low frequencies varied with the amplitude of the sine excitation and predicted that this non-linear springy effect could be due to torque cogging in the motor. Cogging does not apply to our case since we do not have any slots in our motor.

We have then performed experiments varying the drive amplitude with our setup. We have used a drive amplitude of 0.04 V in dSPACE for the DSA tool to collect the data presented in Figure 5-5. As indicated in Figure 5-6, when the drive amplitude is increased in the range 0.04-1.2 V, the resonance peak shifts to lower frequencies indicating a reduction in the stiffness of the spring. For reduction in the resonance frequency by about 1.8 times, the stiffness in the graph is elevated by about $20\log_{10}(3.24) \approx 10.8$ dB, which makes sense. We suspect that this non-linearity in the response at low frequencies arises from frictional effects in our motor. A possible

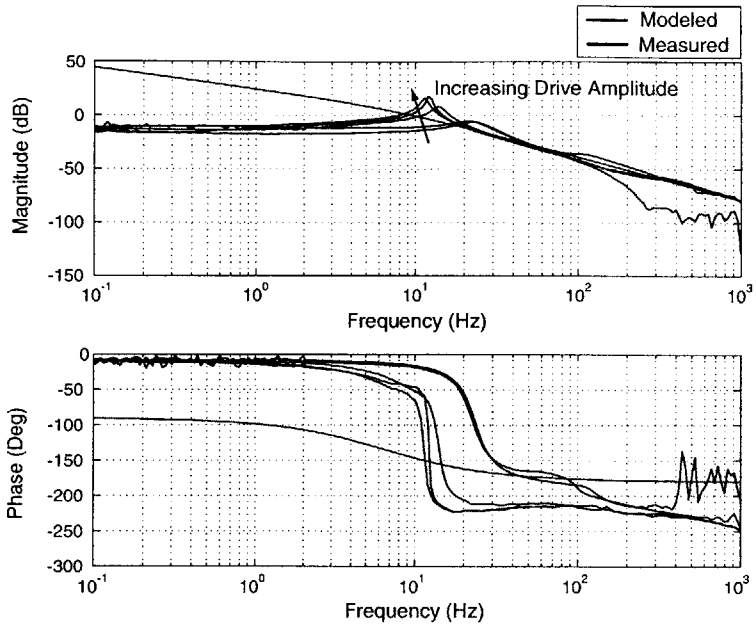

Figure 5-6: The frequency response measured in Figure 5-5 is recorded again for varying drive amplitudes. With increasing amplitude, the resonance peak shifts to lower frequencies and higher stiffnesses.

source is solid friction in the roller element bearing (shown in Figure 5-7) supporting the motor shaft in the casing. Dahl [29] studied the effect of solid friction in damping of mechanical vibrations and proposed a non-linear model describing the frictional effects at low frequencies. This phenomenon has been termed the Dahl effect and has been observed in actuator setups used with disk drives. We have not used this non-linear model in our control algorithm. In any case, as far as control is concerned, it is only the high frequency part of the response which matters. This portion of the response is unaffected by the Dahl phenomenon.

Modified motor model

We now upgrade the model of the motor given by Eq. 4.3 to take into account the resonance from the bearing friction observed in the measured response of Figure 5-5. We add a spring in our model and also additional damping to match the modeled curve with the experimental curve as shown in Figure 5-8. This second order system

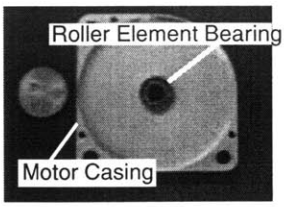

Figure 5-7: Roller element bearing supporting the 0.25 inch diameter motor shaft in the motor casing. A cent is shown in the photograph to indicate the length scale. We suspect that the mechanical friction in the bearing, causes a resonance in the measured frequency response of Figure 5-6.

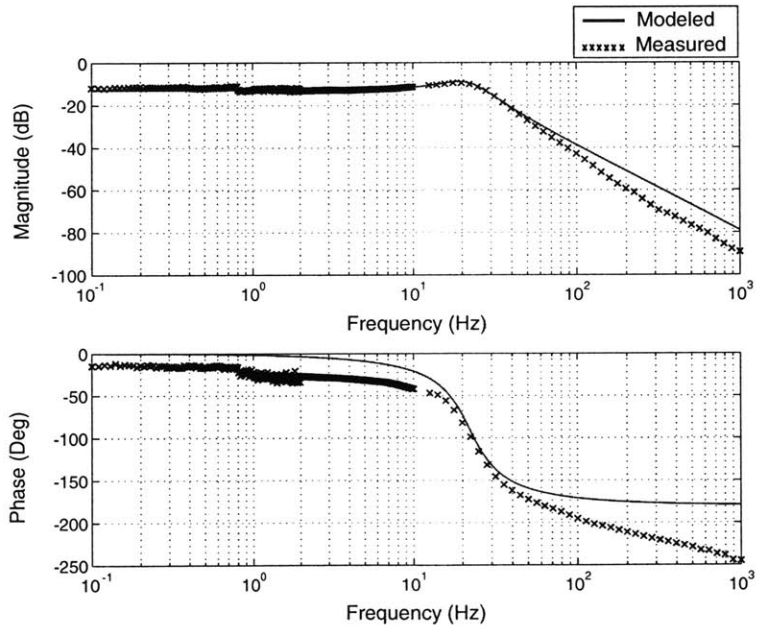

Figure 5-8: Modeled and measured frequency response of the transfer function $\theta_m(s)/V_m(s)$ for the motor with out the string wrapped around the motor shaft.

is underdamped, with an undamped natural frequency of 22.17 Hz and a damping factor of 0.34. The transfer function between the angle of the motor $\theta_m(s)$ and applied voltage $V_m(s)$ is calculated as[3]

$$\frac{\theta_m(s)}{V_m(s)} = \frac{4438}{s^2 + 94.02\ s + 1.94\times 10^4} \tag{5.1}$$

The stiffness of the spring used in this model is 0.26 Nm/rad. The additional damping factor is 7×10^{-4} Nm/(rad/s).

5.5.2 Drive Modeling

Here, we include the motor model of Eq. 5.1 to the drive model proposed in Section 4.3.2. The modeled transfer function between the angle θ_m and voltage V_m applied to the motor[4] assumes the form given by

$$\frac{\theta_m(s)}{V_m(s)} = \frac{4438\ s^2 + 2.21\times 10^4\ s + 9.1\times 10^6}{s^4 + 372.6\ s^3 + 9.52\times 10^4\ s^2 + 5.64\times 10^5\ s + 3.98\times 10^7} \tag{5.2}$$

The values of the parameters that we used in our model are listed in Table 5.1.

In obtaining the best fit between the experimental data and the model, we have tuned some of the parameters. A stiffness of 2300 N/m of the string implies that a mass of 1 kg hung from it extends it by nearly 4 mm, which feels about right in the order of magnitude. To damp out the sharp peaks that we obtained from initial trials, we added a damping factor of 5 Ns/m for the string and increased the motor viscous damping to 20×10^{-4} Nm/(rad/s). The pole-zero diagram for this transfer function is shown in Figure 5-9. As expected for a collocated transfer function, the system has a complex zero pair, whose undamped natural frequency lies in between those of the two complex pole pairs. The zeroes and the slower complex pole pair are

[3]This transfer function is for the motor alone. That is, we do not have the string tied to the motor shaft.

[4]Here the string is tied between the motor shaft and the spindle.

Motor Inertia J_m	1.34×10^{-5} kg m^2
Spindle Inertia J_s	5.63×10^{-3} kg m^2
Motor Viscous Damping B_m	20×10^{-4} Nm/(rad/s)
Spindle Damping B_s	3×10^{-3} Nm/(rad/s)
Motor Resistance R	13.7 Ω
Motor Spring k_{motor}	0.26 Nm/rad
String Stiffness k_{string}	2300 N/m
String Damping b_{string}	5 Ns/m
Radius of Motor Shaft R_m	0.32 cm
Radius of Spindle R_s	5 cm

Table 5.1: Parameter values that we used in our model. The stiffness and the damping of the string are estimated for the best fit of the experimental data with our model.

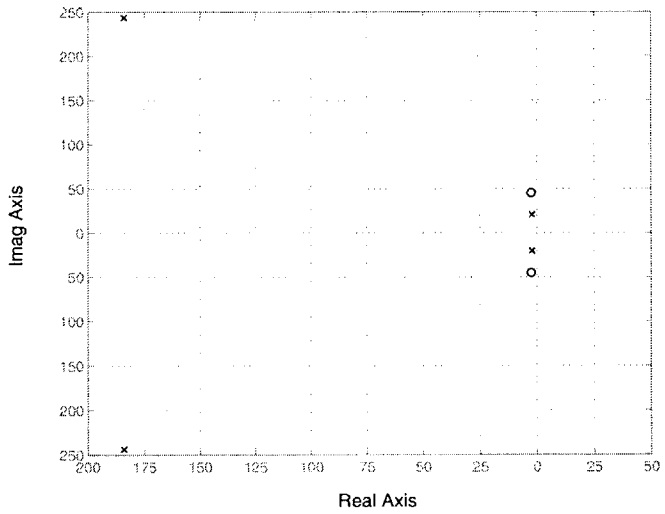

Figure 5-9: Pole-zero plot of the numerical model for the transfer function $\theta_m(s)/V_m(s)$ shown in (5.1). The zeroes are marked as blue circles 'o' and the poles are marked as red crosses 'x'.

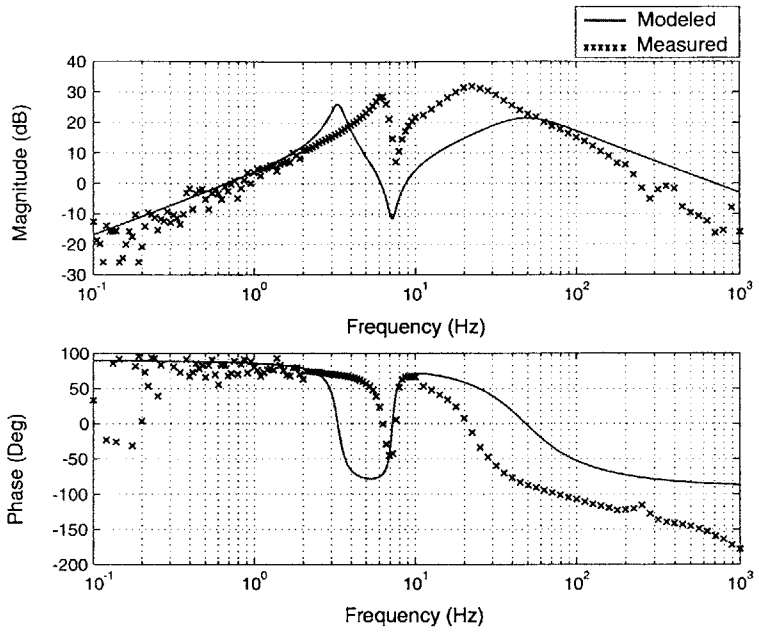

Figure 5-10: Comparison between our model and the measured frequency response of the open loop transfer function $\Omega_m(s)/V_m(s)$ of the plant.

lightly damped when compared with the faster complex pole pair.

Figure 5-10 shows the comparison between the modeled and the measured frequency response of the open loop transfer function between the motor velocity $\Omega_m(s)$ and the applied voltage $V_m(s)$. Our model conforms well to the measured location of the complex zero pair, and the slower complex pole pair (to the same order in magnitude). The root locus diagram for this transfer function is shown in Figure 5-11. With increasing gain K_v, the slower complex pole pair moves into the complex zero pair. The faster complex poles come closer to the negative real axis for intermediate gains and are hence damped out in the closed-loop system. For very large gains, these poles branch out on the negative real axis, with one pole going to the zero at -∞ and the other toward the zero at the origin.

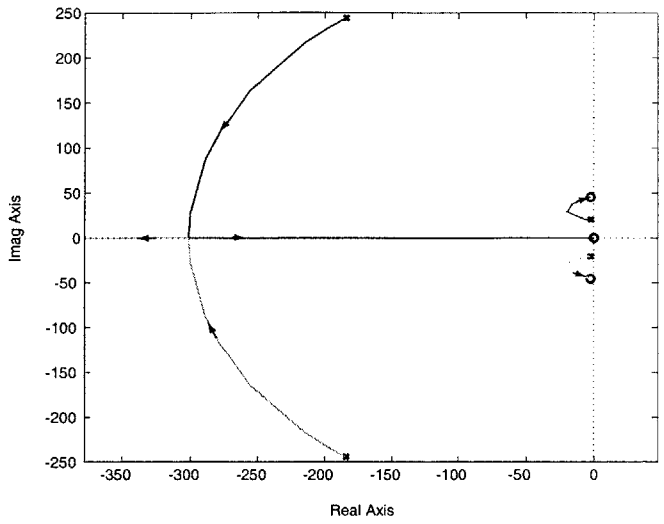

Figure 5-11: Root locus of poles and zeroes of the transfer function $\Omega_m(s)/V_m(s)$ of the plant.

5.5.3 Velocity Minor Loop

For a cross-over frequency of 150 Hz, the magnitude of the plant transfer function is measured as 10 dB, which results in a value of 0.316 for the gain K_v. The measured and predicted frequency response of the negative loop transmission for the velocity minor loop are shown in Figure 5-12. The phase margin at the cross-over frequency of 150 Hz is measured to be 61°. The cross-overs occurring at lower frequencies are all stable with sufficient phase margin.

The measured and modeled frequency response of the closed-loop transfer function of this minor loop are plotted in Figure 5-13. To further damp the modeled notch at the frequency of the complex zero pair, we increased the damping in the string in our model to a value of 10 Ns/m. As expected, because of the large magnitudes of loop transmission, the magnitude of the closed-loop transfer function just flattens out to unity for frequencies between 10 and 100 Hz. This conforms to our earlier root-locus predictions that the resonance from the faster complex pole pair will be damped out in the closed-loop system.

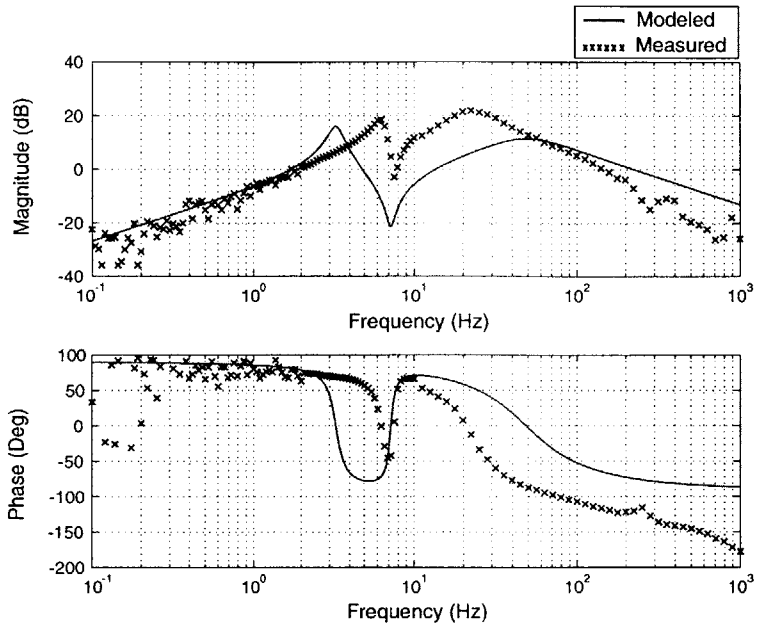

Figure 5-12: Measured and modeled frequency response of the negative loop transmission of the velocity minor loop.

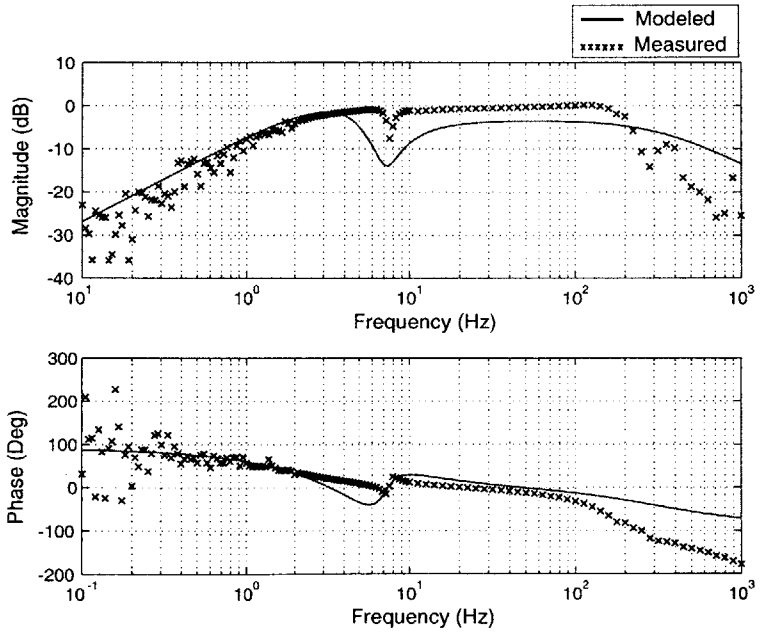

Figure 5-13: Experimental and modeled frequency response of the closed-loop transfer function $\Omega_m(s)/V_v(s)$ of the velocity minor loop.

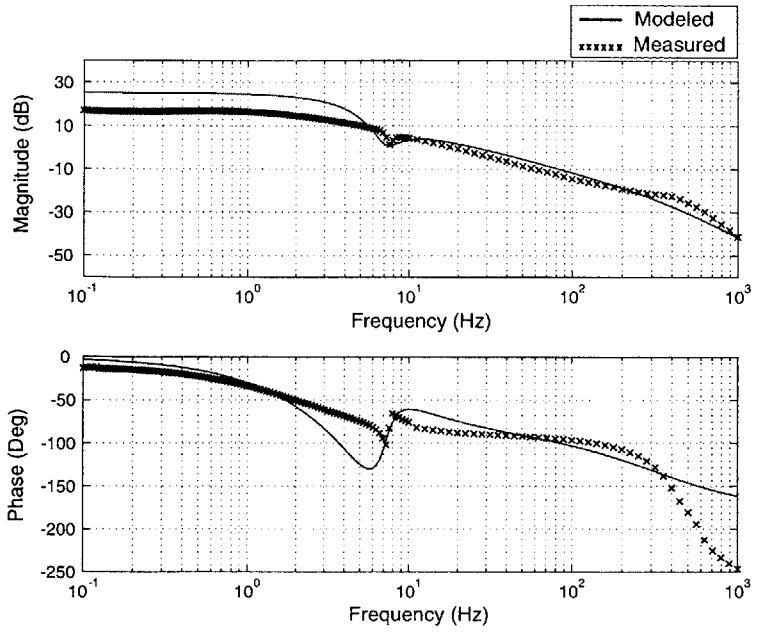

Figure 5-14: Measured and modeled frequency response of the negative loop transmission of the position minor loop. Loop transmission is designed for a cross-over of 20 Hz. The measured phase margin is 90°.

5.5.4 Position Minor Loop

The process described above for the case of the velocity minor loop is repeated here. For a cross-over frequency of 20 Hz, the value of K_p is calculated to be 120. The modeled and measured frequency response of the negative loop transmission are shown in Figure 5-14. The phase margin at the cross-over is 90°.

The measured and predicted frequency response of the closed-loop transfer function $\theta_m(s)/V_p(s)$ are shown in Figure 5-15. The closed-loop -3 dB bandwidth is about 20 Hz. At the intended cross-over frequency of 1 Hz for the major loop containing the speckle-based position feedback, this transfer function has a gain of 0.9.

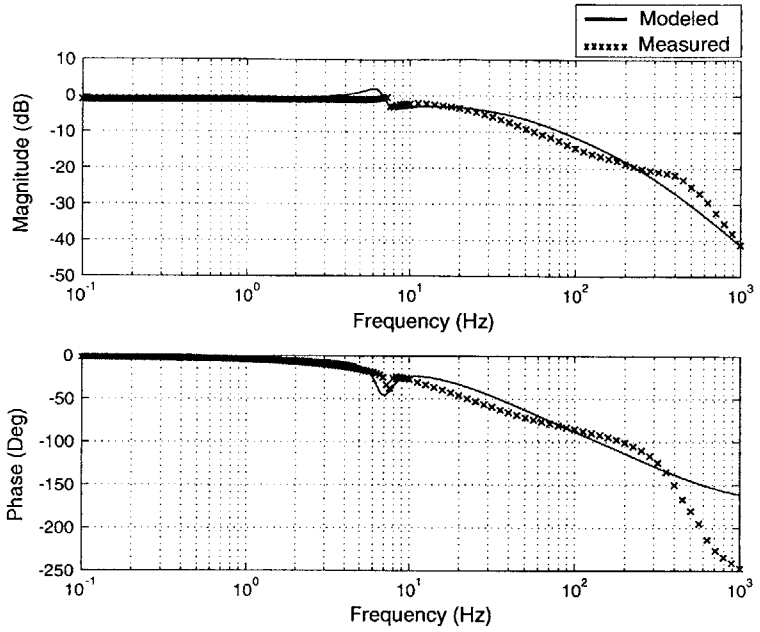

Figure 5-15: Frequency response of the measured and modeled closed-loop transfer function $\theta_m(s)/V_p(s)$ of the position minor loop.

5.6 Speckle-based Control

5.6.1 Major Loop

The control block diagram of Figure 5-4 can be simplified to the form shown in Figure 5-16. This simplified form represents the overall speckle-based control system. The control blocks in the forward path of the major loop are the integrator with gain K_I, the closed-loop transfer function of the position minor loop $\theta_m(s)/V_p(s)$

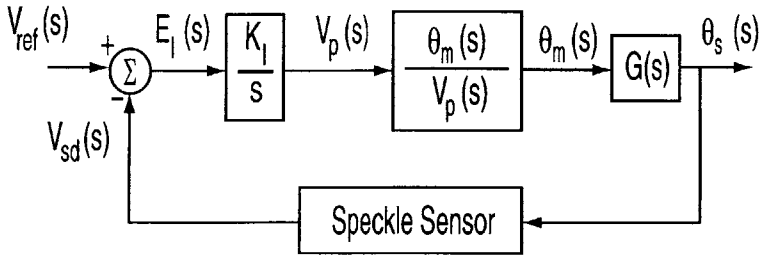

Figure 5-16: Simplified control block diagram of the speckle-based major loop.

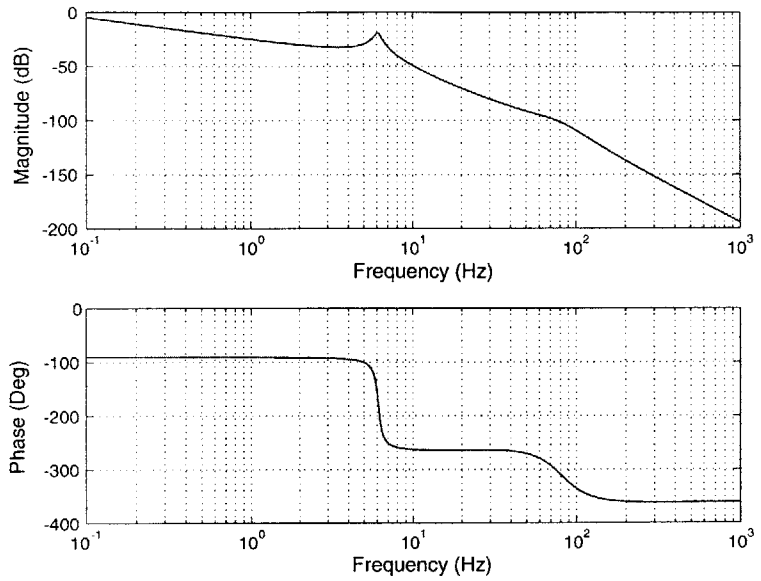

Figure 5-17: Drive resonance using our model is predicted to occur at a frequency of 6 Hz.

and the transfer function of the transmission drive $G(s) = \theta_s(s)/\theta_m(s)$. The transfer function $\theta_s(s)/E_I(s)$ is the product of these three control blocks. Figure 5-17 shows a plot of the frequency response of this transfer function based on our model for the motion system. The resonance from the compliant string in our drive in this modeled frequency response occurs at about a frequency of 6 Hz.

5.6.2 Loop Transmission

To measure the loop transmission of the speckle-based major loop, we have used the configuration shown in Figure 5-18 for our sine-sweep frequency response measurements. The execution step size of our dSPACE implementation of the position control loop is 0.1 ms, which corresponds to a sample rate of 10 kHz. In contrast, our speckle-based sensor has a low sample rate of 10 Hz. This sample rate corresponds to a computation time of 100 ms for our correlation-based image-processing algorithms. If we excite our system with signals of frequencies larger than 10 Hz, our current sensor implementation cannot cope with the rate at which the correlations need to

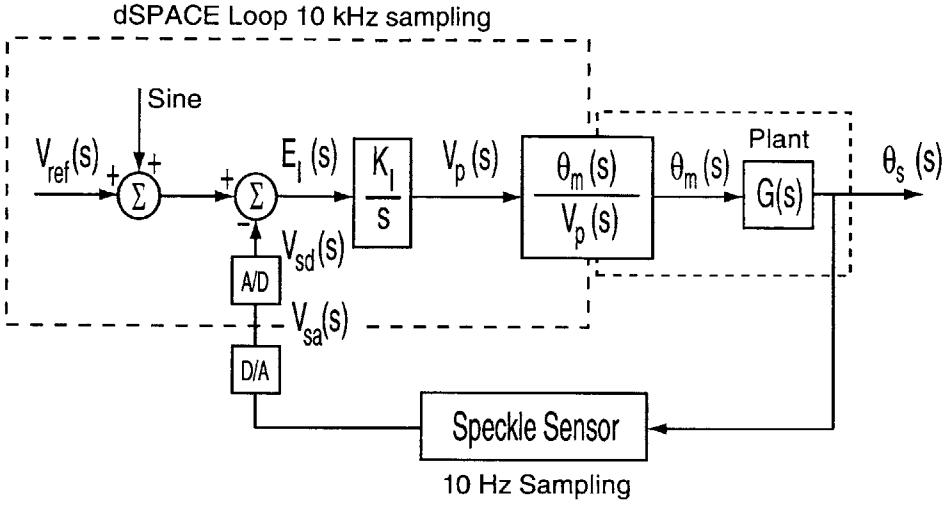

Figure 5-18: Configuration for our sine-sweep frequency response measurement of the loop transmission of the speckle-based major loop.

be performed. We have hence limited the excitation frequencies in our sine-sweep measurements to a range of 0.1-10 Hz.

As described in Section 5.3, the speckle-based position estimate is scaled to a voltage value in the NI real-time system. We have converted this voltage into an analog representation V_{sa}, and monitored this analog signal on an oscilloscope for a voltage V_p applied to the position minor loop. Here, we have mapped ± 0.8 V of the digital voltage V_p to ± 8 V of the analog voltage V_{sa}. We have interfaced this voltage V_{sa} with an A/D channel of dSPACE, which converts the analog value into a digital voltage V_{sd}. We have then successfully implemented the closed-loop system in dSPACE, as discussed in Section 5.4. Using the integrator block, we could reduce the steady state error to zero and achieve a stable control loop.

With a dSPACE ADC scale factor of 0.1, the gain between V_p and V_{sd} is 1. Hence, the loop transmission reduces to just the integrator with the gain K_I. For a cross-over frequency of 1 Hz, we have used a value of $2\pi \approx 6.3$ for K_I.

The measured frequency response of the negative loop transmission is shown in Figure 5-19. This response has a cross-over frequency of about 1 Hz, as expected for a

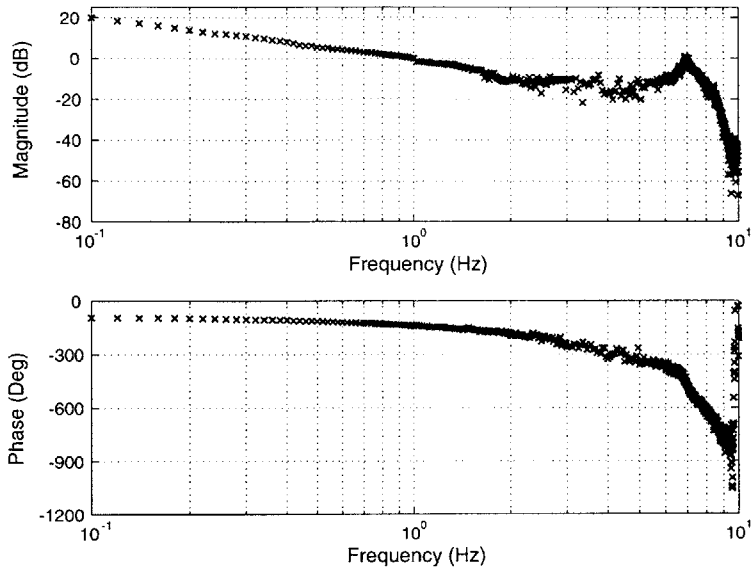

Figure 5-19: Measured negative loop transmission of the speckle-based major loop shows a cross-over frequency of 1 Hz and a phase margin of 40°.

value of 6.3 for K_I. The phase margin measured at the cross-over is 40°. A sharp peak occurs at 7 Hz in this response. In Section 5.6.1, based on a model for the transfer function of the forward path $\theta_s(s)/E_I(s)$, we have predicted that the drive resonance occurs at a frequency of 6 Hz (see Figure 5-17). The peak in our measured response seems to correspond to about the same location. We need to check for stability of the closed-loop system at this peak, since the magnitude crosses over unity here.

Before we proceed with studying this peak in more detail, we now construct a model for the loop transmission and compare its response with the measured response. It would be of interest to see if the magnitude crosses over unity at the peak in the modeled response as well.

5.6.3 Modeling

We examine the magnitude and phase contributions to the loop transmission from the individual control blocks of the speckle-based major loop shown in Figure 5-18.

The control blocks in the forward path have been described in Section 5.6.1. Here,

we propose a simple model for our speckle-based sensor placed in the feedback path. The sampling period of this sensor is $T = 0.1$ s. We assume that the discrete-time processing involved in our sensor implementation introduces a delay of a full sampling period for computing the correlation-based position estimates and a half-sample delay corresponding to a zero-order hold. For a scale factor, α, present along the feedback path, the transfer function representing our model can be written as

$$H(s) = \alpha \frac{(1 - e^{-Ts})}{s} e^{-Ts} \tag{5.3}$$

For a unity gain of the transfer function between $V_{sd}(s)$ and $V_p(s)$ at 1 Hz, the scale factor α is calculated as 173.8. Our model for the loop transmission of the speckle-based major loop is given as

$$L(s) = -\frac{K_I}{s} \frac{\theta_m(s)}{V_p(s)} G(s) H(s) \tag{5.4}$$

5.6.4 Peak measured at 7 Hz

Based on the model presented in Eq. 5.4, we have computed the frequency response of the negative loop transmission of our speckle-based major loop over the frequency range 0.1-10 Hz. This response is represented by the solid curve in Figure 5-20. The measured frequency response of the negative loop transmission, marked as 'x', is shown as a reference for comparison. The cross-over frequency calculated from our model matches with the measured value of about 1 Hz. The modeled phase margin is 35.4°. The resonance peak occurring at about 6 Hz in our model is smaller in magnitude than the peak in the measured response. Magnitude does not cross over unity in the modeled response.

Here, we present our interpretation of the peak measured at 7 Hz in the frequency response of the loop transmission. First, we examine the aspect of aliasing. Since

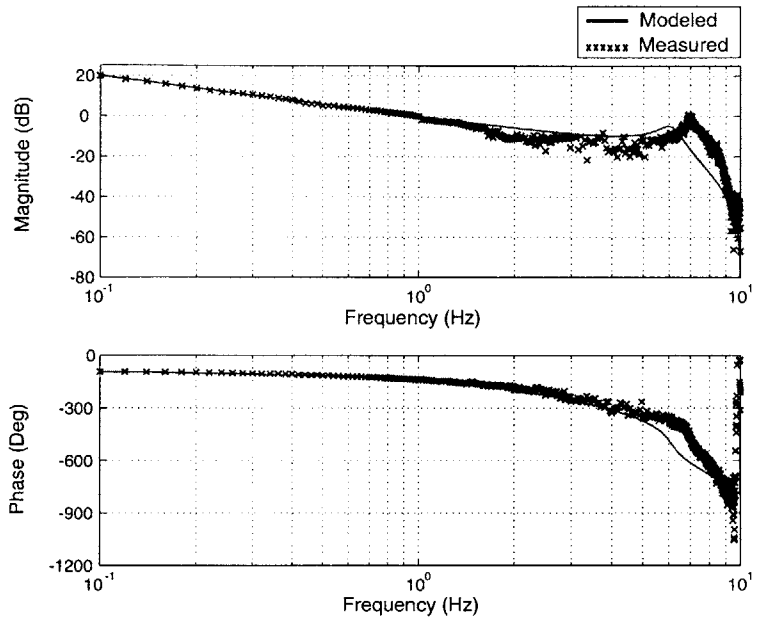

Figure 5-20: Modeled and measured frequency response of the negative loop transmission of the speckle-based major loop in our control system.

the sample rate of our speckle-based sensor is 10 Hz, the Nyquist rate is 5 Hz. For sampling signals of frequencies in the range 5-10 Hz, our sample rate is not sufficiently fast and this results in aliasing of these signals to frequencies in the range 0-5 Hz. A signal with a frequency ω_o in the range 5-10 Hz, when sampled by our speckle-based sensor, gets aliased to a frequency ω given by $\omega = 10 - \omega_0$. As an example, a signal of frequency 6 Hz measured by this sensor is aliased as a signal of frequency 4 Hz.

We recognize that there are two sampling rates for our control system, one at 10 kHz for our dSPACE position control loop and the other at 10 Hz for our speckle-based sensor. Since the 10 kHz sample rate is sufficiently fast, the signals measured by dSPACE are not aliased in the sampling process. This means that we can apply high frequency signals in exciting our system from dSPACE, without generating any aliases for these signals.

So, when we excite our system from dSPACE with a sine signal of frequency 7 Hz, it is fed to the speckle-based sensor as a signal at the same frequency. Since this

frequency is higher than the Nyquist rate of 5 Hz, it is aliased as a 3 Hz signal by the speckle-based sensor.

Note that we have measured the frequency response of the loop transmission after closing the speckle-based major loop, as shown in the configuration of Figure 5-18. So, the 3 Hz alias generated by our speckle-based sensor gets fed back to the control loop (see Figure 5-18) and can excite the system at this frequency. The signals in the closed-loop system are then a mixture of the aliased and actual components of the exciting signal.

The dSPACE/Simulink-based Dynamic Signal Analyzer (DSA) [31] that we use to record our sine-sweep measurements performs an FFT-based correlation of data sets collected for each of the input and output signals after excitation with sine signals in the specified frequency range. We suspect that the large magnitude measured for the peak at 7 Hz could be arising from imperfections of our DSA in handling the 3 Hz aliased signal. The length of the data sets, the settling time between successive excitations, and the integration time over which the measurements are averaged, are some of the factors that are preset in our DSA. We have not attempted verifying this yet, but we suspect that the choice of these factors could have a bearing on the imperfections in our DSA.

Finally, we use the Nyquist criterion to address stability of the closed-loop system at this resonance. The phase at the cross-over here is - 482.75° $\simeq$ - 122.75°. Since the gain drops off at high rates before and after the peak (see Figure 5-20), there are no encirclements of the -1 point on the negative real axis of the loop transmission L(s) plane. Since there are no poles for the loop transmission in the right half plane, and there are no encirclements of the -1 point, the closed loop system is stable.

In summary, we tend to believe that there is a contribution to the measured peak from an aliased signal in addition to that from the actual exciting signal. An efficient DSA tool can minimize the contribution measured from the aliased signal

and can hence measure the dynamic response accurately. Our model for the loop transmission matches closely with the measured response up to the Nyquist limit of 5 Hz. Our model, however, cannot account for the aliasing observed with our sensor implementation. Since we are representing the system response to a 7 Hz excitation signal at a sampling rate of 10 Hz, our model seems to be unable to simulate the large magnitude of the 7 Hz peak measured with our speckle-based sensor. Even if we assume that we have a perfect DSA tool and the measured peak is an actual peak, we have seen from the Nyquist criterion that the unity cross-over here does not cause an instability in the closed-loop system.

We have performed the sine-sweep frequency response measurements on our system primarily to test the control performance of our speckle-based sensor. At the intended cross-over of 1 Hz, we have achieved a sufficient phase margin of 40°. This proves the promise of our speckle-based sensor in feedback control applications. For completeness, we have presented our observations on the peak measured at the drive resonance and our understanding of it. The aspects of aliasing are a direct outcome of the low update rates in our current implementation. A stiffer transmission drive, or a direct-drive setup, could avoid huge peaks caused due to aliasing of the drive resonance by our speckle-based sensor. We suggest the use of these drives in future implementations.

5.6.5 Closed-loop System

The closed-loop system transfer function is given as $-L(s)/(1 - L(s))$, where $L(s)$ is the loop transmission. The frequency response of the closed-loop system transfer function is computed based on the model for $L(s)$ given in Eq. 5.4 and plotted as the solid curve in Figure 5-21. The frequency response obtained from our sine-sweep measurements is marked as 'x'. The closed-loop system -3 dB bandwidth is about 2 Hz. This low bandwidth can be reasoned from the fact that our speckle-based

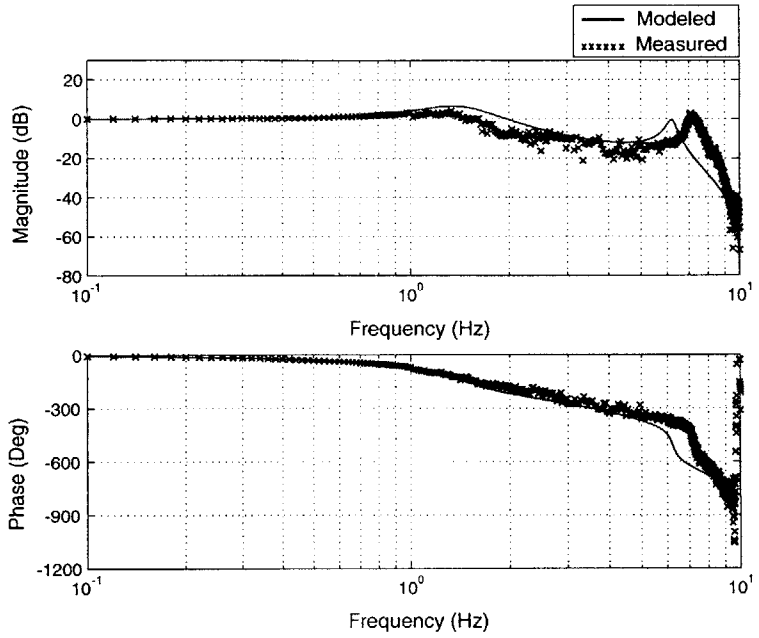

Figure 5-21: Frequency response of the closed-loop transfer function between speckle-based voltage $V_{sd}(s)$ and reference voltage $V_{ref}(s)$ of the speckle-based major loop in our control system.

sensor has a low sample rate of 10 Hz. We propose in Section 6.2 methods by which this limitation of our current implementation can be overcome.

Steady State Oscillation

Figure 5-23 shows a steady state oscillation of frequency 2 Hz recorded for the speckle-based voltage V_{sd} when no reference voltage is applied to the closed-loop system. This data is recorded with our system for a string of length L = 11.6 inch. The amplitude of the oscillation is 1 V. This oscillation could be because of a limit-cycle arising from our implementation of the pattern-matching algorithms that generate the speckle-based position estimates in our NI real-time system. Since we have not verified this point yet, the source of this oscillation remains to be identified. For a scale factor of $8\text{V}/30\,\mu\text{m}$, an amplitude of 1V of this oscillation corresponds to about $3.75\,\mu\text{m}$ in position. This oscillation limits the resolutions achievable with our current implementation. A low pass filter with a cut-off frequency of, say, 0.2 Hz may be used

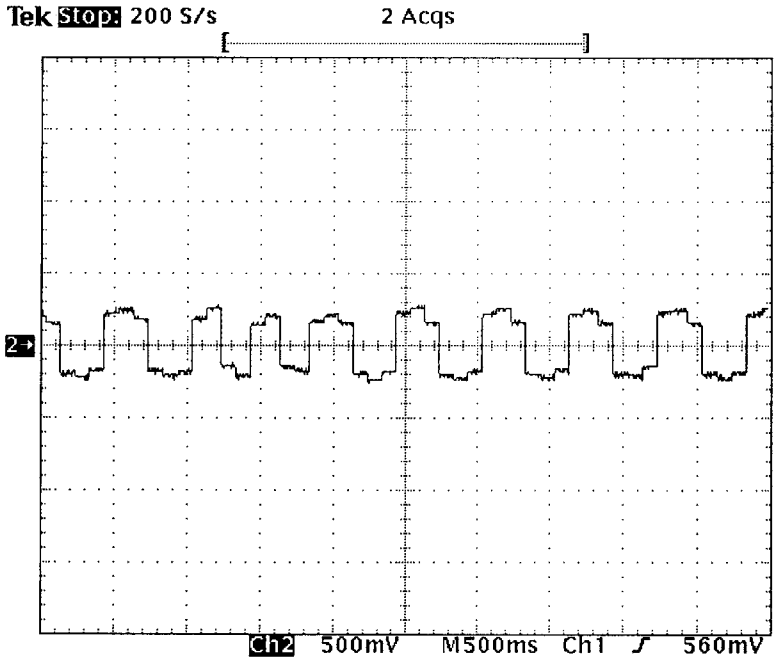

Figure 5-22: At zero values of the reference voltage V_{ref} in the closed-loop system, the speckle-based sensor output has a steady oscillation at a frequency of 2 Hz.

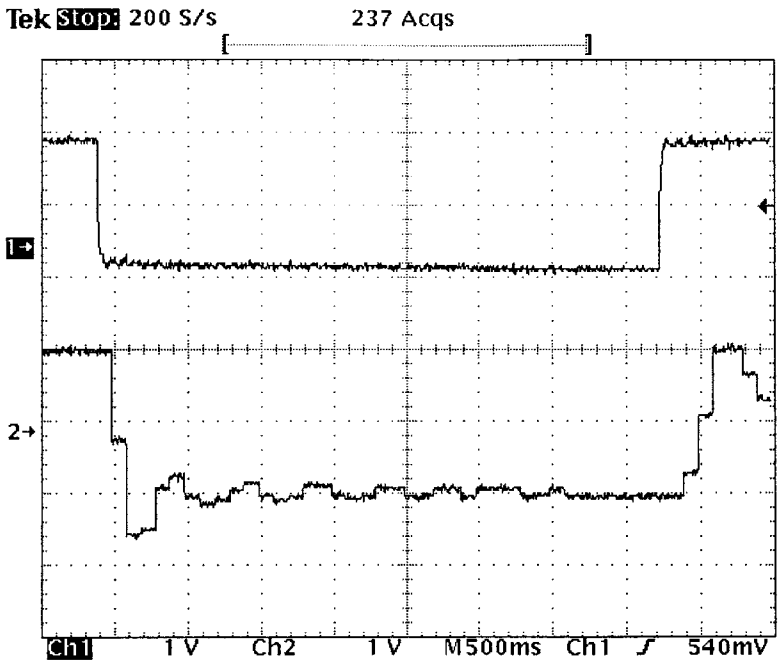

Figure 5-23: Channel 2 output shows the scope trace of the step response of the closed-loop system measured using the speckle-based sensor. The trace shows a superimposed steady oscillation of frequency 2 Hz. Channel 1 is the step response of motor position measured by the optical encoder provided with the motor.

to filter this 2 Hz oscillation.

Step Response

The scope trace of Channel 2 in Figure 5-23 shows the step response of the closed-loop system as measured using our speckle-based sensor. This response is recorded for a string of length $L = 11.6$ inch and an integrator gain of 0.1. The trace of Channel 1 represents the motor angle θ_m, measured using the optical encoder provided with the motor. A steady oscillation of frequency 2 Hz is superimposed on the response measured by the speckle-based sensor. The drive resonance measured for this setting is at 8 Hz. For a sample rate of 10 Hz, a signal of frequency 8 Hz measured by our speckle-based sensor is aliased to a frequency of 2 Hz. This could be a reason for the presence of the 2 Hz steady state oscillation in our step response measurement.

Chapter 6

Conclusions and Suggestions for Future Work

6.1 Summary

This work explored a novel speckle-based position sensing technique applicable to precision motion control systems. We have concentrated on testing the achievable resolution and control performance of our laser speckle-based machine vision sensor. The summary of our work is presented below:

Problem Statement

Our goal was to build a rotary sensor with high resolution and repeatability for use as a position sensor in machine tool metrology applications. The context of this sensor is compound rotary-linear motion metrology of a hybrid rotary-linear axis described in Section 1.3.

Approach

We have discussed in Section 1.3.2 some currently available sensors that apply to compound rotary-linear motion metrology. Heidenhain and Renishaw have come up with commercial two-dimensional planar encoder grid scale sensors. We have not

come across any commercial versions of cylindrical counterparts of these sensors. A rotary-linear actuator system patented by Chitayat [18] uses a sensor that measures the motion of an optical pattern printed on a cylindrical surface. We combined the ideas from these sensors to implement a machine vision sensor that gauges motion visually.

Our Solution

Instead of printing an optical pattern on the spindle surface, we used the laser speckle technique to generate highly position-correlated patterns from the surface. We calibrated our sensor against an auxiliary sensor system described in Chapter 3. We stored two global images separated by a distance of $60\,\mu$m as measured by this auxiliary sensor system. We interpolated between position estimates obtained by performing real-time correlation-based pattern matching between the current speckle image and each of the two global images.

First, we tested our sensor using a micrometer setup to turn the spindle. An image offset by a pixel corresponds to a surface motion of $3.6\,\mu$m. Sub-pixel resolution and repeatability could be easily achieved. We then used the sensor on a rotary stage built from an air-bearing spindle. The closed loop system is stable, the phase margin at crossover being 40°. The control bandwidth is low at about 2 Hz owing to the low update rate of 10 Hz. The system dynamics was modelled and analyzed in Chapter 5.

Challenges

The present low update rate is because of the time-intensive nature of correlation based algorithms that we have used in measuring displacement across images. Real-time acquisition and analysis of image data at higher sample rates is challenging in terms of computational power of the processor.

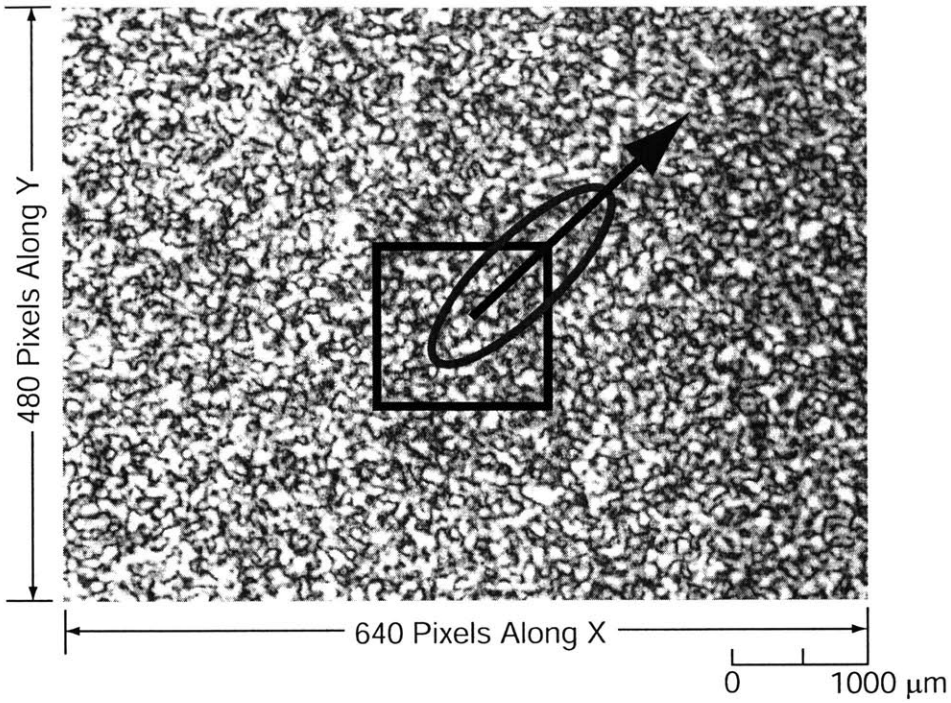

Figure 6-1: Schematic showing localized pattern search that may be implemented on our current system.

6.2 Suggestions for Future Work

• Increase the sensor sample rate.

A possible solution to achieve faster update rates is localizing search with our current image processing technique. For a given pair of pre-stored global images, the direction of speckle shift is known. Consider the typical speckle image shown in Figure 6-1 with a speckle shift in the direction of the arrow. Instead of searching for a central pattern in the whole pixel plane, we can limit our search to just the vicinity of motion along this direction, say, to an elliptical region as shown in figure. The size of the ellipse must be based on position values generated by a estimator that predicts future positions based on current and past positions.

One possible offshoot of this research work is developing an efficient search algorithm that can be used to measure displacement across speckle images. Vona [16]

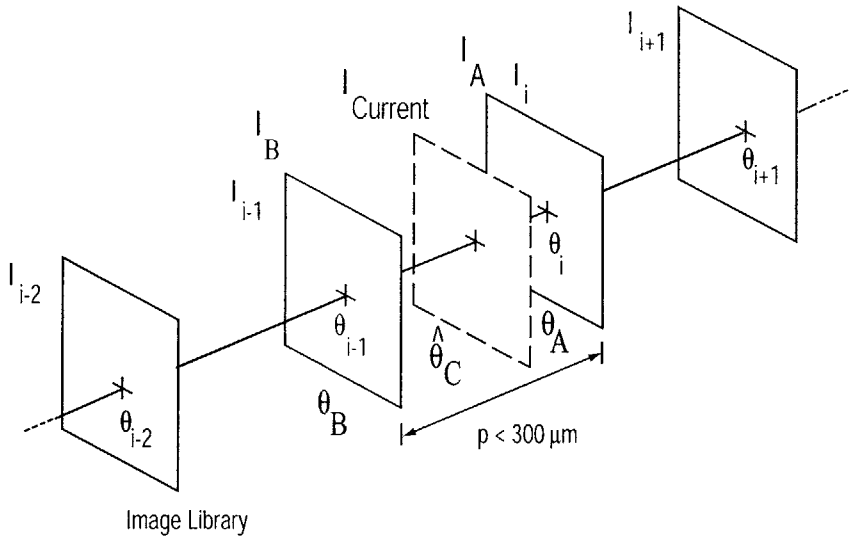

Figure 6-2: Schematic showing a global library of images recorded over the range of motion of the spindle.

discusses the use of absolute difference methods and FFT-based methods apart from correlation-based methods. These could be good starting points for any efforts in this direction. Ultimately, localized search with an optimal search algorithm would be an efficient approach to our motion tracking problem.

- Implement a global image library over the range of motion.

The range of motion in our implementation is limited to 60 μm since we are using just two images separated by that distance. As described in Section 2.2.2, we can extend the range of motion to essentially any desired distance by recording global images I_i spread uniformly over this distance as depicted schematically in Figure 6-2. The pitch spacing p of the images is decided by the decorrelation limit and the memory space available for storage of the library. The upper limit on p is the decorrelation limit ($\approx$ 300 μm in our case). Each 640 $\times$ 480 pixel speckle image captured by our imaging system is about 300 kB in size. As an example, for a pitch spacing of 100 μm, and a range of motion of 1.5 cm, about 45 MB of memory space would be required. As discussed in Section 2.2.2, the state space model of Figure 2-5 could be implemented

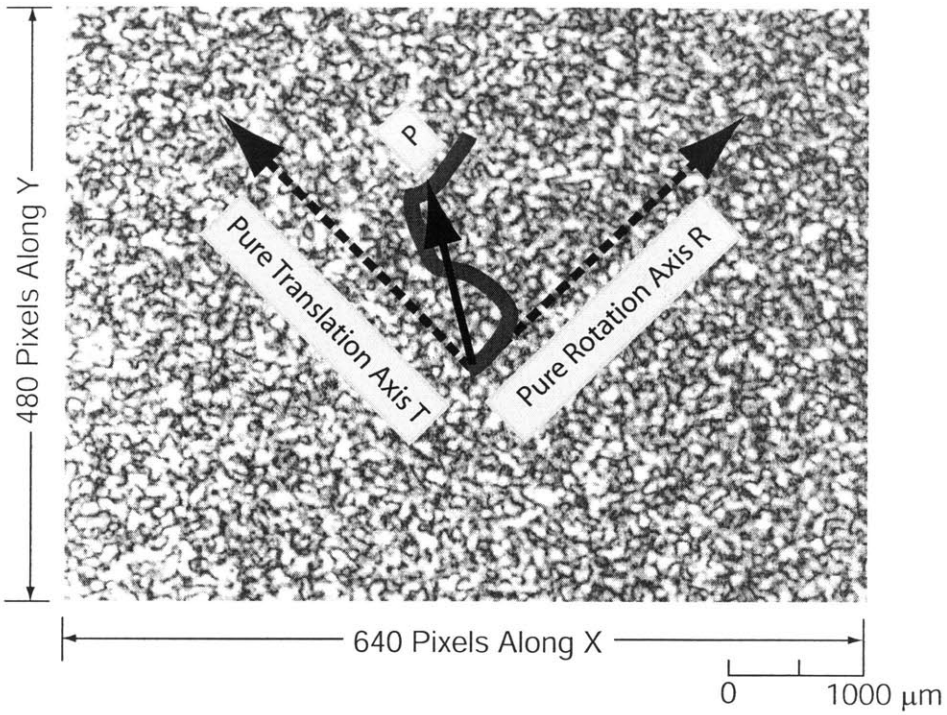

Figure 6-3: Schematic showing the use of our speckle based sensor for compound rotary-linear motion. This is based on a machine vision topology presented by Vona [16]. The speckle shift can be resolved along the axes R and T to obtain rotational and translational displacements respectively. A representative speckle image is shown in the background.

to recover position from the global library.

- Implement a sensor for compound rotary-linear motion metrology.

Here we present some ideas on extending our sensing principle to compound rotary-linear motion, that is, for simultaneously sensing motion along two axes. We have not implemented these ideas, so they remain unverified at this point. A basic topology describing a machine vision sensor for compound rotary-linear motion metrology is presented by Vona [16]. Figure 6-3 shows a schematic applying this topology to our speckle sensor. For the case of pure rotation, like that we have in our current setup, let the speckle shift be along the axis R. If now we arrest the rotation of the axis, and allow it to translate, the speckle shift must be in a perpendicular direction, say, along the axis T. For a combination of rotation and translation, the speckle shift

can assume an arbitrary locus, such as the solid curve in the figure. At any point P on this locus, the corresponding net rotation and translation can be obtained by resolving the position vector (shown by a solid arrow) along the two axes.

We need to extend the principle of the global library to this case of compound rotary-linear motion. For pure rotation, we discussed earlier that the global library must be a linear grid of images spaced along the axis R. Similarly, for pure translation, the global library lies along the axis T. For compound rotary-linear motion, the library must be a grid in the RT space. For localized search in the RT space, we may have to choose a circular search region around the current position.

Note here, though, that the memory requirements scale as the second power of the spatial resolution. For example, if we require a library of 1000 by 1000 images, this represents 10^6 images, and thus requires a library of about 3×10^{11} bytes. This is certainly a daunting prospect in terms of practical application.

In theory, we should be able to measure rotation and translation simultaneously with this sensor. These measurements are independent of each other. If we are interested only in rotation, the advantage of this sensor over the Renishaw encoder is that this sensor is unaffected by translation of a rotating shaft.

We can use our current imaging system without any changes, and set it up for an axis that both translates and rotates to test the ideas presented above. The hybrid rotary-linear axis test bed [7, 16] can be used for this purpose.

6.3 Thesis Contributions

The main contribution of our work is the development of a non-contact position sensor with high resolution and repeatability for use in machine tool applications. The principle of this sensor can be extended to compound rotary-linear motion.

Specific thesis contributions are listed below:

• Developed a laser speckle-based machine vision sensor for measuring the angular displacement of an air-bearing spindle. Achieved higher resolution than a Renishaw incremental optical encoder.

• Developed as a reference sensor for the metrology system a bicell photointerrupter unit that has a repeatability of better than 1 μm, as measured using a micrometer setup.

• Developed an interpolation algorithm for obtaining a position estimate from image offsets measured with respect to two reference images.

• Implemented closed-loop control of position of the air-bearing spindle using speckle-based position feedback. Modeled and analyzed the closed loop system behavior in the frequency domain.

6.4 Concluding Remarks

This work proved experimentally the idea of using speckle images for estimating position at a high resolution. We could easily implement a static response system with a micrometer and PC-based MATLAB routines that calculated displacements across the images. The hardware setup for image acquisition and analysis in this case was simple.

However, coming up with a solution for real-time measurements was more challenging. Since Windows operating system is not real-time, we had to opt for a separate real-time processor integrated with the image acquisition hardware. We set up a simple motion system on which we tested the sensor for its control performance.

We could not achieve high control bandwidths, due to low update rates arising from the image processing routines we use. Localized pattern search should be attempted in any future projects addressing this issue.

Still, the promise of resolution and repeatability that we have observed with our

sensor is encouraging. If update rates can be improved to larger values, the speckle-based sensor could potentially be incorporated as a rotary-linear sensor in the motion industry.

Appendix A

Software Implementation

The schematic for the operation of our speckle-based metrology system is described in Section 5.4. Here we present the sequence of steps followed in our software implementation.

1) Perform an RTW Build of the Simulink model speckle.mdl shown in Figure A-1.

2) Vary the parameter "Pre-index Position Command" in the ControlDesk layout speckle.lay shown in Figure A-2. This parameter runs the Subsystem A. Once the bicell zero crossing is hit, the LED indicator "Index Switch" is turned on. The Renishaw RGR encoder reading is set to zero at this point in the Auxiliary Sensor Subsystem. Turn on SwitchS3 and SwitchS4. This will lock the Subsystem A and activate Subsystem B.

3) Vary the reference voltage V_{ref} between the limits of +0.8 V and -0.8 V. At each limit, capture the speckle image using the NI image acquisition software. The user panel for this software is shown in Figure A-3. Transfer the image files to the root directory of the NI real-time operating system.

4) Set V_{ref} to each of the limits (+0.8 V and -0.8 V) in speckle.lay and run speckle.vi to register the speckle images. The LabVIEW wiring schematic of speckle.vi is shown in Figure A-4.

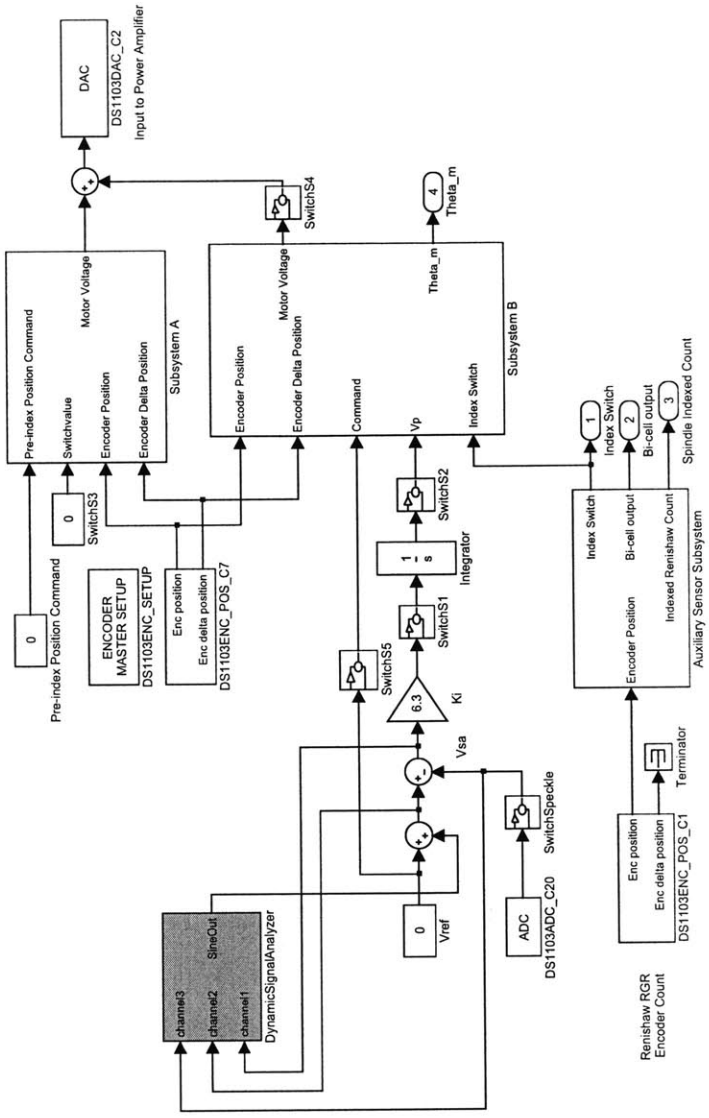

Figure A-1: Simulink Model of speckle-based sensor system includes 4 subsystems as shown. Subsystems A and B run the motor before and after, respectively, of detection of the zero-crossing. Auxiliary Sensor Subsystem interfaces with the photo-interrupter unit and triggers the Renishaw encoder count once the bicell hits the zero-crossing. Dynamic response of the system can be measured by connecting the channels of Dynamic Signal Analyzer subsystem [31] across different points in this model. The motor optical encoder and the Renishaw encoder are interfaced with the channels DS1103ENC_POS_C7 and DS1103_ENC_POS_C1 respectively. The speckle feedback is available from the dSPACE ADC channel DS1103ADC_C20. For convenience, an additional switch SwitchS5 is added in a feed forward branch driving the motor. Before the bicell is zeroed, this switch is kept closed so that the reference voltage V_{ref} drives the motor. When speckle based position is fed back, this switch is opened. Output from DS1103_DAC_C2 drives the PA-21 Power Amplifier. Katherine Lilienkamp helped me with the Simulink and DSA aspects of this implementation.

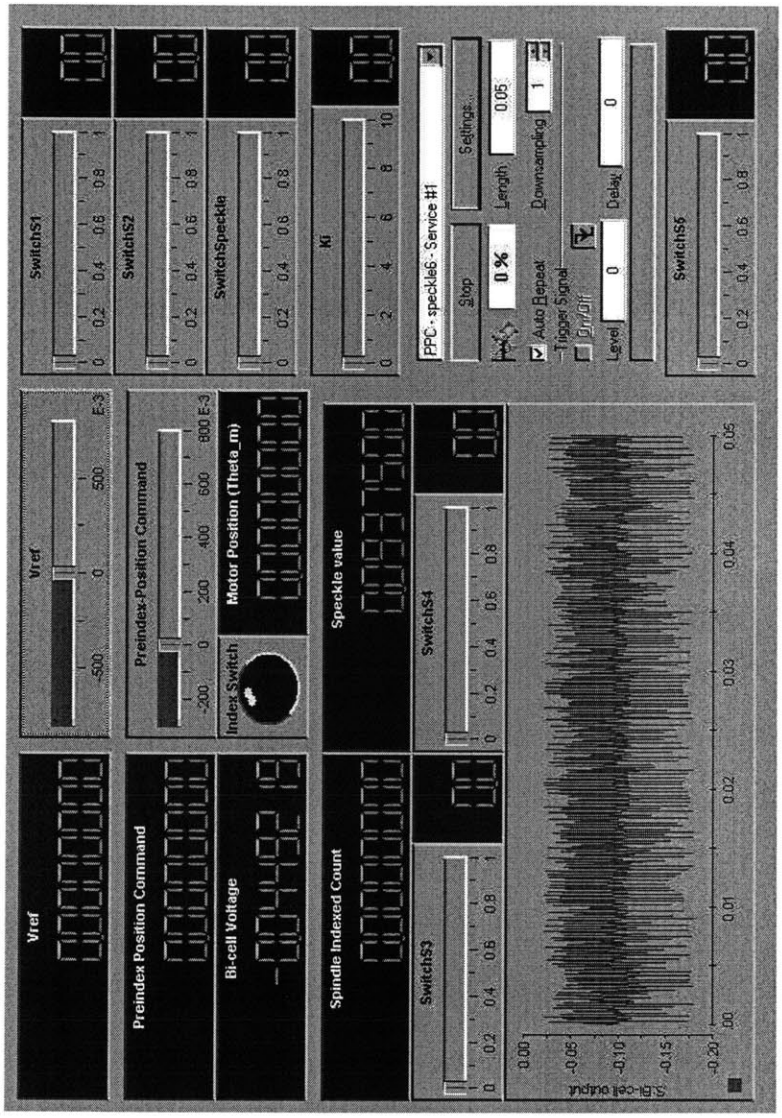

Figure A-2: ControlDesk layout of our implementation of the speckle-based metrology system. Once the speckle.mdl is built, model parameters are transferred from the trace file speckle.trc. In real-time, these parameters can be varied and the data signals of our system can be captured from this layout.

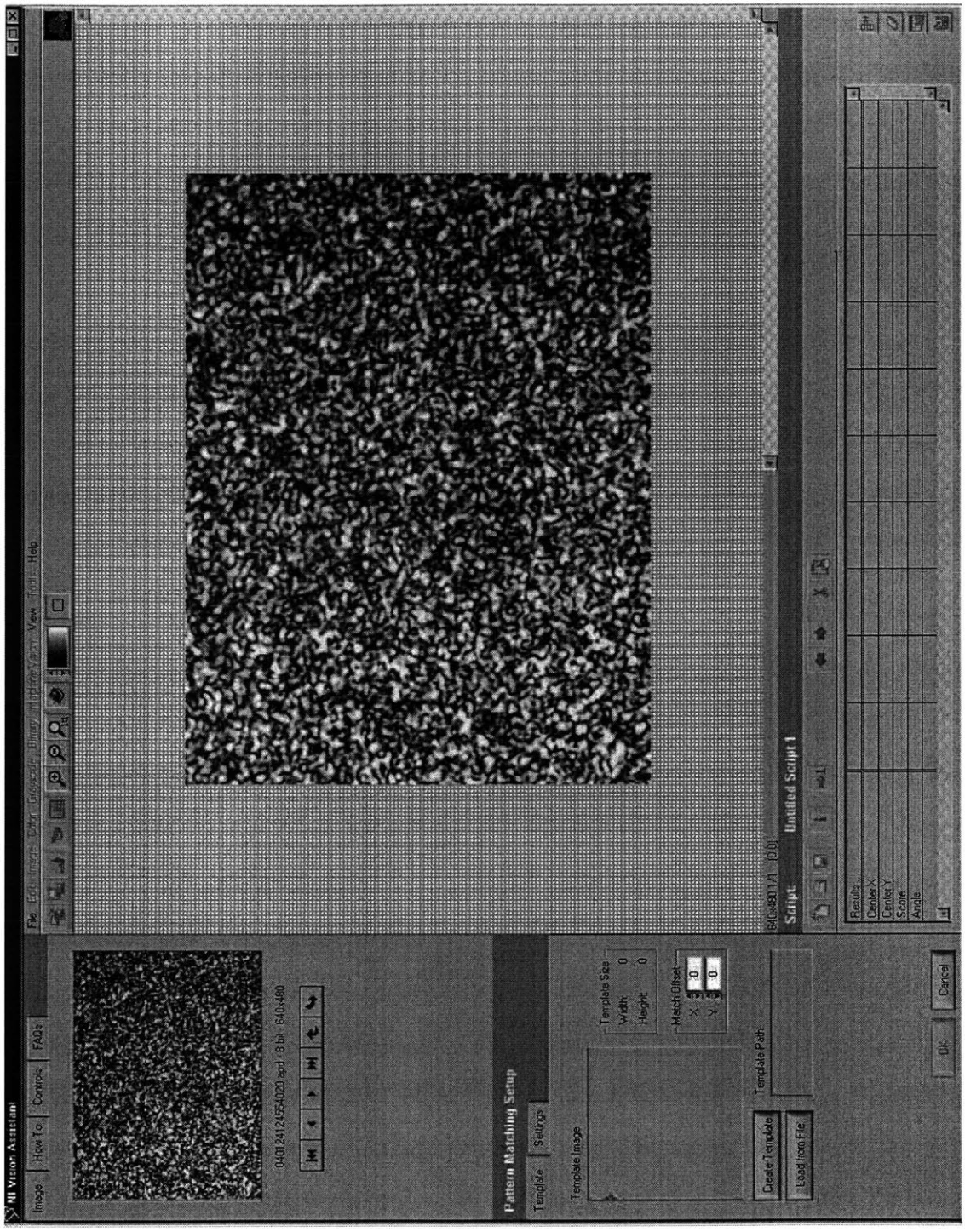

Figure A-3: User Panel for the NI Vision Assistant 7.0 image acquisition software. From this panel, speckle images can be captured on the host PC. Through an ftp process, the speckle images are transferred to the root folder of the real-time operating system. The file path names are given as inputs to the speckle-based sensing algorithm implemented in LabVIEW.

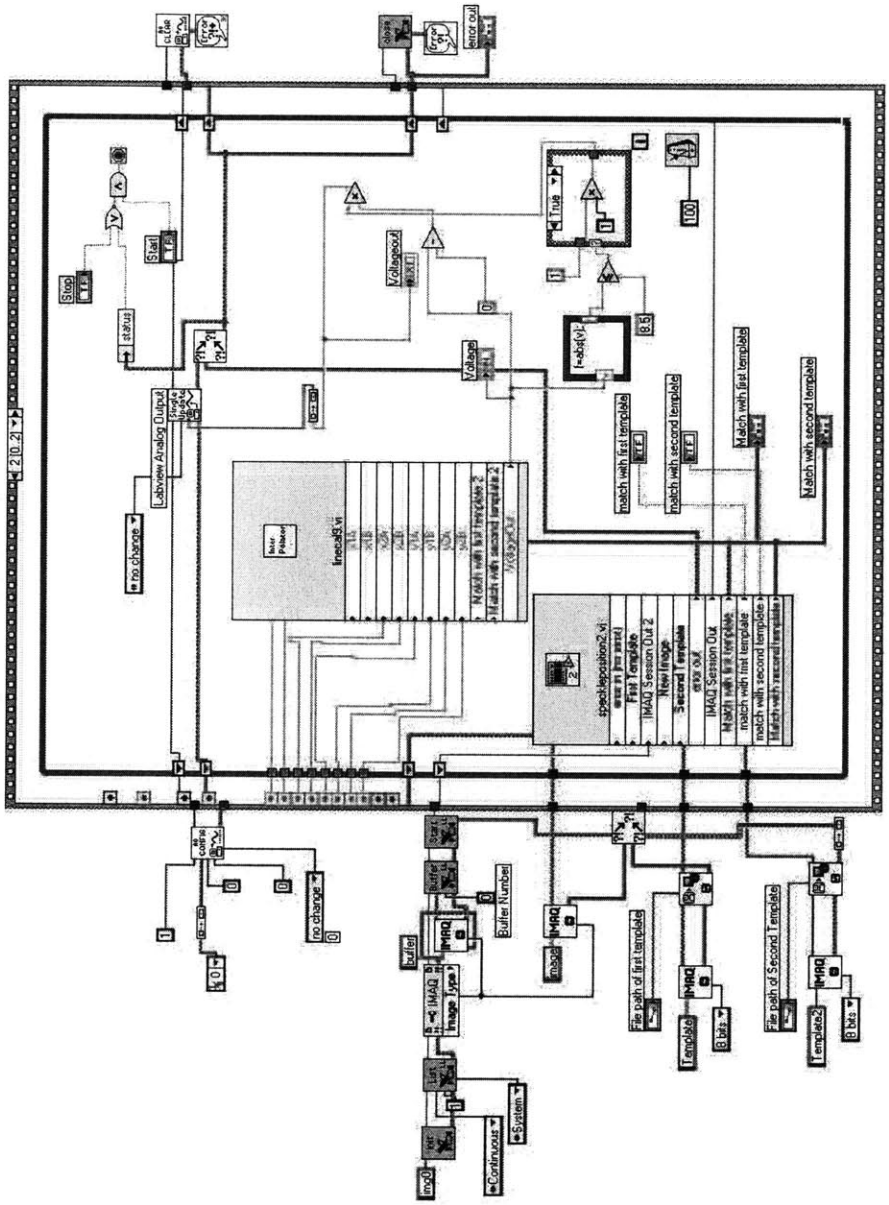

Figure A-4: LabVIEW wiring schematic of speckle.vi, which generates a digital voltage representing the speckle-based position estimate. The SubVI Interpolator interpolates between position estimates derived from pattern matching results obtained by the SubVI speckleposition2.vi. This implementation of our speckle-based sensing algorithm has been assembled from low level programming VI's available in the example library of LabVIEW. Justin Chickles and the Technical Support of National Instruments assisted in writing this code.

5) In speckle.lay close SwitchS1, SwitchS2 and SwitchSpeckle, and open SwitchS5.

Appendix B

Vendors

dSPACE Inc.
28700 Cabot Drive – Suite 1100
Novi, MI 48377
Telephone — (248) 567-1300
Web address — http://www.dspaceinc.com/index.htm
Product used: DS1103 Controller Board

The MathWorks, Inc.
3 Apple Hill Dr.
Natick, MA 01760-2098
Telephone — (508) 647-7000
Web address — http://www.mathworks.com
Products used: MATLAB, Simulink

Advanced Photonix, Inc.
1240 Avenida Acaso
Camarillo, CA 93012
Telephone — (805) 987-0146
Web address — http://www.advancedphotonix.com
Product used: Bi-cell SD-066-24-21-011

Renishaw Inc.
5277 Trillium Blvd
Hoffman Estates IL 60192
Telephone — (847) 286-9953
Web address — http://www.renishaw.com
Product used: Renishaw RGR Encoder

Anorad Inc.
100 Precision Drive Shirley
New York 11967-4710
Telephone — (631) 344-6600
Web address — http://www.anorad.com
Product used: Anorad RGBD x01 Interfacing Unit

Professional Instruments Company
7800 Powell Road
Hopkins, MN 55343
Telephone — (952) 933-1222
Web address — http://www.airbearings.com
Product used: Air-bearing Blockhead Spindle Model 4B

National Instruments Corporation
11500 N Mopac Expressway
Austin, TX 78759-3504
Telephone — (512) 683-0100
Web address —http://www.ni.com
Products used:
Hardware: PXI Chassis 1042, PXI Embedded Controller 8171, Multi-function DAQ 6052E, IMAQ 1409 Video Capture Card
Software: LabVIEW 7.0, LabVIEW Real-time 7.0, Vision Assistant 7.0

Edmund Industrial Optics
W028 101 East Gloucester Pike
Barrington, NJ 08007-1380
Telephone — (800) 363-1992
Web address — http://www.edmundoptics.com
Product used: Analog Monochrome WAT 902C, VZM 100 Microscope

Coreco Imaging Company
900 Middlesex Turnpike
Building 8, Floor 2, Billerica, MA 01821
Telephone — (978) 670-2000
Web address — http://www.coreco.com
Product used: Bandit Video Capture Card

Servo Systems Company
115 Main Road, P.O. Box 97
Montville, NJ 07045-0097
Telephone — (800) 922-1103
Web address — http://www.servosystems.com
Product used: DM-526 Limited Angle Brushless Torque Motor with Optical Encoder

Red Line, Inc.
St.Louis, Missouri, 63031 USA Telephone — (314) 831-3014
Web address — http://www.superbrightleds.com
Product used: RL5-R8030 Super Bright LED

Bibliography

[1] Michael K. Liebman, Marsette A. Vona, David L. Trumper. A Rotary-linear Hybrid Machine Tool Axis. In Proceedings of ASPE Conference, vol. 26, pp. 131-134, 2001.

[2] Douglass Blanding. Exact constraint Machine Design Using Kinematic Principles. ASME Press, New York 1999.

[3] Polytec Physike Instrumente. 16 Albert St. Auburn, MA 01501 Ph. (508) 832-3456 http://www.pi.ws/

[4] Aerotech, Inc., 101 Zeta Drive Pittsburgh, PA 15238-2897 Ph. (412) 963-7470 http://www.aerotech.com/

[5] Maxon Precision Motors, Inc. 838 Mitten Road Burlingame, CA 94010. Ph. (800) 865-7540 http://www.maxon.com/

[6] Vijay Shilpiekandula, Michael K. Liebman, Marsette A. Vona, David L. Trumper. Rotary-linear Hybrid Axis for Meso-scale Machining. In Proceedings of NSF Design, Manufacturing and Industrial Innovation Research Conference, 2003.

[7] Michael K. Liebman. Rotary-Linear Axes for High Speed Machining. Ph.D. Thesis, Department of Mechanical Engineering, Massachusetts Institute of Technology, Cambridge, MA, 2001.

[8] Beckmann P, Spizzichino A. The Scattering of Electromagnetic Waves from Rough Surfaces. Pergamon/Macmillan, New York 1963.

[9] Joseph W.Goodman Statistical Optics. Wiley, New York 2000.

[10] Christopher J. Dainty ed. Laser Speckle and Related Phenomena. Springer - Verlag, Berlin 1974.

[11] Francon M. Laser Speckle and Applications in Optics. New York, Academic Press 1979.

[12] Rajpal A. Sirohi ed. Selected Papers on Speckle Metrology. SPIE, vol. MS 35, 1991.

[13] Lyle G. Shirley. Methods and Apparatus for Remotely Sensing the Orientation of an Object, 1998. U.S. Patent No. 5811826.

[14] Gary L. Cloud. Optical Methods of Engineering Analysis. Cambridge Press, 1995.

[15] Yamaguchi I. Speckle displacement and decorrelation in the diffraction and image fields for small object deformation. Optica Acta, vol. 28 (10), pp 1359-1376, 1981.

[16] Marsette A. Vona. Metrology Techniques for Compound Rotary-Linear Motion. S.M. Thesis, Department of Electrical Engineering and Computer Science, Massachusetts Institute of Technology, Cambridge, MA, 2001.

[17] Yamaguchi I, Tadashige F. Laser Speckle Rotary Encoder. Appl. Optics, vol. 28 (20), pp 4401-4406, 1989.

[18] Anwar Chitayat. Rotary-linear Actuator, 1999. U.S. Patent No. 5982053.

[19] Grid Encoders, KGM: Technical Document. Heidenhain Corporation. 333 State Parkway Schaumburg, IL 60173-5337 Ph. (847) 490-1191 http://www.heidenhain.de/english/produkte/mg/kgm.htm Web page accessed Nov 12, 2003.

[20] Amar M. Kendale. Automation of Soft Lithographic Microcontact Printing. S.M. S.M. Thesis, Department of Mechanical Engineering, Massachusetts Institute of Technology, Cambridge, MA 2001.

[21] Agilent HDNS-2000 Optical Mouse Sensor: Product Brief. Semiconductor Products, Agilent Technologies. 5301, Stevens Creek Blvd. Santa Clara, CA 95051 Ph. (800) 235 0312 http://literature.agilent.com/litweb/pdf/5988-9329EN.pdf Web page accessed Dec 15, 2003.

[22] Paul Horowitz, Winfield Hill. The Art of Electronics. Cambridge University Press, New York 1989.

[23] Vijay Shilpiekandula, David L. Trumper. A Laser Speckle Sensor for Compound Rotary-Linear Motion Metrology. In Proceedings of ASPE Conference, vol. 30, pp. 51-54, 2003.

[24] Air Supply: Techical Document. Professional Instruments Company. 7800 Powell Road. Hopkins, MN 55343 Ph. (952) 933-1222 http://airbearings.com/ Included under "Useful Information". Webpage accessed Dec 16, 2003.

[25] Laboratory Handout, Assignment 4: Brushless Motor Control. MIT Course 2.737 on Mechatronics, Fall 1999. Available with Course Instructor, Professor David L. Trumper, Department of Mechanical Engineering, Massachusetts Institute of Technology, Cambridge MA 02139.

[26] Block-Head Operator's Manual. Professional Instruments Company. 7800 Powell Road. Hopkins, MN 55343 Ph. (952) 933-1222 http://airbearings.com/

[27] Alexander Slocum. Precision Machine Design. Englewood Cliffs, New Jersey. Prentice Hall, 1992.

[28] Stephen J. Ludwick. A Rotary Fast Tool Servo for Diamond Turning of Asymmetric Optics. Ph.D. Thesis, Department of Mechanical Engineering, Massachusetts Institute of Technology, Cambridge, MA 2001.

[29] Dahl P.R. Solid Friction Damping of Mechanical Vibrations, AIAA J. vol. 14, pp. 1675-1682, 1976.

[30] Vijay Shilpiekandula, David L. Trumper. A Laser Speckle Based Position Sensing Technique for a Rotary-linear Hybrid Axis. In Proceedings of NSF Design, Service and Manufacturing Grantees and Research Conference, 2004.

[31] Katherine A. Lilienkamp, David L. Trumper. Dynamic Signal Analyzer for dSPACE. In Proceedings of the dSPACE User's Conference, May 2000.